Study of low-pressure suspension plasma spray nanostructured coating : structural characteristics and application in solid oxide fuel cell

Shiming Xie

THESE DE DOCTORAT DE L'ETABLISSEMENT UNIVERSITE BOURGOGNE FRANCHE-COMTE

PREPAREE A L'UNIVERSITE DE TECHNOLOGIE DE BELFORT MONTBELIARD

Ecole doctorale n° 37

Sciences physiques pour l'ingénieur et microtechniques - SPIM

Doctorat de Sciences pour l'Ingénieur

Par

Mr. Shiming XIE

Study of low-pressure suspension plasma spray nanostructured coating: structural characteristics and application in solid oxide fuel cell

Defended on 17 June 2021, at sévenans campus of UTBM

With the jury composed of

Mr. Alain DENOIRJEAN	Directeur de Recherche, Université de Limoges	Président
Mr. Shrikant JOSHI	Professeur, University West	Rapporteur
Mr. Vincent JI	Professeur, Université de Paris-Saclay	Rapporteur
Mr. Hanlin LIAO	Professeur, Université Bourgogne - Franche-Comté	Examinateur
Mr. Frédéric LAPOSTOLLE	Maître de Conférences, Université Bourgogne - Franche-Comté	Codirecteur de thèse
Mr. Didier KlEIN	Professeur, Université Bourgogne - Franche-Comté	Directeur de thèse

Acknowledgements

My PhD thesis was carried out in the laboratory ICB-LERMPS, UMR 6303, CNRS, Université de Bourgogne Franche-Comté (UBFC) under the support of the China Scholarship Council (CSC).

First and foremost, I would like to thank all the members of the defense committee. Thank president Alain Denoirjean for his coming on site despite the impact of the epidemic. Thank Prof. Shrikant Joshi and Prof. Vincent Ji. They took much patience and time to review my thesis and also gave me a lot of valuable questions and suggestions during the defense. These are all very helpful for my future research. I really appreciate them.

Then, I would like to thank my director: Prof. Didier KLEIN and my co-director: Dr Frédéric LAPOSTOLLE. They gave me a lot of help and encouragement in my PhD career. It is my honour to have worked with them

Besides, I would like to thank Prof. Hanlin LIAO for his help, guidance, and encouragement throughout my work and life in France. I still remind so many times, he guided my experiments in the lab, so many times we discussed my PhD work in the middle of the night. His professional guidance and scientific skills made it possible to conduct my work successfully.

My sincere thanks also go to Mr Christian ADAM for his help in the modification of the LPSPS equipment. Without his help, I could not continue my experiments.

Many thanks to the members of our ICB-LERMPS laboratory: Charles BERNAGE, Joel CHAUVELOT, Emmanuelle ARCENS, Christophe VERDY, Yan WANG, Yongli ZHAO, Chunjie HUANG, Xiujuan FAN, Zexin YU, Xingchen YAN, Xinliang XIE, Tao JIANG, Meimei LIU, Hongjian WU, Franck DECROOS, Libin LALU KOITHARA, Shaowu LIU, Shuohong GAO, Yijun YAO, Wenbo LI, Yingjie LI and so on. I would like to thank them for their help with my PhD work. Also, many thanks to Chen SONG, Chunming DENG, Min LIU in Guangdong Institute of New

Materials for their help and support in terms of experimental materials and characterisation of the coatings.

Finally, I would like to thank my beloved family for their support and concern. Without their encouragement, support and love, I would not have made my PhD career successful.

General introduction

Ceramic coatings have been widely applied in aviation, biomedicine, and energy fields due to their excellent oxidation / corrosion resistance and mechanical and electrical properties. Air plasma spraying (APS) is one of the most frequently used preparation methods for ceramic coatings due to its low cost, high efficiency, and high heating temperature. In recent years, nanostructured / sub-microstructured coatings have attracted increased research interest in terms of improving the coating properties, such as mechanical strength, thermal insulation, wear resistance and so on. However, conventional APS can only use powder at the tens of microns scale due to gas-based feeding limitation, and preparing nanostructured / sub-microstructured ceramic coatings was therefore challenging. This problem is effectively solved by the suspension plasma spraying technique (SPS). Since SPS uses liquid as a medium to transfer feed powders, the powder can be submicron-sized or even nano-sized. For this reason, SPS is considered a promising preparation method for nanostructured / sub-microstructured ceramic coatings.

Nevertheless, the SPS method also has some disadvantages. Compared to APS, the heat transfer between powder and plasma jet in SPS is relatively lower, which easily cause insufficient heating of the particles. Besides, the momentum of the particle in SPS is also much lower, which causes a short spraying distance as well as a challenge in the preparation of high-density coating. The most commonly used method to improve these disadvantages of SPS is using high-power and high-velocity torch. Another possible method is carrying out the spraying process in a low-pressure environment. The low pressure can bring very obvious changes to the structure and property of the coating, which has been widely demonstrated between APS coatings and low-pressure plasma spraying (LPPS) coatings. Taking inspiration from this, a novel spraying technique– low-pressure suspension plasma spraying (LPSPS) – was recently proposed in order to improve the disadvantage of SPS as well as to obtain distinct coating structures not

achievable in conventional SPS coatings. This technology is developed on the platform of LPPS, in which the suspension spraying process is carried out under low pressure by using a specific plasma torch. However, the research of LPSPS is still in the exploratory stage, and related reports are very limited. Currently, the reported LPSPS coatings commonly have a much denser structure compared to the SPS coating. However, their adhesion and mechanical strength are quite low. More importantly, the structural characteristics of the LPSPS coating are still not fully understood. Its practical applications, especially the application in the electrolyte of SOFC, have not been fully studied or verified as well.

This thesis will further develop and study LPSPS. Different from the former reports on LPSPS, this thesis involves a more systematic and comprehensive investigation ranging from the development of LPSPS to its application. The main objectives of this thesis are: (1) To study the effect of the main spraying conditions on the microstructure of the LPSPS coating; (2) To explore the practical application fields, especially in the application of SOFC. In detail, this thesis includes the following contents:

Chapter 1 first provides a review of SPS. The deposition mechanism and characteristics of SPS coatings are introduced. Next, the development and research status of LPSPS are introduced, and the problems of the current LPSPS coatings are summarised. Then, a brief introduction of solid oxide fuel cell (SOFC) is provided, in which the potential value of LPSPS in the preparation of SOFC electrolyte is particularly introduced. Finally, the objectives of this thesis are proposed.

Chapter 2 introduces the experimental setups of LPSPS developed in this thesis, the used materials (powder and substrate) and the characterisation methods of the coating.

Chapter 3 investigates the effect of environmental pressure on the microstructure of YSZ coating prepared by suspension plasma spraying. The coatings are prepared by suspension plasma spraying under different pressures ranging from 980 mbar to 3 mbar. The influences of pressure on plasma jet characteristics, coating microstructure, coating

porosity and coating phase composition are investigated. Finally, the pressure of LPSPS is optimised, and the deposition mechanism of the LPSPS coating is proposed.

Chapter 4 investigates the tailoring of the microstructure of the LPSPS YSZ coating by varying the spraying conditions. These conditions include environmental atmosphere (argon versus air), oxygen content in the environment, spray distance, suspension solid content, solvent type. At the same time, the behaviour of the suspension in LPSPS is meticulously discussed. A vertical crack structure and a high-density structure are successfully tailored by adjusting the preparation parameters.

Chapter 5 investigates the application of LPSPS in the electrolyte of SOFC. YSZ electrolyte and lanthanum silicate electrolyte are deposited by the developed LPSPS processes in the previous chapters. The microstructure, crystallinity and gas permeability of both electrolytes are investigated.

Content

List of figures

List of tables

List of abbreviations

APS Air plasma spraying

CCD Charge Coupled Devices

CMAS $CaO\text{-}MgO\text{-}Al_2O_3\text{-}SiO_2$

CVD Chemical vapor deposition

DC Direct current

EB-PVD Electron beam physical vapour deposition

GDC Gadolinia-doped ceria

LPPS Low-pressure plasma spraying

LPSPS Low-pressure suspension plasma spraying

LSO $La_{10-x}Si_6O_{27-1.5x}$

LSSO $La_9SrSi_6O_{26.5}$

MS Melted splat

NP Nanoparticle

OES Optical emission spectroscopy

PVD Physical vapor deposition

SEM Scanning electron microscope

SOFC Solid oxide fuel cell

SPS Suspension plasma spraying

SP Spherical particles

TBC Thermal barrier coating

XRD X-ray diffraction

YSZ Yttria-stabilised Zirconia

Chapter 1 Background

Chapter 1 Background

1.1 Nanostructured / sub-microstructured ceramic coatings

Ceramic coatings (e.g., YSZ, Al_2O_3, TiO_2 coatings) have been widely applied in aviation, biomedicine, energy and electrical fields due to their excellent oxidation and corrosion resistance and mechanical and electrical properties. Typical cases include thermal barrier coatings (TBCs), wear-resistant coatings, photocatalysis coatings and the functional layer of solid oxide fuel cells (SOFC). Among the preparation methods for ceramic coatings, air plasma spraying (APS) has been one of the most frequently used due to its low cost, high efficiency and high heating temperature.

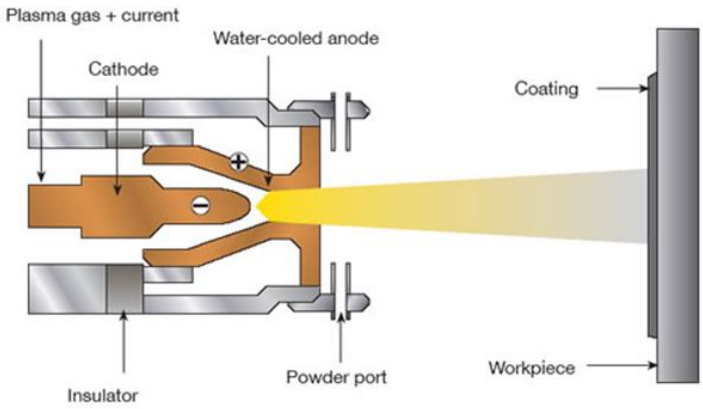

Fig. 1.1 Schematic of air plasma spraying [1]

Fig. 1.1 shows the schematic of APS (without a specific declaration, in this thesis, the plasma spraying refers to direct current (DC) plasma spray). The plasma torch is typically composed of a tungsten cathode and a copper anode in the form of a nozzle. Both are cooled by circulating water. The cathode and anode are respectively connected to the positive and negative electrodes of the DC power. Plasma gases (Ar, H_2, He etc.) are added to the torch from the bottom of the anode. They are ionised by the high-frequency arc formed between the cathode and the anode to produce high-temperature plasma, which is eventually ejected from the nozzle to form a plasma jet. The powders are fed into the plasma jet by carrier gases (Ar or N_2), are rapidly heated to a molten or

semi-molten state and finally impact the substrate to form a coating. Since the plasma jet can be up to 12000–15000 K, at this temperature, in theory, almost all materials can be melted. Hence, APS is particularly suitable for preparing coatings with high melting points, like ceramic coatings.

In recent years, nanostructured / sub-microstructured coatings have attracted increased research interest in an effort to improve the performance of the coating. It has been found that, compared to conventional coatings, nanostructured / sub-microstructured coatings show significantly improved mechanical properties [2, 3], wear resistance [4-6], thermal shock behaviour [7, 8] and photocatalytic efficiency [9, 10], etc. In order to achieve the preparation of nanostructured / sub-microstructured ceramic coatings by using APS, nano- or submicron-sized feed powders are required. However, conventional APS can only use powders at the tens of the microscale. This is because nano- or submicron-sized powders need a much higher flow of carrier gas to deliver due to their low mass, which will drastically perturb the high-enthalpy plasma jet [11, 12]. In addition, the electrostatic forces between fine particles can dominate the gravity acting on the particles, resulting in particle agglomeration and an inability to transfer powders through the feeder [13].

One way to solve this drawback is using coarse agglomerated powders composed of nanopowders. However, this method will greatly increase the cost and time of coating preparation. More importantly, the homogeneity of the coating prepared by using this method is quite poor. The agglomerated powder is easily heated into a hybrid structure with a melted dense layer outside and unmelted nanoparticles inside. As a result, the coating typically contains a bimodal microstructure rather than a full nanostructure, as shown in Fig. 1.2.

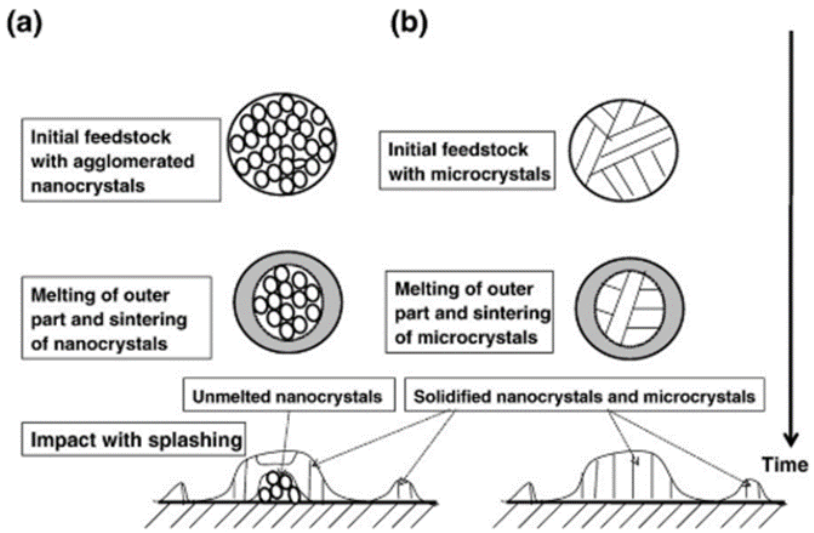

Fig. 1.2 Schematic of the typical microstructure of the thermal sprayed coating using different types of feed powder: (a) agglomerated powder, (b) conventional powder[14]

1.2 Suspension plasma spraying (SPS)

Another solution is using suspension-containing nanopowders as the feedstock, known as suspension plasma spraying (SPS) (without a specific declaration, in this thesis, the SPS refers to the suspension plasma spray carried out under atmospheric pressure), which was invented in the mid-1990s by Université de Sherbrooke [15]. This method completely solves the problem of fine-powder transfer. Moreover, the resulting coating has good homogeneity, so it is considered to be the most effective method for preparing nanocoatings by plasma spraying technology. The schematic of suspension plasma spraying is shown in Fig. 1.3. The suspension is transported to the plasma jet by a pressurised vessel or by a peristaltic pump. Sometimes, the suspension needs to be atomised before injection. The typical SPS system is developed on the APS platform. Therefore, the cost of the SPS is as low as that of the APS, to some degree. In addition, the deposition rate of SPS coating is much higher than traditional nanostructure coating preparation methods, such as PVD (physical vapour deposition) and CVD (chemical vapour deposition). For these reasons, the SPS technique has been attracting more and more attention in both academia and industry.

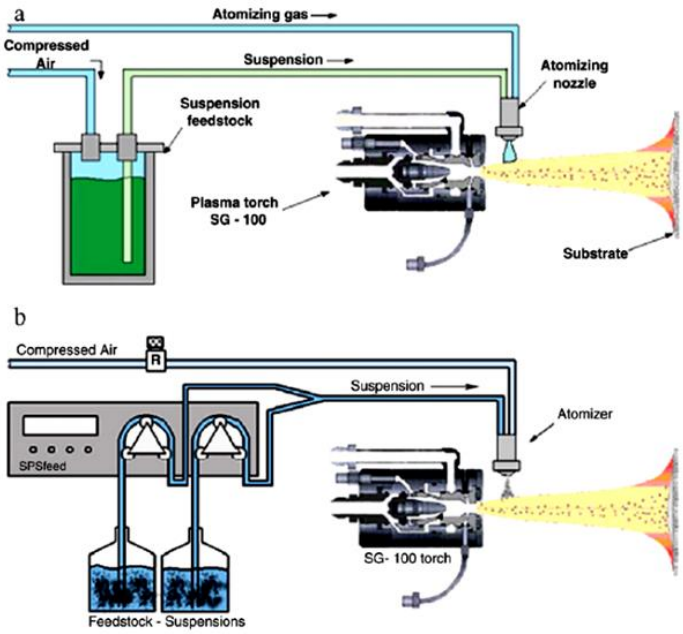

Fig.1.3 Schematic of suspension plasma spraying:(a) by using pressurized vessel, (b) by using peristaltic pump [16]

1.2.1 Evolution process of suspension in the plasma jet

The biggest difference between SPS and APS is the feedstock behaviour in the plasma jet. In terms of SPS, the suspension will go through a much more complicated evolution before reaching the substrate. Fig. 1.4 shows a schematic of the suspension evolution from being injected into the plasma jet to finally deposited on the substrate.

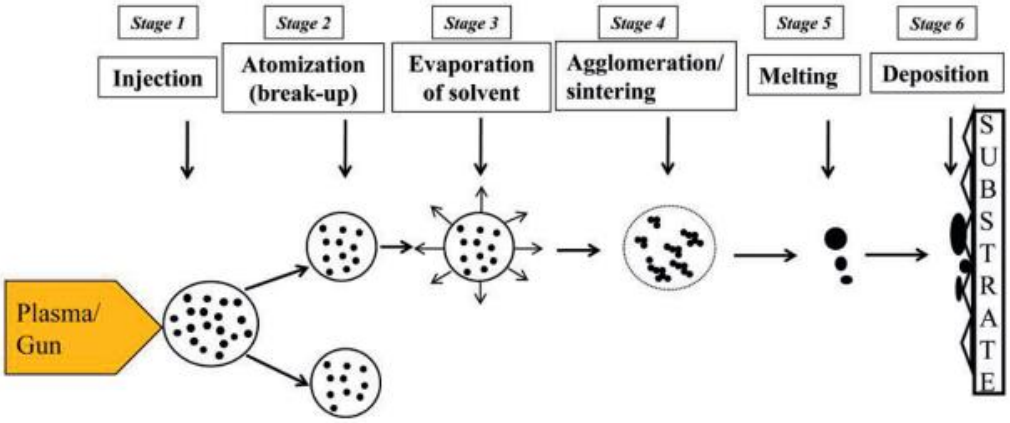

Fig. 1.4 Evolution process of the suspension in SPS from the injection to the final deposition[17]

1. Injection of the suspension.

The first stage is the injection of the suspension. There are two major types of injection: axial injection and radial injection, as shown in Fig.1.5. In the case of axial injection, the suspension can smoothly enter the plasma centre so that the powder can be heated more fully. However, this injection form can only be realised with a specific axial spray torch [18-20]. In terms of the radial injection, a considerable part of the suspensions will enter the fringe area of the plasma, as shown in Fig. 1.6, where more untreated or resolidified particles will be produced, reducing the quality of the coating. However, the radial injection has better compatibility with most plasma torches than the axial injection. Therefore, the radial injection is more commonly used in SPS. In addition to the injection type, injection angle, injection pressure [21] and pre-atomisation prior to injection [22] also have an influence on the behaviour of the suspension in the plasma jet. In short, the injection of the suspension needs to be strictly controlled during the coating preparation.

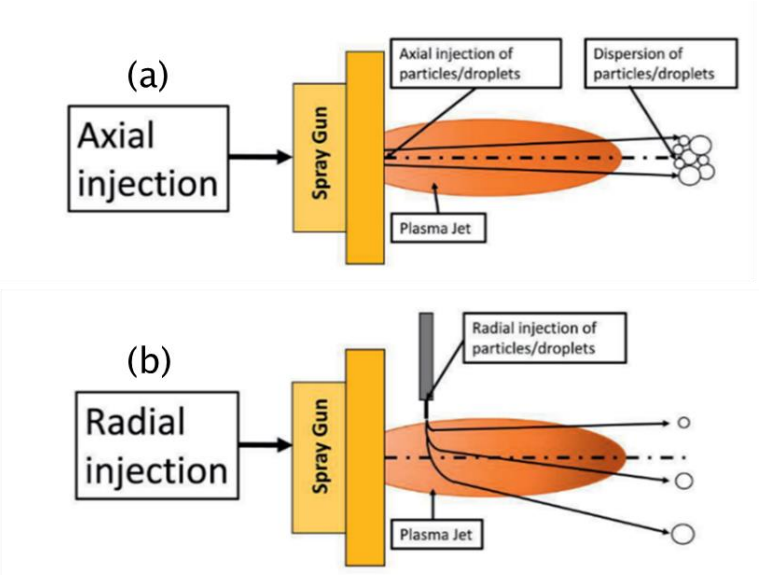

Fig. 1.5 Schematic of two injection types in SPS [17]

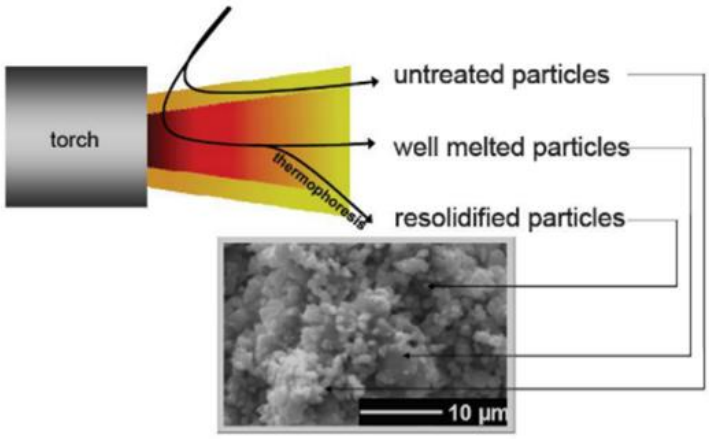

Fig. 1.6 Distribution of the particles in the plasma jet in SPS with the radial injection form [23]

2. Suspension fragmentation

After the suspension is injected into the plasma, it is fragmented into small droplets (atomisation process). The drag force of the plasma jet and the surface tension of the droplet are the two most important factors influencing fragmentation. The drag force (shear force) tends to break the droplets, while the surface tension of the droplet tends to maintain the integrity of the droplets [14, 24, 25]. In the practical process, drag force is much higher than surface tension; thus, the suspension will be rapidly fragmented once it is injected into the plasma [25]. When the initial drop started with 300 μm, J. Fazilleau et al. [21] calculated the fragmentation time (τ_f) to be ~ 0.15 μs. The diameter of the droplet can be calculated using the following relation [12, 26]:

$$D = \frac{8\sigma_l}{C_D \rho U^2} \qquad (1)$$

where, σ_l , C_D, ρ, U is the surface tension ($N \cdot m^{-1}$), the drag coefficient, the plasma density($kg \cdot m^{-3}$) and the plasma velocity($m \cdot s^{-1}$) relative to the droplet velocity, respectively. The drag force can be influenced by the plasma gas composition, flow rate and torch current. The surface tension is only determined by the inherent characteristics of the suspension. For example, the surface tension of water is much larger than that of ethanol, so water is relatively difficult to be fragmented. The droplet viscosity is mainly affected by the solid content of the suspension and the powder size [14, 27]. Normally, the higher

the solid content, the higher the droplet viscosity and the larger the size of the droplet.

3. Vaporisation of solvent

Due to the ultra-high temperature of the plasma jet, the solvent in the droplet is rapidly heated and vaporised. The interaction between the solvent and the plasma mainly occurs at this stage. For example, the vaporisation of water takes heat from the plasma. In contrast, the ethanol will undergo a combustion reaction after vaporisation, releasing heat into the plasma. Fig. 1.7 shows infrared images of the plasma jet with different solvents injected. It can be seen that the temperature of the water-injected plasma jet drops rapidly, while that of the ethanol-injected plasma jet first drops slightly and then rises obviously, which is attributed to the ethanol combustion after vaporisation. As a result, the ethanol-injected plasma jet can maintain a high temperature over a longer distance.

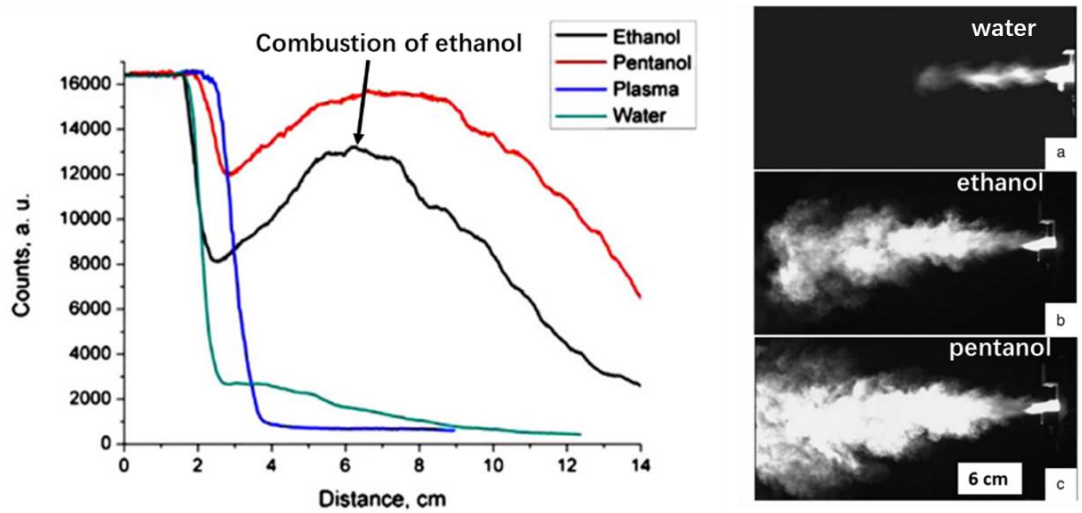

Fig. 1.7 Infrared images of the plasma jet with different solvents injected: (a) line profile along the plasma jet axis of averaged infrared image, (b) infrared images [28]

4. Agglomeration of nanopowders

Once the atomised droplet vaporises, the exposed nanopowders tend to agglomerate together due to their high surface energy [29]. The factors affecting nanopowder agglomeration mainly include [30] 1. Van der Waals forces. 2. Moisture (hydrogen

bonds). 3. Capillary forces. 4. Adsorbed foreign species. 5. Particle pre-sintering (during particle syntheses). Due to the agglomeration of the nanopowder, most of the particles in the plasma jet of SPS are much larger than the feed powder. Besides, the large agglomerates can be further divided into small agglomerates during the flight process, as shown in Fig. 1.8. Finally, the plasma jet actually contains a large number of agglomerates at various sizes, as well as a few single particles without agglomeration. For this reason, the SPS coating typically contains the particle in various sizes [31-33].

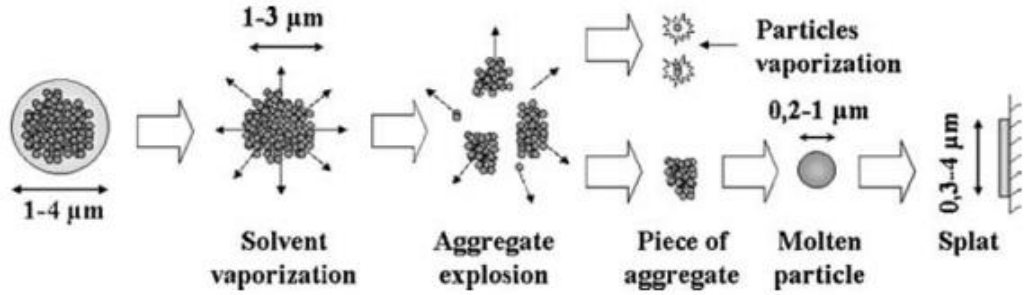

Fig. 1.8 Further fragmentation of the large agglomerate in SPS [34]

5. Melting of the particles

Strictly speaking, the nanopowders are heated and melted as soon as they are exposed to the plasma, so the melting process and the agglomeration process can be considered to occur simultaneously. Since the radial temperature distribution of the plasma jet is not uniform (the temperature at the plasma centre is higher than at the plasma fringe), the particles are differently heated in practical conditions. Fig. 1.9 shows the deposited particles and their corresponding products on the coating. In the case of sufficient heating, the particles tend to transform into splats, which normally corresponds to a dense coating [35-37]. In the case of insufficient heating, the particles tend to transform into nanoparticle clusters or single particles, which normally corresponds to a porous coating. As a matter of fact, in most cases, due to the low momentum, small agglomerate and single particles are hard to turn into splat, even though they are heated sufficiently.

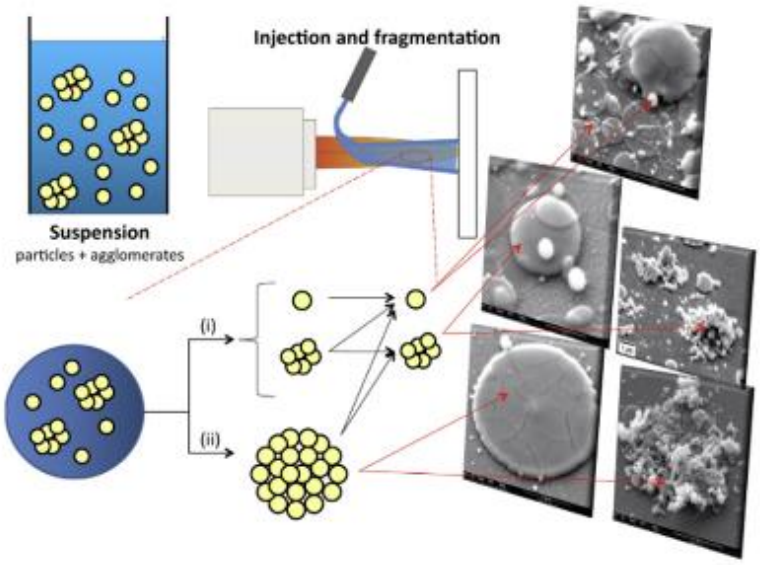

Fig. 1.9 Deposited particles with different morphologies and their corresponding products in the SPS coating [38]

1.2.2 Structural characteristics and deposition mechanism and of the SPS coatings

In terms of SPS, a part of the plasma jet energy is used to evaporate the solvent. Therefore, the heating state of the particles in SPS is generally worse than that of the particles in APS. In addition, the nano-sized or submicron-sized powders have low mass. Thus, their dynamic inertia and thermal inertia are much lower than that of coarse powder used in APS. In other words, the nano-sized or submicron-sized powders easily lose velocity and temperature with the in-flight distance increasing [34, 39]. C. Delbos et al. [34] simulated the particle temperature and particle velocity as a function of the spraying distance. They found that the particles at a size of 0.1μm reached their maximum velocity of 500 m/s within the first 10 mm of their trajectory. Thereafter, the velocity rapidly dropped to 350 m/s within the next 10 mm. It was also found that the small particles were earlier solidified due to a faster cooling rate. For these reasons, SPS coatings easily form a porous nanostructure that is expected in some special applications, like photocatalytic coatings and TBCs (thermal barrier coatings). Fig. 1.10 shows the typical microstructure of TiO_2 photocatalytic coating prepared by SPS and by APS. It

can be seen that TiO_2 prepared by SPS has a much higher specific surface than that prepared by APS due to the porous nanostructure of the SPS coating. As a result, TiO_2 coating prepared by SPS exhibits a higher photocatalytic efficiency compared to that deposited by APS [40, 41]. In addition, the porous nanostructure also produces a large number of nanopores, which can help to decrease the thermal conductivity of TBCs [42].

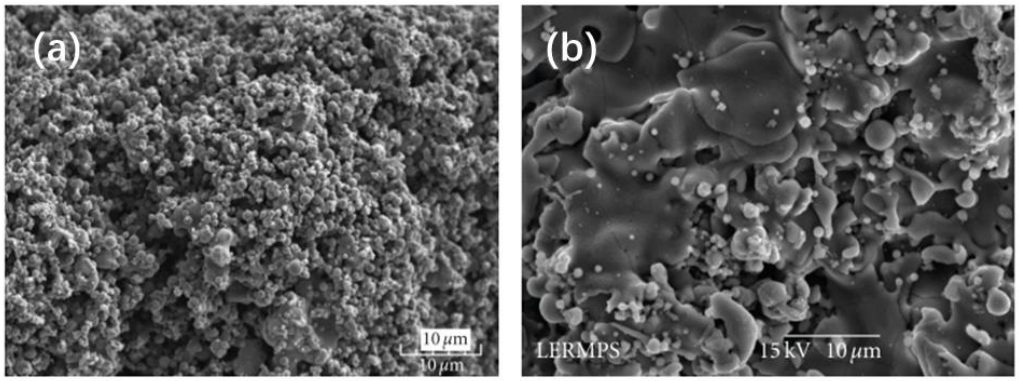

Fig. 1.10 Typical microstructure of TiO_2 photocatalytic coating prepared by SPS (a) and by APS (b) [43]

In addition to the porous structure, the columnar structure is another structural characteristic widely reported in SPS coatings, as shown in Fig. 1.11. This feature is strongly determined by the unique deposited mechanism of SPS coating. Berghaus et al. [44] simulated the change in the direction of the particle velocity as a function of the particle size in the plasma jet, as shown in Fig. 1.12. It can be seen that the trajectory of the particle with a small size is more easily affected by the plasma jet. In order to characterise the motion behaviour of particles in the plasma jet, a dimensionless number of Stokes number (S_t) is introduced as shown in Eqs. (2):

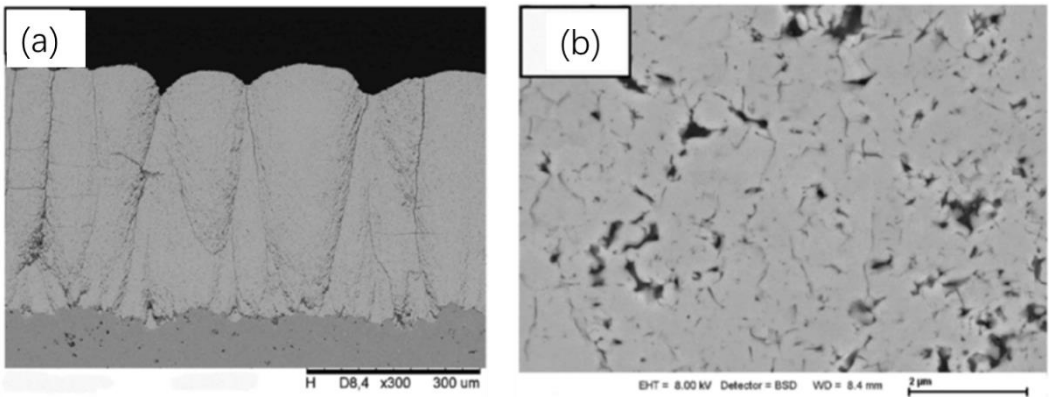

Fig. 1.11 Porous columnar structure of SPS: (a) at low magnification; (b) at high magnification[45]

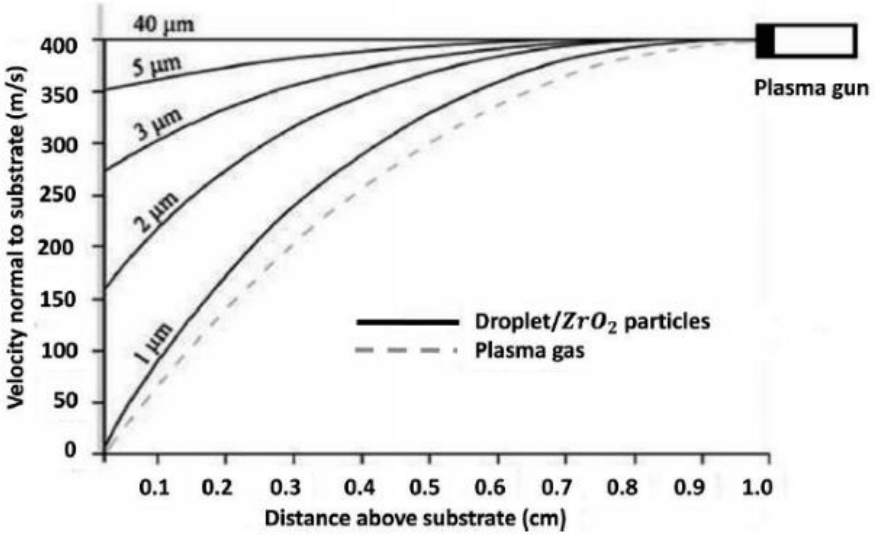

Fig. 1.12 Effect of plasma flow on particles trajectory before impacting the substrate in SPS [44]

$$S_t = \frac{\rho_d d^2 v_0}{18 \mu_g l} \qquad (2)$$

where ρ_d is the particle density, d is the particle diameter, v_0 is the fluid velocity of the flow (plasma jet), l is the characteristic dimension of the obstacle (substrate) and μ_g is the gas dynamic viscosity (plasma viscosity). The lower the S_t, the more likely the particles will follow the plasma jet trajectory.

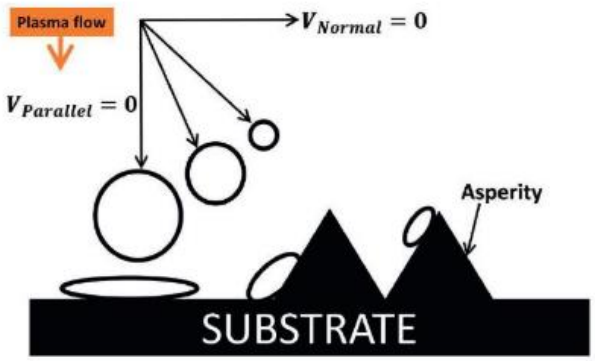

Fig. 1.13 Impact trajectories of the particles upon the substrate in SPS [17]

When the plasma jet reaches the substrate, the plasma jet trajectory changes from perpendicular to the substrate to parallel to the substrate. Since the particles in SPS typically exhibit a low S_t due to their mass, they easily follow the plasma jet trajectory. As a result, the particles mostly deposit on the sides of surface asperities, which causes a prominent growth of the coating on the asperities, as shown in Fig. 1.13. After multiple spraying passes, the columnar structure is built up upon the asperities, as shown in Fig. 1.14.

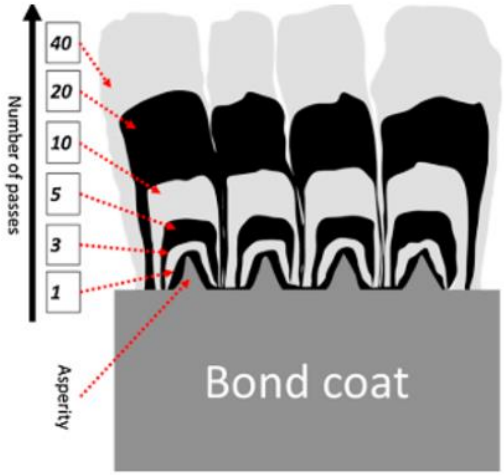

Fig. 1.14 Schematic of the formation of the columnar structure of SPS coatings [46]

The columnar structure has a good thermal strain tolerance for thermal cycling. Hence, SPS has a huge advantage in the preparation of TBC [47-51]. Bernard et al. [42] systematically evaluated the characteristics of the TBCs prepared by SPS, APS and EB-

PVD (Electron Beam Physical Vapour Deposition). They summarised the microstructural features of the coating prepared by these three methods, as shown in Fig. 1.15.

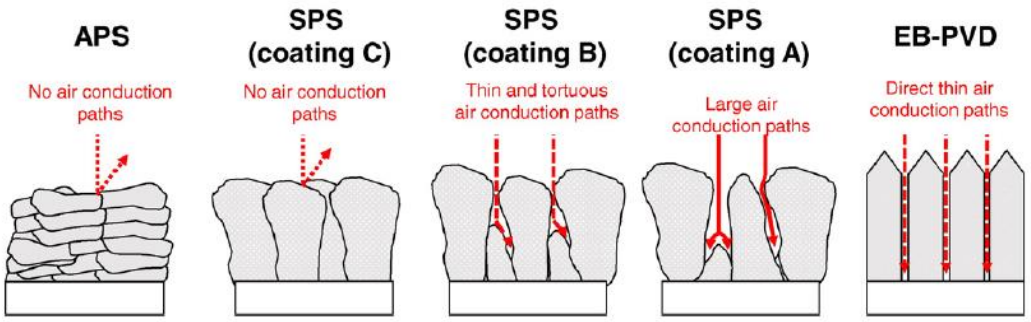

Fig. 1.15 Air conduction model for the different TBCs [42]

The APS coating exhibits a laminar structure with a low thermal strain tolerance. Hence, its thermal shock resistance is the lowest among all methods. However, the laminar structure cut off air conduction through the coating, which can substantially lower the thermal conductivity of the coating. Hence, the APS coating normally has good thermal insulation. The EB-PVD coating exhibits a typical columnar structure with high column density, so it has the most excellent thermal shock resistance. However, the gap between the column shows an entirely vertical shape, which provides a favourable channel for air conduction. Hence, the thermal conductivity of the EB-PVD coating is the highest among all coatings. In terms of SPS coating, the column density in the coating is relatively low; thus, its thermal shock resistance is also relatively lower than that of EB-PVD coating, but still much higher than that of APS coating. In addition, the gap between the columns in the SPS coating exhibits a feature of tortuosity, which can reduce the air conduction to a certain extent. Moreover, the micropores in the SPS coating can significantly enhance phonon scattering, as shown in Fig. 1.16. These two features allow the SPS coating to exhibit a lower thermal conductivity than the other two coatings.

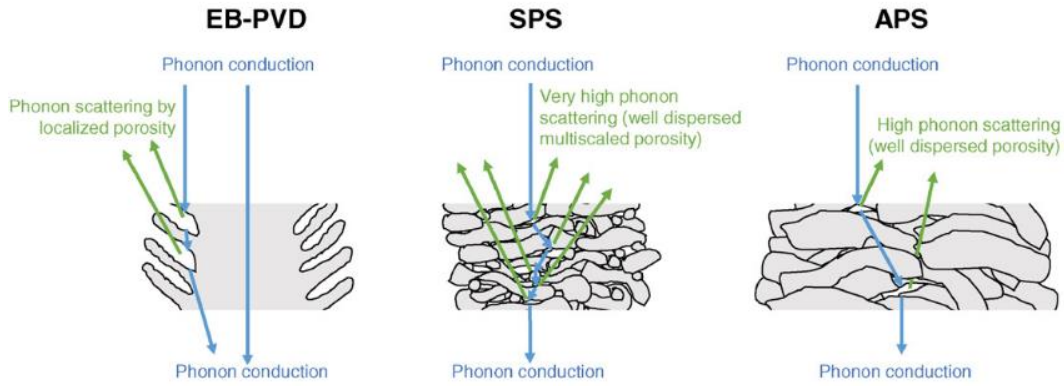

Fig. 1.16 Phonon scattering in the different TBCs [42]

1.2.3 Disadvantages of SPS

It is known that compared to the coarse structure of the APS coating, the fine structures provide the SPS coating with many improved properties, such as mechanical strength, photocatalytic efficiency, thermal insulation, thermal strain tolerance and so on. However, the SPS method also has some disadvantages. As mentioned above, compared to APS, the heat transfer between particles and plasma jet in SPS is relatively lower, easily causing insufficient heating for the particles. It can decrease the adhesion of the coating at last. Besides, the momentum of the particle in SPS is also lower, which causes a much shorter spraying distance (~30-50 mm) than that (~100 mm) of APS. The excessively short spraying distance will limit the application of this technology on complex-shaped workpieces such as turbine blades [52]. Moreover, the low momentum of the particle also makes it challenging to prepare high-density coating by using SPS.

The most commonly used method to improve these disadvantages of SPS is using a high-power and high-velocity torch, like the commercial Axial III plasma torch (Northwest Mettech Corporation, Vancouver, Canada) [53-55]. The structure of the Axial III plasma torch is shown in Fig.1.17. It is composed of three independent cathodes and anodes, and can be seen as a combination of three independent plasma torches arranged in parallel. The plasma jet produced by each torch converge together and form an enhanced plasma jet.

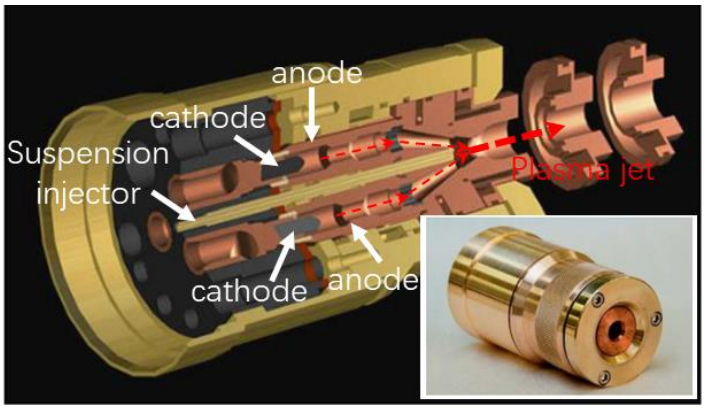

Fig. 1.17 Northwest Mettech Axial III plasma torch [56]

The main characteristics of the Axial III torch are listed as follows [57]:

Plasma gas: Ar, N_2, H_2 (He)

Plasma flow: 100–300 slpm

Input power range: 30–105 kW

Arc current: 300–750 A

Spray distance: 50–250 mm

Such a special structure of the Axial III torch not only allows it to have higher power and plasma jet velocity but also allows the suspension to be axially injected. All of these can help to improve the disadvantages of conventional SPS technologies. Fig. 1.18 shows the Al_2O_3 coating prepared by SPS using the Axial III torch. It can be seen that the coating exhibits a high density. A large number of fine splats are formed on the coating. It reflects the high velocity of the deposited particles. It should be noted that the preparation conditions (122 kW of torch power and 220 slpm of plasma gas flow) are very demanding, which almost reaches the design limit of this torch. Fig. 1.19 shows the YSZ electrolyte coating prepared by SPS using the Axial III torch. It can be seen that only under appropriate parameters (high current, high plasma flow and short spray distance) can a high-density coating be successfully prepared.

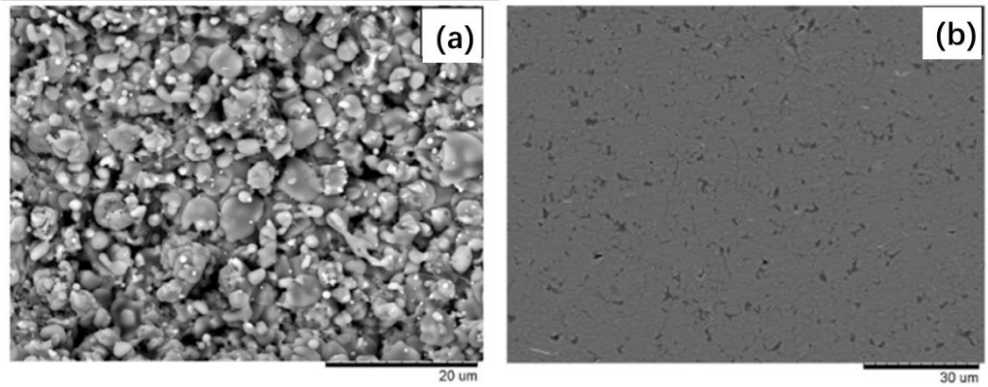

Fig. 1.18 Microstructure of the Al_2O_3 coating prepared by Axial III torch: (a) surface morphology, (b) cross-sectional morphology [53]

(Preparation conditions: torch power:122 kw, plasma gas flow: 220 slpm ($Ar/N_2/H_2$), Al_2O_3 powder: D50=~2 μm)

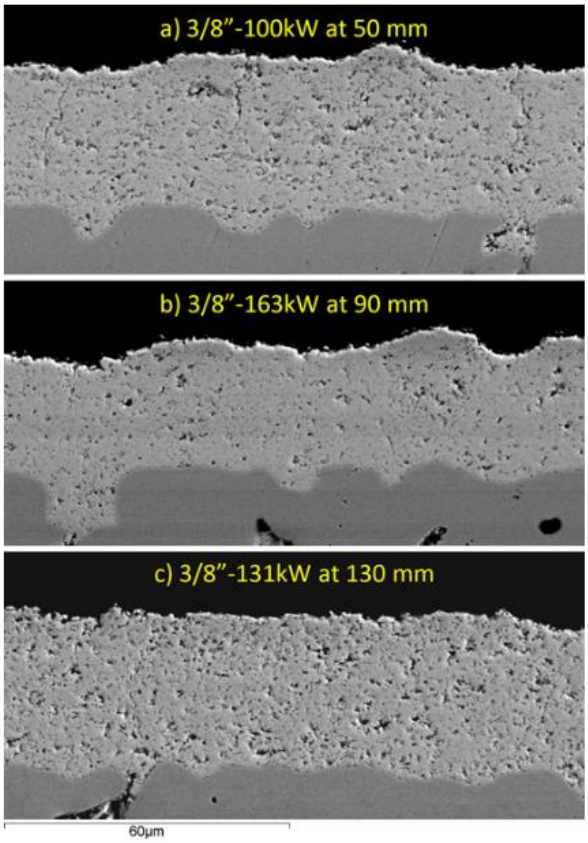

Fig. 1.19 Microstructure of the YSZ coatings prepared by Axial torch III [58]

(Preparation conditions: torch power: 100-163 kW, plasma gas flow: 275 slpm ($Ar/N_2/H_2$, 8mol% YSZ powder: D50 = 2.6 μm)

1.3 Low-pressure suspension plasma spraying (LPSPS)

1.3.1 Effect of low-pressure on the plasma spraying

In addition to high power and high-velocity torch, another possible way to improve the disadvantage of SPS is carrying out the spraying process under low pressure. In fact, the spraying technology under low pressure can be traced back to the 1970s. Based on the APS, researchers proposed low-pressure plasma spraying (LPPS), the schematic of LPPS is shown in Fig. 1.20. Different from the APS conducted in the atmosphere. The LPPS is conducted in a low-pressure environment.

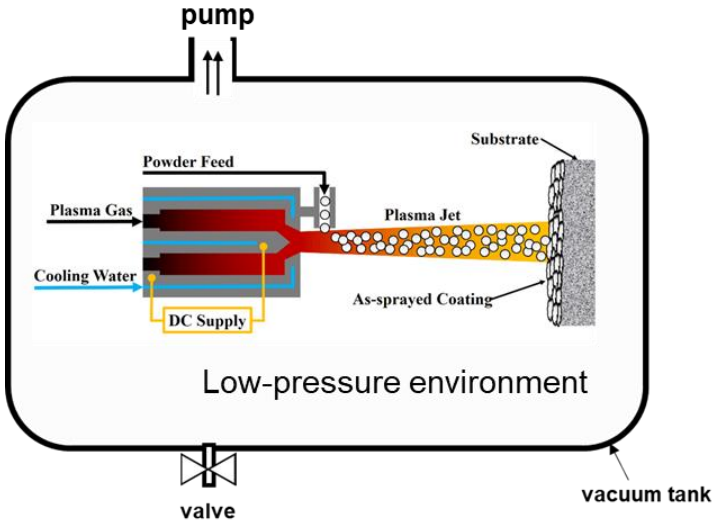

Fig. 1.20 Schematic of LPPS

In comparison to APS, LPPS exhibits many different characteristics. First, the plasma jet in LPPS is more expanded. Fig. 1.21 shows the shape of the plasma jets under different pressures. It can be seen that the plasma jet becomes wider and longer as the pressure decreases. This phenomenon is because the thin atmosphere under low pressure has less heat conductivity and gas resistance to the plasma jet.

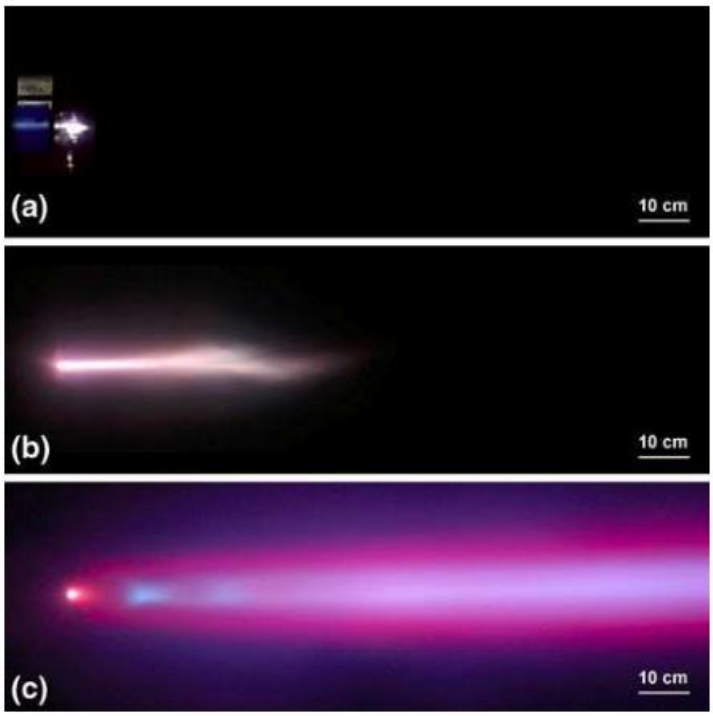

Fig. 1.21 Images of the plasma jets under different pressures: (a) 95 kPa (950 mbar / APS), (b) 5 kPa (50 mbar / LPPS), and (c) 0.1 kPa (1 mbar / LPPS) [59]

Second, the particle velocity in LPPS is much higher. Due to the less gas resistance to the particles， the particles in LPSPS can be accelerated to a rather high velocity [60]. For that reason, LPPS coatings typically have a higher density compared to APS coatings [61-64]. Fig. 1.22 shows the wear-resistant coatings prepared by LPPS. It can be seen that these coatings all exhibit a high density without obvious pores.

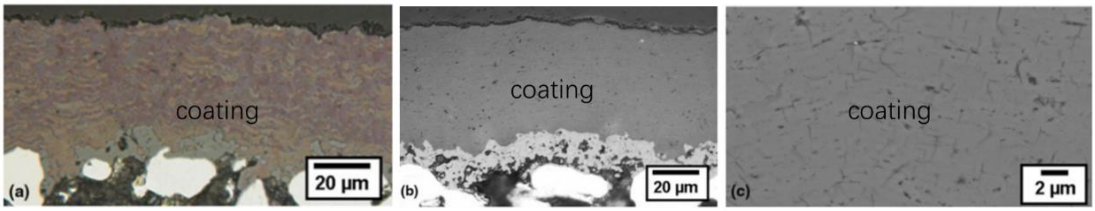

Fig. 1.22 Dense structured coatings prepared by LPPS: (a) titania coating, (b) alumina coating, (c) a magnified detail of a magnesia alumina spinel coating [61]

Third, the particles in LPPS are heated more thoroughly. The longer plasma jet of LPPS increases the dwell time of the particles in the plasma jet, allowing the particles

to be heated more thoroughly [65], which can help to increase the adhesion of the coating.

Forth, the morphology of the deposits in LPPS is diverse. Low pressure allows the heated particle to be vaporised more easily. Under certain conditions, the powder can be completely or partially vaporized. In that case, the deposits are not limited to the form of liquid droplets but can also be in the form of smaller-sized nanoclusters or vapors. These finer deposits nucleate and grow up on the substrate to form the coating. This kind of deposition form is completely different from the stacking form of splats of APS coating. Therefore, the resulting coating exhibits a unique structure that is completely distinguished from the layered structure of APS coatings. Fig. 1.23 shows a feather-like structured coating prepared by LPPS. Such a structure allows the coating to have excellent thermal shock resistance as well as low thermal conductivity [40, 52].

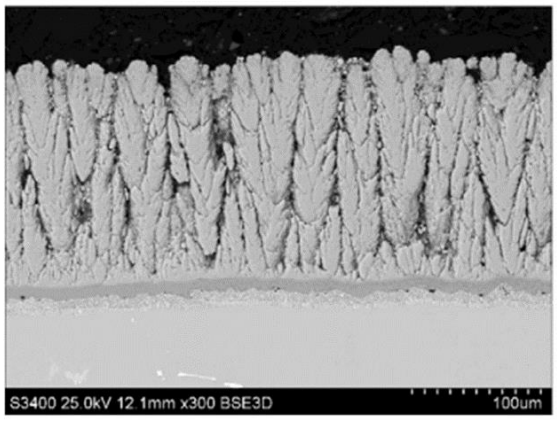

Fig. 1.23 Feather-like structured coating prepared by LPPS [66]

1.3.2 Development and research status of LPSPS

According to the effect of low pressure on the coating deposition as mentioned above, it is reasonably believed that that low pressure is expected to improve the disadvantage of conventional SPS, and provides a new possibility for preparing distinctly structured coatings not achievable by using SPS. Taking inspiration from LPPS, in recent years, researchers proposed low-pressure suspension plasma spraying (LPSPS).

To the best of the authors' knowledge, in 2014, Purdue University (U.S.A.) and Université de Technologie de Belfort Montbéliard (UTBM) (France) almost

simultaneously reported the first research results on LPSPS. In May 2014, Purdue university firstly prepared SOFC electrolytes by LPSPS [67]. This work was achieved on the platform of LPSPS in Sandia National Laboratories' Thermal Spray Research Laboratory (SNL's TSRL) (U.S.A.), as shown in Fig. 1.24. The spray torch used was a Sulzer Metco OSCA high-energy radial plasma torch. The microstructure of the resulting electrolyte layer is shown in Fig. 1.25. The electrolyte layer was thin and dense enough but contained many unmelted particles. It is believed that the radial suspension injection is not suitable for the LPSPS since it is hard for the fine powder to enter the expanded plasma jet in the form of radial injection.

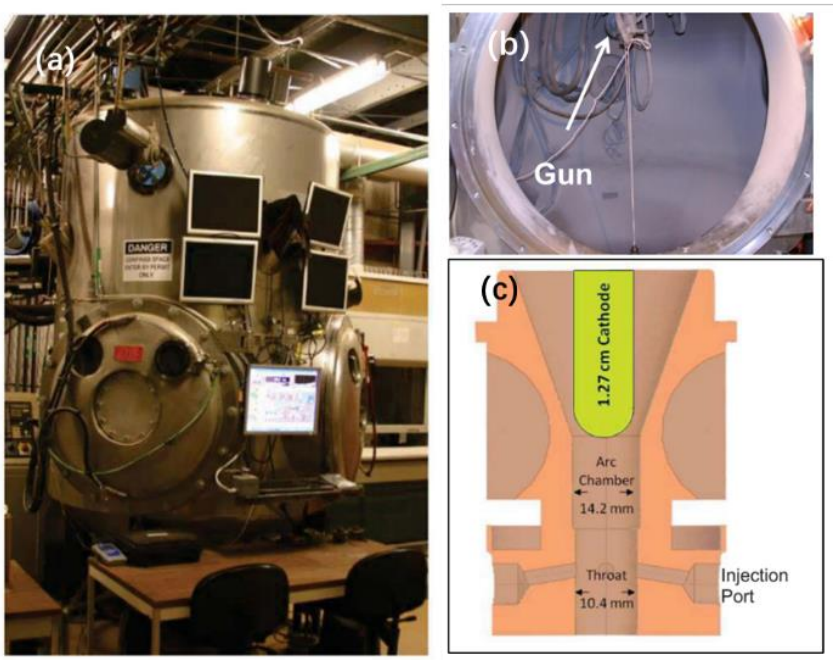

Fig. 1.24 Low-pressure plasma spray platform of SNL's TSRL [67]: (a) appearance of the spraying equipment, (b) interior of the vacuum chamber, (c) schematic of OSCA radial plasma torch for spraying

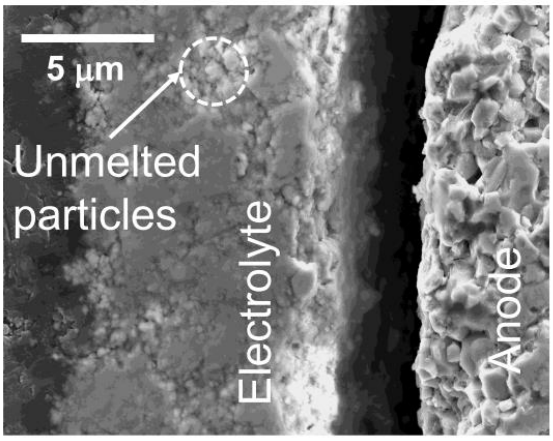

Fig. 1.25 Cross-sectional image of the YSZ electrolyte layer prepared by LPSPS reported by Purdue University [67]

(Preparation conditions: torch: Sulzer Metco O3CA plasma torch, torch power: 69 kw, pressure: 2.4 Torr, powder: 8 mol%YSZ, plasma gas: Ar/H_2: 59 slpm/7 slpm, spraying distance:117 mm)

In November 2014, He et al [68] in Université de Technologie de Belfort Montbéliard first reported a study on LPSPS with axial injection. This work was carried out based on the platform of LPPS in LERMPS laboratory of UTBM, as shown in Fig. 1.26. A homemade tri-cathode axial torch was used for spraying, as shown in Fig. 1.27. The torch is composed of three cathodes with a common anode. The three cathodes are arranged in a cone at a certain angle and produce three independent arcs to generate three plasma jets. They eventually converge into an enhanced plasma jet which is ejected from a common nozzle. Such a special design not only allows the torch to have a relatively higher power (up to 60 kW), but also allows the suspension to be axially injected; it is expected to remove the unmolten particles to a large degree. The microstructures of the resulting coating are shown in Fig. 1.28. It can be seen that the coating exhibits completely distinct morphologies from the conventional SPS coating. There are a large number of nanoparticles on the coating, and no noticeable pores can be observed in the coating. It is considered to be a hybrid coating based on the deposition of vapor and droplets. The density of the coating is much higher than that of the SPS coating, but the

interparticle cohesion of the coating appears to be poor, causing detachment in the coating. The coating also has poor mechanical strength; the hardness and elastic modulus of the coating are only 4.70 ± 0.90 GPa and 114.50 ± 8.20 GPa, respectively. Besides, the tri-cathode torch uses the same cathode as the commercial F1 torch. The torch current, therefore, can only remain at a relatively low level, which is not beneficial to the heating of the powders. Moreover, the design of the tri-cathode torch is not suitable for the low-pressure environment. It was seriously eroded after several sprayings. He et al. was forced to stop the research after the limited experiments.

Fig. 1.26 LPPS system in LERMPS laboratory of UBTM [69]

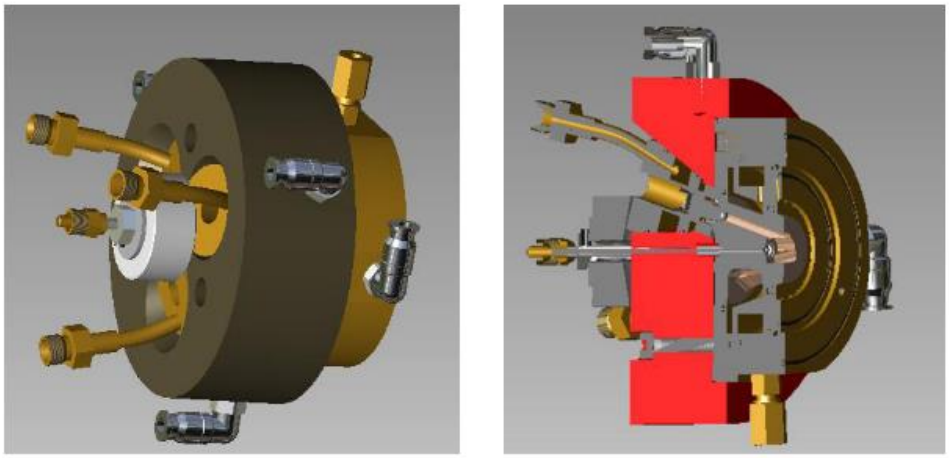

Fig. 1.27 Tri-cathode torch with the axial injection mode [68]

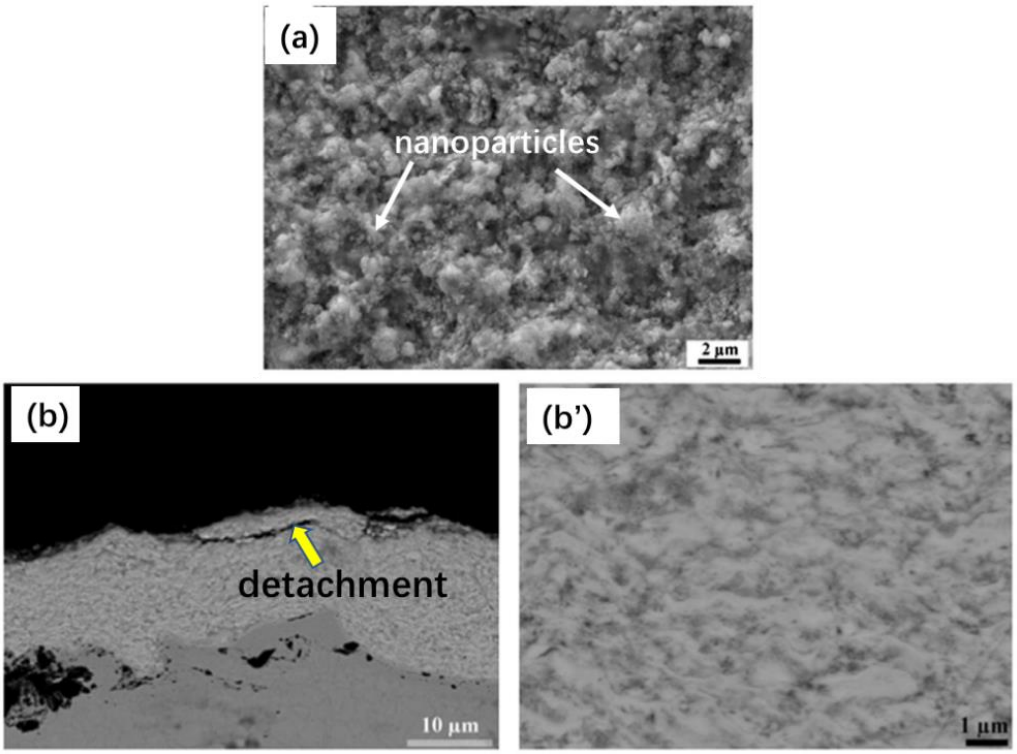

Fig. 1.28 Microstructures of the YSZ coating prepared by LPSPS reported by He et al. [68]: (a) surface image, (b)(b') cross-sectional images

(Preparation conditions: torch: tri-cathode torch, power: 53 kW, pressure: 100 Pa, powder: 3 mol%YSZ (D50=0.1μm), plasma gas: Ar/H_2: 120 slpm/10 slpm, spraying distance: 150 mm)

On the basis of the work of He et al., Song et al. [69] in the Université de Technologie de Belfort Montbéliard designed a bio-cathode axial plasma torch that is suitable for low-pressure environments, as shown in Fig. 1.29. The design of this torch referred to the tri-cathode axial torch, but the nozzle was designed to be further expanded. Moreover, the cathode is replaced with the one used in the commercial F4 torch. In order to save costs, the torch only included two cathodes. Nevertheless, since the cathode of F4 torch can support a higher current than that of F1 torch, the bi-cathode can also remain a relatively high power. By using this torch, Song et al. carried out a series of experiments. Fig. 1.30 shows the microstructures of the resulting coating. The coating shows a good density, and its morphology is similar to that prepared by He et al.

Unfortunately, the adhesion of the coating was still very poor, and most coatings fell off after a few weeks.

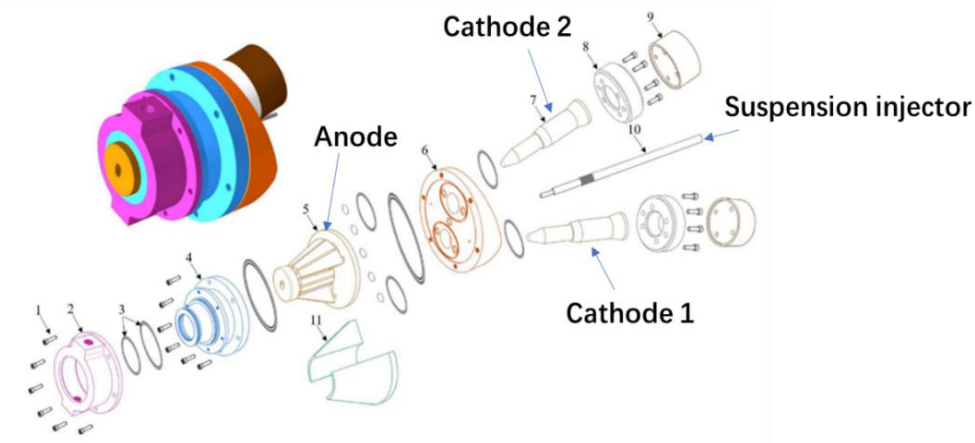

Fig. 1.29 Schematic of bio-cathode axial plasma torch [69]

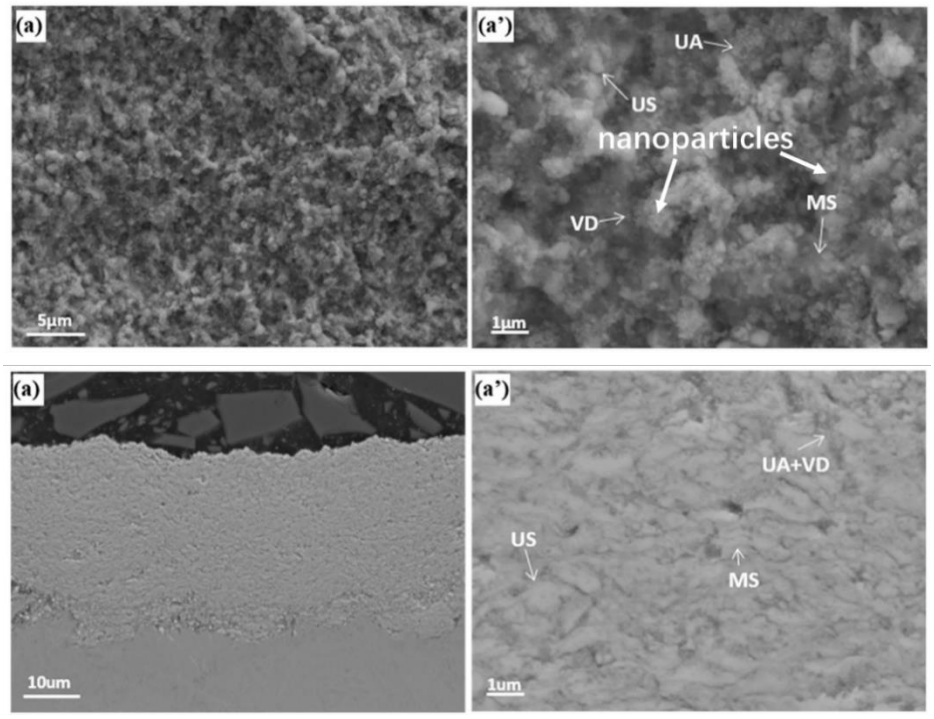

Fig. 1.30 Microstructures of the coating prepared by LPSPS reported by Song et al. [69]: (a)(a') surface image, (b)(b') cross-sectional image

(Preparation conditions: torch: bi-cathode torch, power: 61 kw, pressure: 6 mbar, powder: 3 mol% YSZ (D50=0.1 μm), plasma gas: Ar/He/H_2: 60 slpm/100 slpm/10 slpm, spraying distance: 350 mm)

1.3.3 Problems of the current LPSPS coatings

According to the limited literature on LPSPS, the LPSPS coatings commonly have a denser structure compared to the SPS coatings. However, the adhesion and mechanical strength of the current LPSPS coatings are quite low. More importantly, the structural characteristics of the LPSPS coating are still not fully understood. Its practical applications have not been fully studied or verified as well. The research of the LPSPS is still in the exploratory stage. A lot of work needs to be done in order to better understand this technology.

1.4 Introduction of SOFC

SOFC (solid oxide fuel cell) is a power generation device that directly converts chemical energy into electrical energy through electrochemical reactions. It uses hydrogen energy, natural gas, coal gas, etc., as fuel. SOFC can be widely applied in distributed power generation, transportation, mechanical power and other fields. In comparison with other fuel cells, the main advantages of SOFC are:

1) SOFC usually operates at a high temperature of 600 ℃~1000 ℃. A high working temperature can increase the electrochemical reaction rate. Therefore, SOFC does not need to use metal catalysts like Pt, which largely reduce its preparation cost.

2) Due to the all-solid structure, the shape of SOFC is not restricted. In addition to the traditional planar structure, it can also be designed into many different complex shapes such as tubular, corrugated, etc.

3) Since the materials used in the working parts of SOFC are solid oxides, it avoids material corrosion and electrolyte leakage that commonly occur in other fuel cells.

1.4.1 Working principle of SOFC

Fig. 1.31 shows the schematic of SOFC when hydrogen is used as a fuel. A typical SOFC mainly consists of an anode, a cathode and an electrolyte. Hydrogen enters into the anode layer, in which it undergoes a catalytic dissociation to generates hydrogen ions (H^+). Meanwhile, oxygen enters the cathode undergoes a catalytic dissociation to generate oxygen ions (O^{2-}). O^{2-} pass through the electrolyte layer driven by the gradient of the chemical potential or concentration of ions, and react with the hydrogen ions (H^+) to generate H_2O at the anode. Since the electrolyte is designed for electronic insulation, electrons can only pass through an external circuit from the anode to the cathode, thereby generating the current. The involved chemical reactions in the SOFC include:

$$H_2 + O^{2-} \rightarrow H_2O + 2e^- \quad anode$$

$$\frac{1}{2}\, O_2 + 2e^- \rightarrow O^{2-} \; cathode$$

$$H_2 + \frac{1}{2}\, O_2 \rightarrow H_2O \;\; overall \;\; reaction$$

It can be seen that water is the only product during the work of SOFC. Hence, SOFC is considered as an environment-friendly power generation.

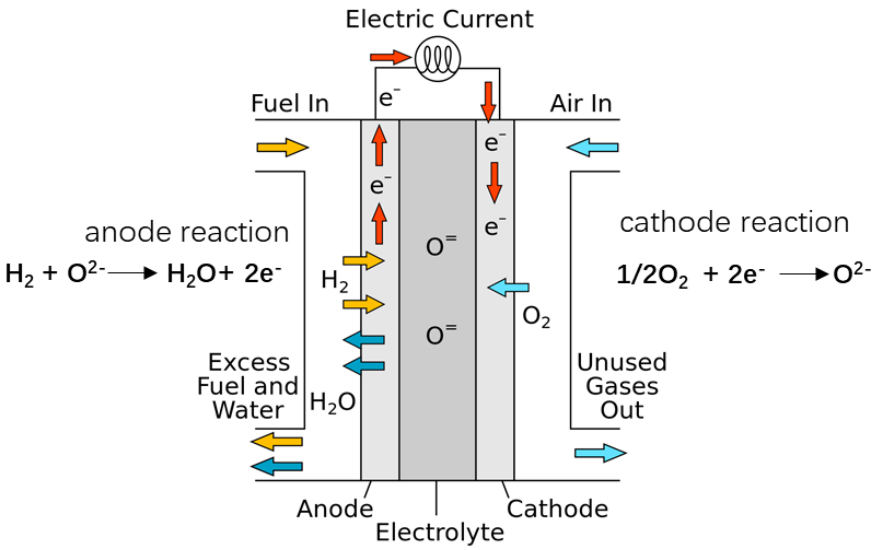

Fig. 1.31 Schematic of solid oxide fuel cell (SOFC) [70]

In practical conditions, SOFC generally relies on a support structure to increase its

mechanical properties. Figure 1.32 shows the typical support type of SOFC. The most commonly used type is using one of the anode, electrolyte and cathode as the support.This type of support is easily prepared. However, it typically has low mechanical properties and easily generates cracks as well. In particular, for the electrolyte support structure, the thick electrolyte will cause great ionic resistance and lower the ion conductivity. In order to overcome these shortcomings, researchers developed the metal support structure in recent years. This structure is achieved by a porous metal substrate (stainless steel), therefore, has better mechanical properties than ceramic-based support (anode, electrolyte and cathode support).

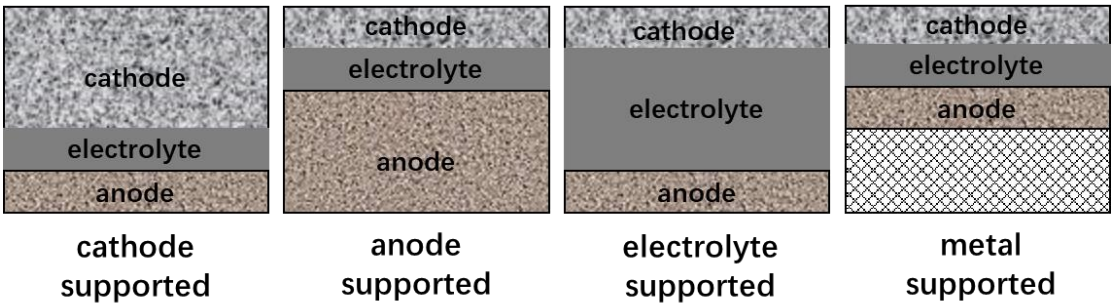

Fig. 1.32 Support structures for SOFC

1.4.2 Requirement of the components of SOFC

The cathode/ anode of SOF is required to have a porous structure in order to allow the oxidant/fuel to reach the interface of electrode-electrolyte. In addition, they must be a good conductor of electrons/ions as well as have a good reduction/oxidation catalytic activity. Currently, LaMnO3 with a perovskite structure is one of the main materials for the cathode. However, undoped $LaMnO_3$ is a P-type semiconductor with low conductivity (1-10 $S{\cdot}cm^{-1}$). In order to increase the conductivity, strontium is generally doped. Hence, lanthanum manganite doped with strontium--$La_{1-x}Sr_xMnO_3$ (x = 0.2, 0.3, or 0.4) -- is the most commonly used in the SOFC. Its electrical conductivity is about 130 $S{\cdot}cm^{-1}$ at 700 ° C. The anode is generally made up of two materials: the catalytic metal and the ceramic constituting the electrolyte. Ni-YSZ is the most commonly used anode material. The role of Ni is to conduct electricity and catalyze, and the role of YSZ is to

match the thermal expansion coefficient of the anode with the electrolyte and to expand the catalytic reaction area inside of the anode as well.

The electrolyte is the core component of the SOFC. In many cases, the performance of SOFC is greatly determined by the quality of the electrolyte. SOFC electrolyte first must have a high density (low gas permeability) to isolate the fuel and oxidant, preventing a short circuit in the cell. Second, it should have high ionic conductivity but low electronic conductivity. Third, it should be as thin as possible to reduce ionic resistance. Finally, it must have good chemical compatibility and thermal expansion matching with the electrodes. YSZ with a cubic fluorite structure is the most commonly used electrolyte material of SOFC [71-74]. It has high ionic conductivity, negligible electronic conductivity, excellent mechanical properties and good stability. YSZ with fluorite structure mainly has two forms: ZrO_2 doped with 3 mol% Y_2O_3 (3 mol% YSZ) and ZrO_2 doped with 8 mol% Y_2O_3 (8 mol%). Out of them, the 8 mol% YSZ is more frequently used since it has higher oxygen ion conductivity and higher stability in a wide oxygen partial pressure range of 10^{-15}~10^{5}Pa.

It should be noted that these advantages of YSZ mentioned above are based on the premise of high operating temperature. The effective operating temperature of the YSZ electrolyte usually exceeds 1000 °C. This is because the ion conductivity of the YSZ will dramatically decrease at intermediate temperatures (500 ℃-800 ℃). The high operating temperature not only greatly increased the preparation cost of the SOFC but also decreased the stability of the cell during the long-term operation. The main solution to this disadvantage of YSZ electrolyte is decreasing its thickness. In spite of that, the effective operating temperature of YSZ electrolyte is still difficult to be lower than 800 °C.

In order to further reduce the operating temperature of the cell, researchers are developing alternative electrolyte materials. Out of them, apatite-type lanthanum silicates having the general formula $La_{10-x}Si_6O_{27-1.5x}$ (LSO) is one of the most widely reported materials. It is considered to be a pure ion conductor in a wide range of oxygen

partial pressure[75, 76]. To further increase the sintering ability and ion conductivity of LSO, Sr, Al and Fe are usually doped [77-79]. Out of them, Sr is the most frequently used due to its similar ionic radius to La. It has been proved that Sr-doped LSO ($La_9SrSi_6O_{26.5}$) has an ionic conductivity of roughly 2.4-2.6 $mS \cdot cm^{-1}$ at 700 ℃. This performance was better than that of the undoped LSO prepared in the same conditions[80].

1.4.3 Preparation methods of metal-supported SOFC electrolyte

As mentioned above, due to the excellent mechanical properties, the metal-supported SOFC has greater potential value in the future. The metal-supported SOFC is typically fabricated by sequentially depositing the anode, the electrolyte and the cathode on a metal substrate. For that reason, traditional preparation methods for SOFC, such as screen printing and tape casting, are not suitable. This is because all of these methods involve very high process temperatures (>1400 ℃) the metal support cannot withstand. An effective solution is using plasma sprayings for the preparation. The plasma sprayings not only allow the powder to be sufficiently heated but also allow the substrate temperature to remain at a relatively low temperature (500 ℃-800 ℃). Next, the wider process window of the plasma sprayings makes them easier to meet the structural requirement of different components of SOFC. In addition, plasma sprayings have a much lower cost and higher efficiency than the traditional methods. Based on the above advantages, the topic of plasma spraying metal-supported SOFCs has attracted more and more attention from researchers[37, 81-84]

Out of these reports on metal-supported SOFCs, the study on the electrolyte attracted the most attention. This is because the electrolyte is the core component of the SOFC. In many cases, the performance of SOFC is greatly determined by the quality of the electrolyte. Currently, APS [82-84] and LPSPS [37, 81] have been widely reported to prepare the electrolyte of metal-supported SOFC. However, both of them have some limitations. For example, due to the inevitable existence of coarse pores, the APS electrolytes typically have a high thickness (> 60 μm) to ensure enough low gas

permeability. This inevitably increases the ionic resistance of the electrolyte. LPPS can achieve the preparation of the thin electrolyte by using agglomerated powders. However, the homogeneity of the coating microstructure is difficult to control [37], and its preparation cost is also much higher compared to APS. These issues can be effectively addressed by LPSPS. Firstly, thanks to the fine feed powder, the thickness of the LPSPS coating can be much lower than that of conventional plasma spraying. Secondly, it has been proved that LPSPS coating has a relatively high density due to the high particle velocity under low pressure. All of these features indicate that LPSPS has potential in the preparation of SOFC electrolytes.

1.5 Objectives of this thesis

As mentioned above, although the LPSPS coatings commonly have a denser structure compared to the SPS coatings, the structural characteristics of the LPSPS coating are still not fully understood. Considering that the structure of the plasma sprayed coating strongly depends on the spraying conditions, the first objective of this thesis is to study the effect of main spraying conditions on the structure of the LPSPS coating.

Also, as a technology under development, the practical application of LPSPS has not been fully studied or verified as well. Hence, the second objective of this thesis is to explore the potential application fields, especially the application in the SOFC electrolyte. It should be noted that only with a certain understanding of the structural characteristics of the coating can the application of the coating be foreseen. Therefore, the second objective is actually based on the realization of the first objective.

References

[1] http://www.amphardchrome.co.uk/plasma-spraying.php.

[2] C. Lamuta, G. Di Girolamo, L. Pagnotta, Microstructural, mechanical and tribological properties of nanostructured YSZ coatings produced with different APS process parameters, Ceramics International 41(7) (2015) 8904-8914.

[3] X.C. Zhong, Z.W. Liu, Y.S. Wu, M.T. Liu, D.C. Zeng, Nano-composite coatings with improved mechanical properties and corrosion resistance by thermal spraying, IOP Conference Series: Materials Science and Engineering 60 (2014) 012032.

[4] A.P. Malshe, W. Jiang, A.R. Dhamdhere, Nanostructured coatings for machining and wear-resistant applications, JOM 54(9) (2002) 28-30.

[5] W. Tian, Y. Wang, Y. Yang, Fretting wear behavior of conventional and nanostructured Al2O3–13wt%TiO2 coatings fabricated by plasma spray, Wear 265(11-12) (2008) 1700-1707.

[6] L. Wang, S. Liu, J. Gou, Q. Zhang, F. Zhou, Y. Wang, R. Chu, Study on the wear resistance of graphene modified nanostructured Al2O3/TiO2 coatings, Applied Surface Science 492 (2019) 272-279.

[7] M. Pourbafrani, R.S. Razavi, S.R. Bakhshi, M.R. Loghman-Estarki, H. Jamali, Effect of microstructure and phase of nanostructured YSZ thermal barrier coatings on its thermal shock behaviour, Surface Engineering 31(1) (2014) 64-73.

[8] Y. Wang, W. Tian, Y. Yang, Thermal shock behavior of nanostructured and conventional Al2O3/13 wt%TiO2 coatings fabricated by plasma spraying, Surface and Coatings Technology 201(18) (2007) 7746-7754.

[9] A.N. Banerjee, The design, fabrication, and photocatalytic utility of nanostructured semiconductors: focus on TiO2-based nanostructures, Nanotechnol Sci Appl 4 (2011) 35-65.

[10] F.-L. Toma, G. Bertrand, D. Klein, C. Coddet, C. Meunier, Nanostructured Photocatalytic Titania Coatings Formed by Suspension Plasma Spraying, Journal of Thermal Spray Technology 15(4) (2006) 587-592.

[11] P. Fauchais, R. Etchart-Salas, V. Rat, J.F. Coudert, N. Caron, K. Wittmann-Ténèze, Parameters Controlling Liquid Plasma Spraying: Solutions, Sols, or Suspensions, Journal of Thermal Spray Technology 17(1) (2008) 31-59.

[12] P. He, H. Sun, Y. Gui, F. Lapostolle, H. Liao, C. Coddet, Microstructure and properties of nanostructured YSZ coating prepared by suspension plasma spraying at low pressure, Surface and Coatings Technology 261 (2015) 318-326.

[13] Z. Chen, R.W. Trice, M. Besser, X. Yang, D. Sordelet, Air-plasma spraying colloidal solutions of nanosized ceramic powders, Journal of Materials Science 39(13) (2004) 4171-4178.

[14] L. Pawlowski, Suspension and solution thermal spray coatings, Surface and Coatings Technology 203(19) (2009) 2807-2829.

[15] F. Gitzhofer, E. Bouyer, and M.I. Boulos, Suspension Plasma Spray Deposition, U.S. Patent 5,609,921, 1997.

[16] L. Łatka, Thermal Barrier Coatings Manufactured by Suspension Plasma Spraying - A Review, Advances in Materials Science 18(3) (2018) 95-117.

[17] A. Ganvir, Microstructure and Thermal Conductivity of Liquid Feedstock Plasma Sprayed Thermal Barrier Coatings, university west, 2016.

[18] Y. Zhao, D. Li, X. Zhong, H. Zhao, L. Wang, F. Shao, C. Liu, S. Tao, Thermal shock behaviors of YSZ thick thermal barrier coatings fabricated by suspension and atmospheric plasma spraying, Surface and Coatings Technology 249 (2014) 48-55.

[19] Z. Tang, H. Kim, I. Yaroslavski, G. Masindo, Z. Celler, D. Ellsworth, Novel Thermal Barrier Coatings Produced by Axial Suspension Plasma Spray, International Thermal Spray Conference and Exposition, 2011, Hamburg, Germany.

[20] H.C. Chen, J. Heberlein, and R. Henne, integrated Fabrication Process for Solid Oxide Fuel Cells in a Triple Torch Plasma Reactor, Journal of Thermal Spray Technology, 9(3)(2000) -353.

[21] J. Fazilleau · C. Delbos · V. Rat · J. F. Coudert · P. Fauchais · B. Pateyron, Phenomena Involved in Suspension Plasma Spraying Part 1: Suspension Injection and Behavior, Plasma Chem Plasma Process (2006) 26:371–391.

[22] E. Aubignat, Contribution à la compréhension et à la maîtrise du procédé de projection plasma de suspensions céramiques. , 2014, Ph. D. Thesis, Belfort-Montbéliard, France, (in French).

[23] Marchand, C., et al., Liquid precursor plasma spraying: observation of liquid feedstock break-up, in Thermal Spray Corrsing Borders. Ed. E. Lugscheider, Pub. DVS-Verlag Düsseldorf, Germany (2008), e-proceedings, 2008.

[24] P. Fauchais, V. Rat, J.F. Coudert, R. Etchart-Salas, G. Montavon, Operating parameters for suspension and solution plasma-spray coatings, Surface and Coatings Technology 202(18) (2008) 4309-4317.

[25] J. Fazilleau, C. Delbos, V. Rat, J.F. Coudert, P. Fauchais, B. Pateyron, Phenomena Involved in Suspension Plasma Spraying Part 1: Suspension Injection and Behavior, Plasma Chemistry and Plasma Processing 26(4) (2006) 371-391.

[26] P. Fauchais, V. Rat, C. Delbos, J.F. Coudert, T. Chartier, L. Bianchi, Understanding of suspension DC plasma spraying of finely structured coatings for SOFC, IEEE Transactions on Plasma Science 33(2) (2005) 920-930.

[27] R. Rampon, O. Marchand, C. Filiatre, G. Bertrand, Influence of suspension characteristics on coatings microstructure obtained by suspension plasma spraying, Surface and Coatings Technology 202(18) (2008) 4337-4342.

[28] D. Soysal, A. Ansar, A new approach to understand liquid injection into atmospheric plasma jets, Surface and Coatings Technology 220 (2013) 187-190.

[29] D. Sen, S. Mazumder, J.S. Melo, A. Khan, S. Bhattyacharya, S.F. D'Souza, Evaporation Driven Self-Assembly of a Colloidal Dispersion during Spray Drying: Volume Fraction Dependent Morphological Transition, Langmuir 25(12) (2009) 6690-6695.

[30] M. Trunec, K. Maca, Advanced Ceramic Processes, Advanced Ceramics for Dentistry, Elsevier, 2014, pp. 123-150.

[31] Y. Zhao, Y. Wang, F. Peyraut, H. Liao, G. Montavon, M.-P. Planche, J. Ilavsky, A. Lasalle, A. Allimant, Evaluation of nano/submicro pores in suspension plasma sprayed YSZ coatings, Surface and Coatings Technology 378 (2019).

[32] O. Tingaud, A. Bacciochini, G. Montavon, A. Denoirjean, P. Fauchais, Suspension DC plasma spraying of thick finely-structured ceramic coatings: Process manufacturing mechanisms, Surface and Coatings Technology 203(15) (2009) 2157-2161.

[33] R. Jaworski, L. Pawlowski, F. Roudet, S. Kozerski, A.L. Maguer, Influence of Suspension Plasma Spraying Process Parameters on TiO2 Coatings Microstructure, Journal of Thermal Spray Technology 17(1) (2007) 73-81.

[34] C. Delbos, J. Fazilleau, V. Rat, J.F. Coudert, P. Fauchais, B. Pateyron, Phenomena Involved in Suspension Plasma Spraying Part 2: Zirconia Particle Treatment and Coating Formation, Plasma Chemistry and Plasma Processing 26(4) (2006) 393-414.

[35] X. Fan, G. Darut, M.P. Planche, C. Song, H. Liao, G. Montavon, Preparation and characterization of aluminum-based coatings deposited by very low-pressure plasma spray, Surface and Coatings Technology 380 (2019).

[36] B. Vautherin, M.P. Planche, R. Bolot, A. Quet, L. Bianchi, G. Montavon, Vapors and Droplets Mixture Deposition of Metallic Coatings by Very Low Pressure Plasma Spraying, Journal of Thermal Spray Technology 23(4) (2014) 596-608.

[37] J. Wen, C. Song, T. Liu, Z. Deng, S. Niu, Y. Zhang, L. Liu, M. Liu, Fabrication of Dense Gadolinia-Doped Ceria Coatings via Very-Low-Pressure Plasma Spray and Plasma Spray–Physical Vapor Deposition Process, Coatings 9(11) (2019).

[38] A. Joulia, G. Bolelli, E. Gualtieri, L. Lusvarghi, S. Valeri, M. Vardelle, S. Rossignol, A. Vardelle, Comparing the deposition mechanisms in suspension plasma spray (SPS) and solution precursor plasma spray (SPPS) deposition of yttria-stabilised zirconia (YSZ), Journal of the European Ceramic Society 34(15) (2014) 3925-3940.

[39] G. Mauer, A. Guignard, R. Vaßen, D. Stöver, Process diagnostics in suspension plasma spraying, Surface and Coatings Technology 205(4) (2010) 961-966.

[40] F.-L. Toma, G. Bertrand, S.O. Chwa, C. Meunier, D. Klein, C. Coddet, Comparative study on the photocatalytic decomposition of nitrogen oxides using TiO2 coatings prepared by conventional plasma spraying and suspension plasma spraying, Surface and Coatings Technology 200(20-21) (2006) 5855-5862.

[41] C. Zhang, U. Chaudhary, S. Das, A. Godavarty, A. Agarwal, Effect of Porosity on Photocatalytic Activity of Plasma-Sprayed TiO2 Coating, Journal of Thermal Spray Technology 22(7) (2013) 1193-1200.

[42] B. Bernard, A. Quet, L. Bianchi, A. Joulia, A. Malié, V. Schick, B. Rémy, Thermal insulation properties of YSZ coatings: Suspension Plasma Spraying (SPS) versus Electron Beam Physical Vapor Deposition (EB-PVD) and Atmospheric Plasma Spraying (APS), Surface and Coatings Technology 318 (2017) 122-128.

[43] F.-L. Toma, G. Bertrand, D. Klein, C. Meunier, S. Begin, Development of Photocatalytic Active TiO2Surfaces by Thermal Spraying of Nanopowders, Journal of Nanomaterials 2008 (2008) 1-8.

[44] Oberste Berghaus, J., et al., Suspension plasma spraying of nanoceramics using an axial injection torch Thermal Spray Connects: Explore Its Surfacing Potential ed E Lugscheider and CC Berndt (Düsseldorf, Germany: DVS) e-proceedings. Basel, Switzerland), ASM International, 2005.

[45] D. Zhou, J. Malzbender, Y.J. Sohn, O. Guillon, R. Vaßen, Sintering behavior of columnar thermal barrier coatings deposited by axial suspension plasma spraying (SPS), Journal of the European Ceramic Society 39(2-3) (2019) 482-490.

[46] A. Ganvir, R.F. Calinas, N. Markocsan, N. Curry, S. Joshi, Experimental visualization of microstructure evolution during suspension plasma spraying of thermal barrier coatings, Journal of the European Ceramic Society 39(2-3) (2019) 470-481.

[47] P. Sokołowski, P. Nylen, R. Musalek, L. Łatka, S. Kozerski, D. Dietrich, T. Lampke, L. Pawłowski, The microstructural studies of suspension plasma sprayed zirconia

coatings with the use of high-energy plasma torches, Surface and Coatings Technology 318 (2017) 250-261.

[48] A. Ganvir, V. Vaidhyanathan, N. Markocsan, M. Gupta, Z. Pala, F. Lukac, Failure analysis of thermally cycled columnar thermal barrier coatings produced by high-velocity-air fuel and axial-suspension-plasma spraying: A design perspective, Ceramics International 44(3) (2018) 3161-3172.

[49] B. Xiao, X. Huang, T. Robertson, Z. Tang, R. Kearsey, Sintering resistance of suspension plasma sprayed 7YSZ TBC under isothermal and cyclic oxidation, Journal of the European Ceramic Society (2020).

[50] A. Ganvir, N. Markocsan, S. Joshi, Influence of Isothermal Heat Treatment on Porosity and Crystallite Size in Axial Suspension Plasma Sprayed Thermal Barrier Coatings for Gas Turbine Applications, Coatings 7(1) (2016).

[51] Y. Zhao, L. Wang, J. Yang, D. Li, X. Zhong, H. Zhao, F. Shao, S. Tao, Thermal Aging Behavior of Axial Suspension Plasma-Sprayed Yttria-Stabilized Zirconia (YSZ) Thermal Barrier Coatings, Journal of Thermal Spray Technology 24(3) (2014) 338-347.

[52] X.F. Zhang, K.S. Zhou, M. Liu, C.M. Deng, C.G. Deng, J. Mao, Z.Q. Deng, Mechanisms governing the thermal shock and tensile fracture of PS-PVD 7YSZ TBC, Ceramics International 44(4) (2018) 3973-3980.

[53] S. Goel, S. Björklund, N. Curry, U. Wiklund, S.V. Joshi, Axial suspension plasma spraying of Al2O3 coatings for superior tribological properties, Surface and Coatings Technology 315 (2017) 80-87.

[54] M. Marr, J. Kuhn, C. Metcalfe, J. Harris, O. Kesler, Electrochemical performance of solid oxide fuel cells having electrolytes made by suspension and solution precursor plasma spraying, Journal of Power Sources 245 (2014) 398-405.

[55] D. Waldbillig, O. Kesler, Electrochemical testing of suspension plasma sprayed solid oxide fuel cell electrolytes, Journal of Power Sources 196(13) (2011) 5423-5431.

[56] J.V. Heberlein, P. Fauchais, M.I. Boulos, thermal spray fundamental, 2014.

[57] https://www.mettech.com/coating-equipment/axial-III-plasma-spray-system.php.

[58] M. Marr, O. Kesler, Permeability and Microstructure of Suspension Plasma-Sprayed YSZ Electrolytes for SOFCs on Various Substrates, Journal of Thermal Spray Technology 21(6) (2012) 1334-1346.

[59] K. von Niessen, M. Gindrat, Plasma Spray-PVD: A New Thermal Spray Process to Deposit Out of the Vapor Phase, Journal of Thermal Spray Technology 20(4) (2011) 736-743.

[60] M.G. J. L. Dorier, Ch. Hollenstein, Plasma Jet Properties in a New Spraying Process at Low Pressure for Large Area Thin Film Deposition, International Thermal Spray Conference (2001) 28-30.

[61] A. Hospach, G. Mauer, R. Vaßen, D. Stöver, Characteristics of Ceramic Coatings Made by Thin Film Low Pressure Plasma Spraying (LPPS-TF), Journal of Thermal Spray Technology 21(3-4) (2012) 435-440.

[62] Y. Niu, H. Wang, H. Li, X. Zheng, C. Ding, Dense ZrB2–MoSi2 composite coating fabricated by low pressure plasma spray (LPPS), Ceramics International 39(8) (2013) 9773-9777.

[63] Y.-p. Wang, J.-t. Gao, W. Chen, C.-x. Li, S.-l. Zhang, G.-j. Yang, C.-j. Li, Development of ScSZ Electrolyte by Very Low Pressure Plasma Spraying for High-Performance Metal-Supported SOFCs, Journal of Thermal Spray Technology 29(1-2) (2019) 223-231.

[64] B. Liang, H. Chen, C.X. Ding, Low Temperature Transformation of 3 mol% Yttria Stabilized Zirconia Coatings Deposited by Air Plasma Spraying, Materials Science Forum 620-622 (2009) 413-416.

[65] Z. Salhi, D. Klein, P. Gougeon, C. Coddet, Development of coating by thermal plasma spraying under very low-pressure condition <1mbar, Vacuum 77(2) (2005) 145-150.

[66] M. Goral, S. Kotowski, A. Nowotnik, M. Pytel, M. Drajewicz, J. Sieniawski, PS-PVD deposition of thermal barrier coatings, Surface and Coatings Technology 237 (2013) 51-55.

[67] James D Fleetwood, Solid oxide fuel cell electrolytes produced via very low pressure suspension plasma spray and electrophoretic deposition, Purdue University, 2014.

[68] P. He, Etude du développement de la projection plasma sous très basse pression, Université de Technologie de Belfort-Montbéliard, 2014.

[69] C. Song, Potentialité de préparation de revêtements en céramiques par la projection plasma sous basse pression, Université de Technologie de Belfort-Montbéliard, 2018.

[70] https://en.wikipedia.org/wiki/Solid_oxide_fuel_cell.

[71] Y. Chen, S. Omar, A.K. Keshri, K. Balani, K. Babu, J.C. Nino, S. Seal, A. Agarwal, Ionic conductivity of plasma-sprayed nanocrystalline yttria-stabilized zirconia electrolyte for solid oxide fuel cells, Scripta Materialia 60(11) (2009) 1023-1026.

[72] S. Dwivedi, Solid oxide fuel cell: Materials for anode, cathode and electrolyte, International Journal of Hydrogen Energy (2020).

[73] S. Badwal, Zirconia-based solid electrolytes: microstructure, stability and ionic conductivity, Solid State Ionics 52(1-3) (1992) 23-32.

[74] J. Molenda, K. Świerczek, W. Zając, Functional materials for the IT-SOFC, Journal of Power Sources 173(2) (2007) 657-670.

[75] T. Nakao, A. Mineshige, M. Kobune, T. Yazawa, H. Yoshioka, Chemical stability of La10Si6O27 and its application to electrolytes for solid oxide fuel cells, Solid State Ionics 179(27-32) (2008) 1567-1569.

[76] A. Shaula, V. Kharton, F. Marques, Ionic and electronic conductivities, stability and thermal expansion of La10−x(Si,Al)6O26±δ solid electrolytes, Solid State Ionics 177(19-25) (2006) 1725-1728.

[77] X.G. Cao, S.P. Jiang, Identification of oxygen reduction processes at (La,Sr)MnO3 electrode/La9.5Si6O26.25 apatite electrolyte interface of solid oxide fuel cells, International Journal of Hydrogen Energy 38(5) (2013) 2421-2431.

[78] X.G. Cao, S.P. Jiang, Effect of Sr and Al or Fe co-doping on the sinterability and conductivity of lanthanum silicate oxyapatite electrolytes for solid oxide fuel cells, International Journal of Hydrogen Energy 39(33) (2014) 19093-19101.

[79] Y. Ma, N. Fenineche, O. Elkedim, M. Moliere, H. Liao, P. Briois, Synthesis of apatite type La10−xSrxSi6O27−0.5x powders for IT-SOFC using sol–gel process, International Journal of Hydrogen Energy 41(23) (2016) 9993-10000.

[80] C. Bonhomme, S. Beaudet-Savignat, T. Chartier, A. Maître, A.-L. Sauvet, B. Soulestin, Sintering kinetics and oxide ion conduction in Sr-doped apatite-type lanthanum silicates, La9Sr1Si6O26.5, Solid State Ionics 180(36-39) (2009) 1593-1598.

[81] C. Zhang, H.L. Liao, W.Y. Li, G. Zhang, C. Coddet, C.J. Li, C.X. Li, X.J. Ning, Characterization of YSZ Solid Oxide Fuel Cells Electrolyte Deposited by Atmospheric Plasma Spraying and Low Pressure Plasma Spraying, Journal of Thermal Spray Technology 15(4) (2006) 598-603.

[82] W.Z. Wang, F. Sun, X.P. Guo, H.L. Liao, O. Elkedim, J.C. Liang, Effect of substrate surface temperature on the microstructure and ionic conductivity of lanthanum silicate coatings deposited by plasma spraying, Surface and Coatings Technology 205(12) (2011) 3665-3670.

[83] W. Gao, H.-L. Liao, C. Coddet, Effect of Gun Current on Electrical Properties of Atmospheric Plasma-Sprayed Lanthanum Silicate Coatings, Journal of Thermal Spray Technology 22(7) (2013) 1103-1108.

[84] W. Gao, H. Liao, C. Coddet, Effect of feedstock powder characteristics on microstructure and mechanical properties of lanthanum silicate coatings deposited by atmospheric plasma spraying, Applied Surface Science 254(17) (2008) 5548-5551.

Chapter 2 Experimental materials and methods

Chapter 2 Experimental materials and methods

2.1 LPSPS equipment

In this thesis, a LPSPS system was developed to prepare all studied coatings. The schematic of the LPSPS system is shown in Fig. 2.1, and its photos are shown in Fig. 2.2. The LPSPS system was developed on the platform of LPPS in LERMPS lab [1-3]. A peristaltic pump was used to deliver the suspension. Meanwhile, a magnetic agitator continuously worked to prevent the sedimentation of the suspension. The spraying system was placed in a vacuum tank. An axial bi-cathode plasma torch was used for spraying. The plasma torch was mounted on a programmable 6-axis robot (ABB IRB 1400). The details of this torch are mentioned in section 1.3.2. During the spraying process, two pumping groups were used to pump the tank to a low-pressure environment.

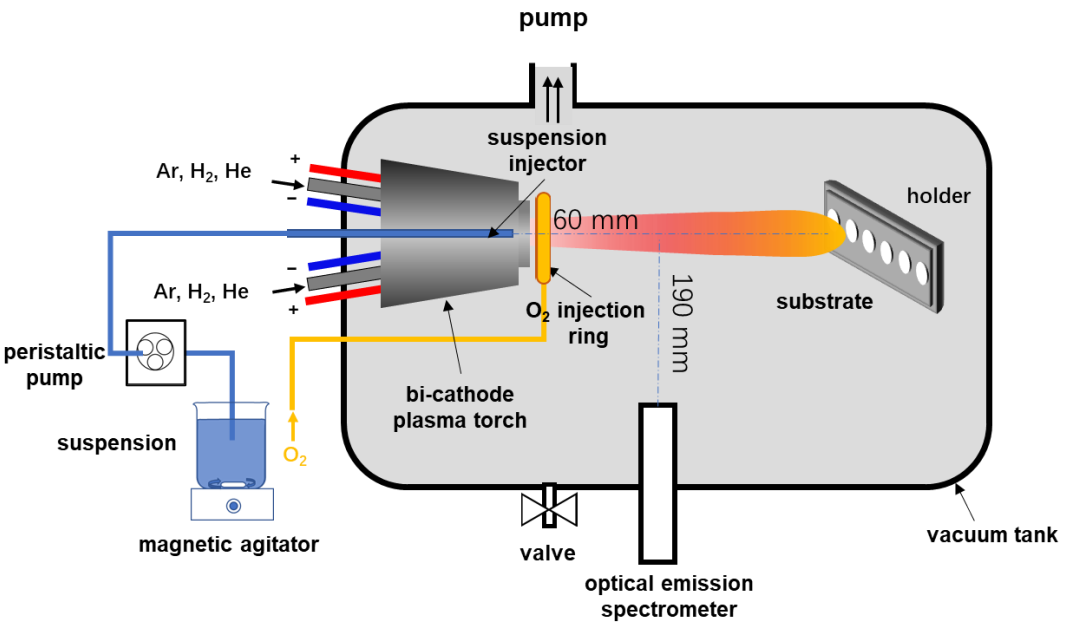

Fig. 2.1 Schematic of LPSPS system

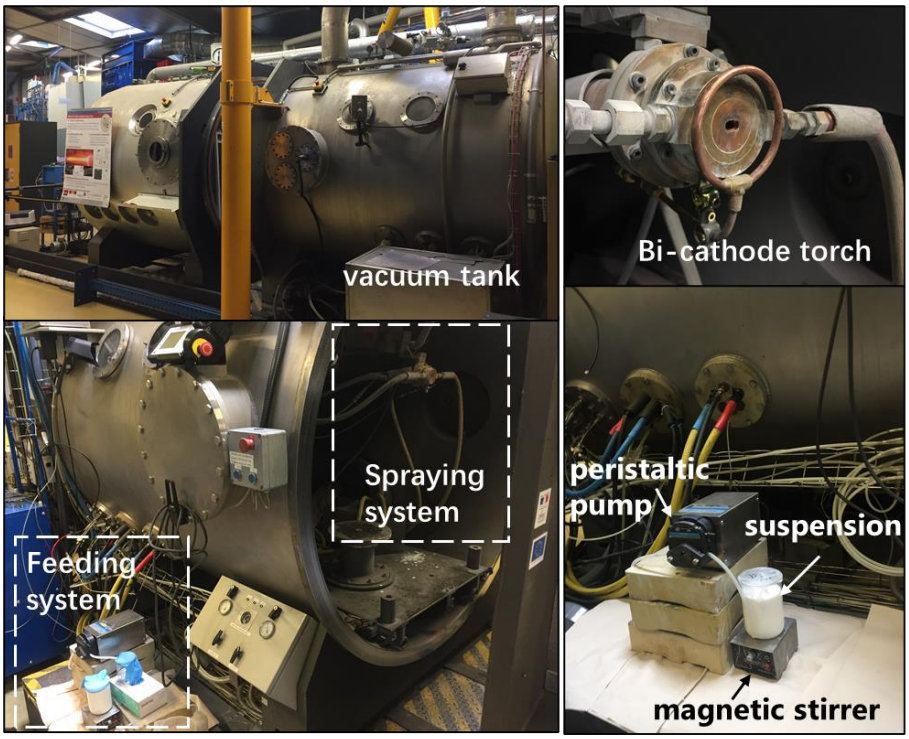

Fig. 2.2 Photos of LPSPS system

2.2 Materials

2.2.1 Powders

Tree kinds of powder were used in this thesis. In chapter 3 and 4, commercially available 8 wt% YSZ (8 wt% Y_2O_3 + ZrO_2) powder (Qingdao Tianyao Industry Company Ltd, Qingdao, China) in size of D50 ~150 nm was used to prepare the YSZ coating. In Chapter 5, commercially available 8 mol% YSZ (8 mol% Y_2O_3 + ZrO_2) powder (Shanghai Yaotian New Material Technology Co., Ltd., Shanghai, China) in size of D50 ~ 150 nm was used to prepare the YSZ electrolyte coating. At the same time, customised $La_9SrSi_6O_{26.5}$ (LSSO) powder (Qingdao Tianyao Industry Company Ltd, Qingdao, China) in size of 500 nm was used to prepare the lanthanum silicate electrolyte coating. The morphologies of the above powders are shown in Fig. 2.3

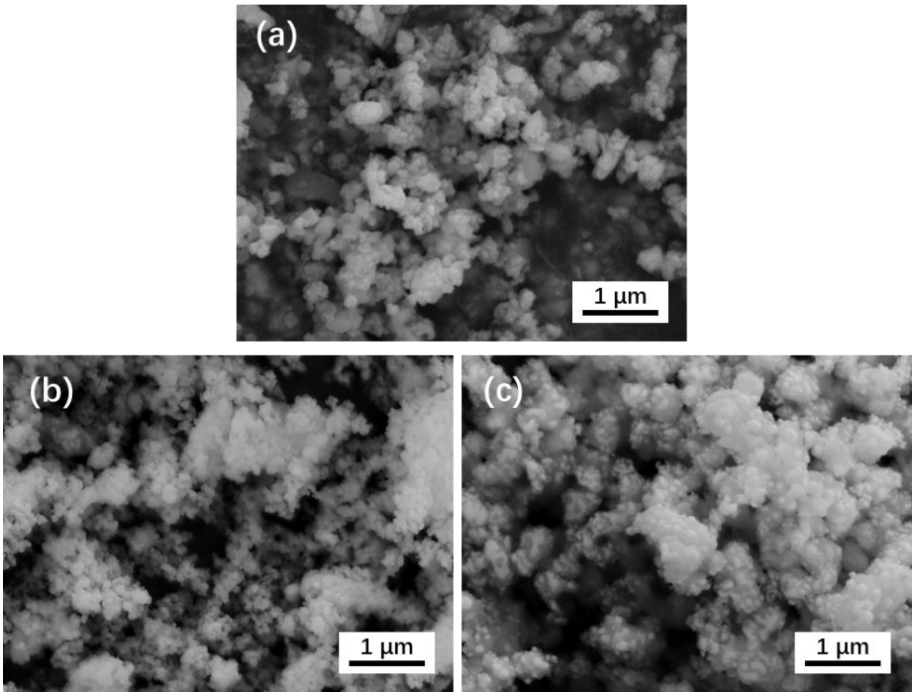

Fig. 2.3 Morphologies of the used powders;(a) 8 wt% YSZ powder, (b) 8 mol% YSZ powder, (c) $La_9SrSi_6O_{26.5}$ powder

2.2.2 Suspension preparation

In order to prevent the sedimentation of suspension during the spraying process, a dispersant (DOLAPIX ET 85, Zschimmer & Schwarz, Germany) was added during the suspension preparation. Firstly, the dispersant was dissolved in ethanol and then mixed with magnetic stirring for 5 min. Thereafter, the powders were added to the prepared solution with continuous magnetic stirring. At last, the suspension was agitated by ultrasound for 15 min. In order to optimise the dispersant content for each suspension, prior to the spraying, a series of sedimentation tests were carried out, as shown in Fig. 2.4. Given the practical spraying time, the sedimentation test only lasted 24 hours. Under the premise that no obvious sediment was observed, the dispersant content should be as low as possible to reduce the viscosity of the suspension. Based on the above criteria, the optimal dispersant content for each suspension is presented in Table 2.1.

After the dispersant content was determined, a series of suspensions were prepared according to the requirements. The preparation process of the suspensions was: first, the dispersant was dissolved in ethanol or deionised water and then mixed via magnetic stirring for five minutes. Thereafter, powders were added to the prepared solution with continuous magnetic stirring. Finally, the suspensions were agitated by ultrasound for fifteen minutes. During the spraying process, the suspension was continuously stirred with the magnetic stirrer to prevent the sedimentation of the powder.

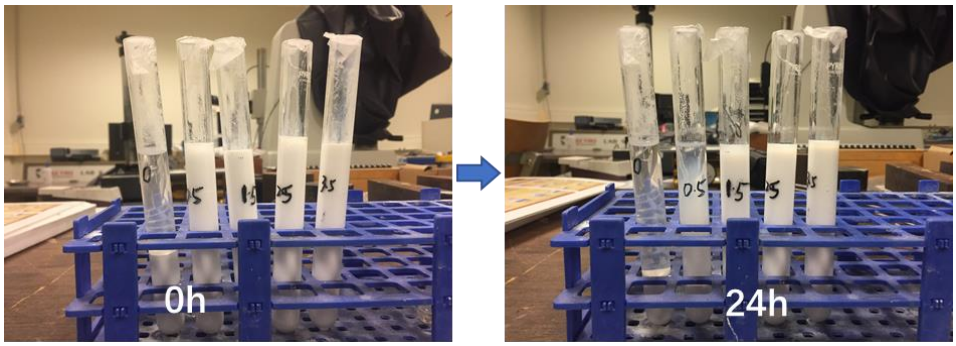

Fig. 2.4 Sedimentation test of the suspension

Table 2.1 Dispersant content of the suspensions

	8 wt% YSZ suspension (ethanol solvent)	8 wt% YSZ suspension (water solvent)	8 mol% YSZ suspension (ethanol solvent)	$La_9SrSi_6O_{26.5}$ suspension (ethanol solvent)
Dispersant Content (wt%)	1.5	1.5	0.5	0.5
Solid content of the suspension	5wt%, 15 wt%, 25 wt%	15 wt%	15 wt%	15 wt%

2.2.3 Substrates

Inconel 738 in size of Φ 25mm × 5mm was used as the substrate of 8 wt% YSZ coating. Prior to the deposition of the coating, a NiCoCrAlYTa bond coating (120 μm thickness) was prepared by APS, the powder used was the commercial NiCoCrAlYTa

powder (Sulzer-Metco, Amdry 997, 5-37 μm). The spraying parameter for the bond coating is shown in Table 2.2

Table 2.2 Spraying parameters of NiCoCrAlYTa bond coating

Spraying parameters	
Current(A)	600
Voltage(V)	72
Ar(L/min)	65
H_2 (L/min)	11
Carrier gas (L/min)	2
Feeding rate (g/min)	43
Spraying distance(mm)	110

Porous stainless steel in size of Φ 20 mm × 1 mm was used as metal support for SOFC electrolyte. Prior to the deposition of the electrolyte, Gadolinia-doped ceria (GDC) with 30-50 μm thickness as an anode layer was deposited on the porous stainless steel using APS. The schematic of the deposition steps of electrolyte coating is shown in Fig. 2.5, and the spraying parameters of the anode layer is displayed in Table 2.3.

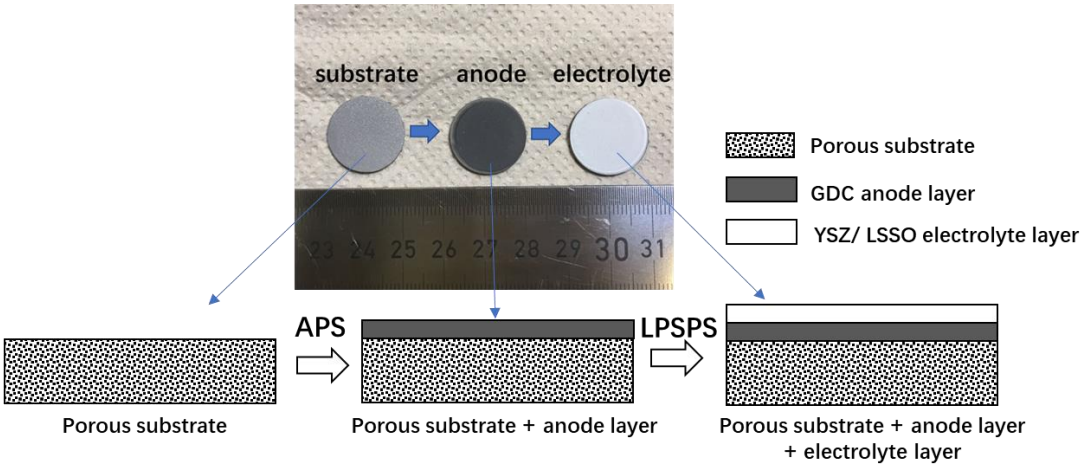

Fig. 2.5 Schematic of the deposition process of the electrolyte

Table 2.3 Spraying parameters of GDC anode coating

Spraying parameters	
Current(A)	500
Voltage(V)	70
Ar(L/min)	50
H_2(L/min)	5
Carrier gas (L/min)	2
Feeding rate (g/min)	20
Spraying distance(mm)	100

2.3 Coatings preparation

This thesis involves two environmental atmospheres (argon versus air) and multiple environmental pressures (980 mbar, 600 mbar, 400 mbar, 200 mbar and 3 mbar) for the coating preparation. These are all achieved through the vacuum tank. For the coating preparation under 980 mbar, the vacuum tank was open, allowing the coating to be prepared in the air. For the coating preparation under low pressures (from 600 mbar to 3 mbar) in the argon, prior to the coating deposition, the vacuum tank was first pumped to the minimal pressure of 1 mbar. Thereafter, the tank was filled with argon until the set pressure was reached. For the coating preparation under 200 mbar in the air, the vacuum tank was pumped to 200 mbar, making the tank remain at 200 mbar, and then the pump was turned off. During the spraying process, the pressures in the vacuum chamber were automatically maintained by the gas valve.

The substrates were fixed on a homemade holder, and the coatings were deposited by the spray torch moving in front of the substrates. Prior to the coating deposition, the substrates were first preheated at 600°C (8 wt% YSZ coatings) and 300°C (electrolyte

coatings) using the pure plasma jet. The substrate temperatures were tested with a K-type thermocouple in contact with the back of the substrates. Thereafter, the suspensions were injected to start the deposit of the coatings. In order to more clearly distinguish the difference of the coating prepared by different spraying conditions, the target thickness of the coating in the optimization stage of the spraying condition (chapter 3 and chapter 4) is 300-600 μm.

It should be noted that due to the design problems, the spray torch was gradually eroded as the experiment progressed. In order to extend the service life of the spray torch, in the later stage of this thesis work, the spraying time or torch current was reduced.

2.4 Characterisation methods

2.4.1 Microstructure of the coatings and powders

The microstructure of the coatings and powders were observed using an optical microscope from Nikon (Japan) and a scanning electron microscope (SEM) (JSM-7800F, JEOL, Japan). Before the observation, a metallisation treatment with gold or carbon vapour was performed using a SCD 005/CEA035 sputter coater (BAL-TEC, Switzerland).

2.4.2 Porosity of the coatings

The coating porosity was calculated through image analysis by the software ImageJ. In that process, the images were set to a high contrast degree to make sure that the pores were shown in white, and the matrix was shown in black, as shown in Fig. 2.6. The porosity was defined as the pixel ratio of the white area to the entire image. For each measurement, ten cross-sectional images of the coating at 1000 × magnification in different regions were captured by SEM. It needs to be pointed out that SPS coating normally contains many pores that are filled by nanoparticles. There are still

pores at nanoscale size existing between the stacked nanoparticles. However, it is difficult to be calculated these pores through image analysis. To simplify the calculation process, in the thesis, these filled pores were regarded as empty pores to calculate the porosity. In addition, in order to reduce errors, the cracks and the column interfaces in the coating were not considered in the coating porosity measurements.

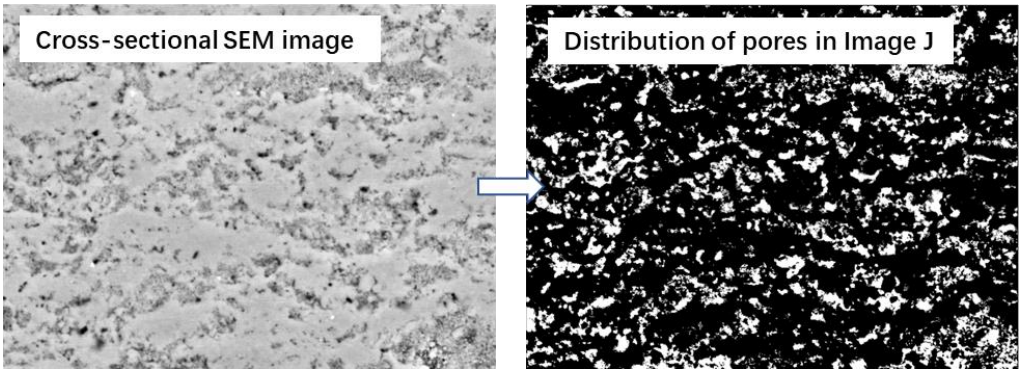

Fig. 2.6 Measurement of coating porosity through image analysis

2.4.3 Surface roughness of the coatings

The surface roughness (Ra) was measured using a surface roughness tester (SJ-210 SERIES, Mitutoyo, Japan). Each coating was measured ten times in different regions; the average value of the above results was taken as the final surface roughness of the coating.

2.4.4 Phase composition of the powders and the coatings

The phase composition of the powders and the coatings were characterised by X-ray diffraction (XRD) (Bruker AXS D8 Focus, Germany) with CoKα radiation (λ=1.7889 Å). An angular range of 20 ° to 80 ° (in 2θ) was scanned in steps of 0.02 °.

2.4.5 Mechanical properties of the coatings

Traditional testing methods of mechanical properties (hardness and elastic modulus) are based on macro- or micro- indentation. They are not suitable for thin coatings due to the large indentation area. In addition, their accuracy is relatively poor and cannot accurately reflect the characteristics of the finely structured coating. In contrast, the

indentation area of nanoindentation is much smaller. It can reach a pressure depth as small as nanometres (0.1~100nm) due to the ultra-low load applied. During the test process, a load-displacement curve is drawn by recording the change of the load and indentation depth, as shown in Figure 2.7, where P_{max} is the maximum load, $_{max}$ is the maximum displacement, S is the contact stiffness and h_f is the final depth. The whole test process is precisely controlled by a computer.

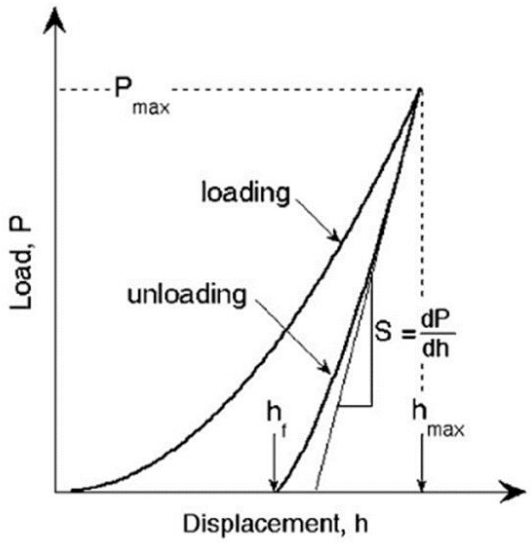

Fig. 2.7 Schematic of the load-displacement curve of the nanoindentation test

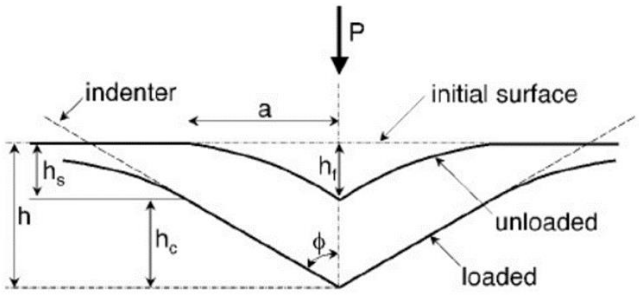

Fig. 2.8 Schematic of the unloading process of the indentation test

Fig. 2.8 shows the schematic of the unloading process of the indentation test according to the definition of hardness and elastic modulus in the classic elastoplastic deformation theory. The hardness *H* and elastic modulus *E* can be calculated based on the equations below [4].

$$H = \frac{F_{max}}{A(hc)}$$

$$E_r = \frac{1-\nu^2}{E} + \frac{1-\nu_i^2}{E_i}$$

$$S = 2\beta E_r \sqrt{\frac{A(hc)}{\pi}}$$

F_{max} is the peak indentation load, $A(hc)$ is the projected area of the indentation at the contact depth hc. E_r is the effective elastic modulus. E_i is the elastic modulus of the indenter material, ν is the Poisson's ratio of the tested material, ν_i is the Poisson's ratio of indenter material, *S* is the unloading stiffness and β is a constant determined by the geometry of the indenter. For general materials, ν is typically around 0.3, and for a diamond indenter, E_i is 1140 GPa and ν_i is 0.07.

In this thesis, a nanoindenter (Hysitron, U.S.A.) was used to measure the mechanical properties of the coatings. The cross-sections of the coating were selected as the measurement positions for nanoindentation. The loading and unloading rates were 200 mN/min and the pause time at the maximum load (10 mN) was 10 s. Ten different areas were measured to calculate the average of each mechanical property.

2.4.6 Diagnosis of plasma jet characteristics

In this thesis, the Jobin-Yvon Triax 190 type optical emission spectrometer equipped with a CCD (Charge Coupled Devices) camera was employed to diagnose the characteristics of the plasma jet, as shown in Fig. 2.9. Optical emission spectroscopy (OES) is a diagnostic method widely used to diagnose the characteristics of plasma jets [5, 6]. This technique is based on the detection of light signals emitted by excited atoms or excited ions when they are de-excited by radiative mechanisms. The plasma jet has an ultra-high temperature (＞10,000K), when the suspension is injected into it, it is partially or even mostly decomposed into atoms or ions. The excited atoms or ions will create an emission spectrum after their transition from a high energy state to a low energy state. Due to the different atomic energy levels, each element produces unique characteristic emission spectral lines. Hence, the chemical species of the plasma jet can

be determined by the type of the spectral line, and their content can be determined by the intensity of the spectral line as well. According to this principle, the intensity of the spectral line can also reflect the enthalpy of the plasma jet. The higher the intensity of the spectral line, the higher the enthalpy of the plasma jet. In short, the OES can provide information related to the chemical species within the plasma jet as well as the enthalpy of the plasma jet.

In this study, the resolution of the spectrometer is 0.3 nm, and its focal length is 190 mm. Therefore, in order to measure the chemical species in the centre of the plasma jet, the head of the detector was 190 mm far from the axial line of the plasma jet centre and fixed at a spraying distance of 60 mm (the shortest spray distance that the detector could reach). The installation schematic of the optical emission spectrometer is shown in Fig. 2.1.

Fig. 2.9 Jobin-Yvon Triax 190 optical emission spectrometer.

2.4.7 Gas permeability of the electrolytes

A homemade device was used to measure the gas permeability of the electrolytes, as shown in Fig. 2.10. The principle of measurement is to establish a constant pressure difference on both sides of the coating sample and simultaneously measure the gas leakage flow. The gas permeability can be calculated according to Darcy's law:

$$k = \frac{Q\eta}{A \cdot \Delta P} \cdot \mu$$

Where k is the specific permeability (m^2); Q is the gas leakage flow ($m^3 \cdot s^{-1}$); η is the thickness of the coating (m); A is the cross-sectional area of the gas passing through the coating (m^2); ΔP is the pressure difference on both sides of the coating (Pa); and μ is the dynamic viscosity of gas (Pa·s). Due to the high sensitivity of hydrogen to gas leakage (especially for minor defects), hydrogen was used as the test gas to examine the gas permeability of the electrolytes. The measurement process is as follows: first, the coating was deposited on the porous stainless steel and then sealed with epoxy resin in the sealing fixture. Thereafter, one side of the sample was connected to 2 bar hydrogen, and the other side was connected to the atmosphere. Hydrogen leakage flow was measured by an electromagnetic flowmeter (Drycall Ml-500, U.S.A.). In order to increase the reliability of the measurements, three parallel samples were selected for each coating, and each parallel sample was measured three times.

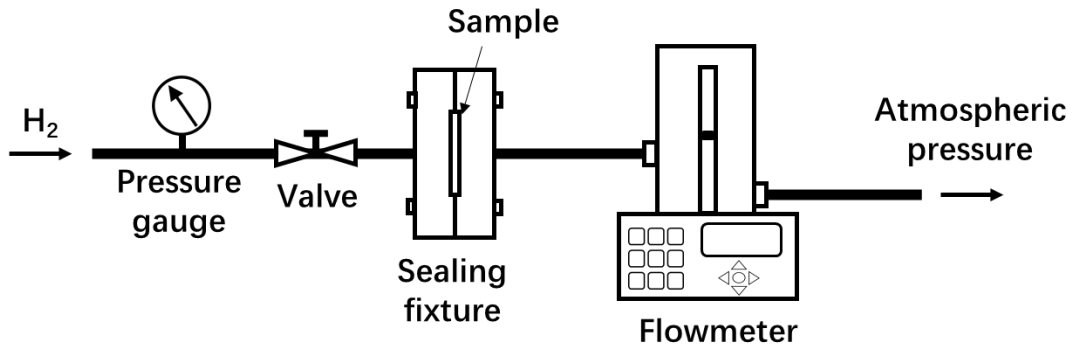

Fig. 2.10 Schematic of the gas permeability measurement of the electrolyte

References

[1] B. Vautherin, M.P. Planche, R. Bolot, A. Quet, L. Bianchi, G. Montavon, Vapors and Droplets Mixture Deposition of Metallic Coatings by Very Low Pressure Plasma Spraying, Journal of Thermal Spray Technology 23(4) (2014) 596-608.

[2] N. Zhang, F. Sun, L. Zhu, M.P. Planche, H. Liao, C. Dong, C. Coddet, Measurement of Specific Enthalpy Under Very Low Pressure Plasma Spray Condition, Journal of Thermal Spray Technology 21(3-4) (2012) 489-495.

[3] B. Vautherin, M.P. Planche, A. Quet, L. Bianchi, G. Montavon, Manufacturing of composite titanium-titanium nitride coatings by reactive very low pressure plasma spraying (R-VLPPS), Journal of Physics: Conference Series 550 (2014) 012035.

[4] W.C. Oliver, G.M. Pharr, Measurement of hardness and elastic modulus by instrumented indentation: Advances in understanding and refinements to methodology, J. Mater. Res., Vol. 19, No. 1, Jan 2004.

[5] K. von Niessen, M. Gindrat, Plasma Spray-PVD: A New Thermal Spray Process to Deposit Out of the Vapor Phase, Journal of Thermal Spray Technology 20(4) (2011) 736-743.

[6] L. Zhu, N. Zhang, F. Sun, R. Bolot, M.-P. Planche, H. Liao, C. Coddet, Thin Yttria-Stabilized Zirconia Coatings Deposited by Low-Energy Plasma Spraying Under Very Low Pressure Condition, Journal of Thermal Spray Technology 20(5) (2011) 1118-1124.

Chapter 3 Effect of environmental pressure on the microstructure of the coating prepared by suspension plasma spraying

Chapter 3: Effect of environmental pressure on the microstructure of the coating prepared by suspension plasma spraying

In this chapter, YSZ coatings are prepared by using suspension plasma spraying under environmental pressure varying from 980 mbar to 3 mbar. The influences of environmental pressure on plasma jet characteristics, coating microstructure, coating porosity and coating phase composition are investigated. At the same time, the pressure of LPSPS in this thesis is optimized, and the deposition mechanism of LPSPS coating is proposed.

3.1 Introduction

Conventional SPS techniques are based on the platform of APS. Therefore, the deposition process of the coating is limited under atmospheric pressure. In fact, the environmental pressure has a significant effect on the coating deposition, which has been demonstrated between the APS coatings and the LPPS coatings [1-3]. First, the velocity of the deposited particle is significantly increased as the pressure decreases [4]. It means that the coating prepared under lower pressure is generally more homogeneous and denser. Second, the plasma jet is lengthened as the pressure decreases, which allows the particles to be heated more sufficiently, and also enables the deposition of the coating on the complex parts such as turbine blades [5, 6].

It is worth noting that the laws mentioned above are all based on the understanding of the effect of pressure on powder behaviour in the plasma jet. However, the effect of pressure on suspension behaviour in the plasma jet has not been fully investigated or verified yet. In addition, pressure is the crucial parameter that distinguishes LPSPS and SPS. Hence, pressure should be the first parameter to be studied for the development of the LPSPS. With these in mind, in this chapter, yttria-stabilized zirconia (YSZ) coatings are prepared by suspension plasma spraying under different pressures, the effect

of pressure on plasma jet, coating microstructure, coating porosity and coating phase composition are investigated.

3.2 Preparation conditions of the coatings

In this chapter, the environmental pressure varies from atmospheric pressure (980 mbar) to ultra-low pressure (3 mbar) for the coating preparation. The detailed spraying parameters are presented in Table 3.1.

Table 3.1 Experimental parameters of SPS YSZ coating under different environmental pressures

Parameters	980 mbar	600 mbar	400 mbar	200 mbar	3 mbar
Environmental atmosphere	air	argon	argon	argon	argon
Current (A)	700×2	700×2	700×2	700×2	700×2
Voltage (V)	54	54	54	54	54
Ar (L/min)	80	80	80	80	89
H_2 (L/min)	20	20	20	20	20
Solvent type	ethanol	ethanol	ethanol	ethanol	ethanol
Solid concentration (wt%)	15	15	25	25	25
Suspension flow (mL/min)	55	55	35	35	35
Spraying distance (mm)	50	60	80	100	250
Substrate temperature (℃)	650-720	650-720	650-720	650-720	650-720
Spraying time (min)	13	13	13	13	20
Result	√	√	√	√	×

*remark: √: no coating spallation; ×: coating spallation

Due to technical problems, it is not possible for the case of 980 mbar to achieve an argon atmosphere, so it uses an atmospheric atmosphere. Similarly, in the case of 980 mbar and 600 mbar, the suspension at a low flow rate (35 mL/min) cannot enter

the plasma jet smoothly. Therefore, the suspension flow rate is increased in these two cases. However, in order to ensure the same powder feeding rate, the solid content of both cases is accordingly reduced. The spraying distance in table 3.1 is the shortest distance the substrate can withstand in the current conditions.

3.3 Characteristics of the plasma jets

Fig. 3.1 shows the shapes of the plasma jets under different pressures with the suspension injected. It can be seen that the plasma jet is broadened and elongated with the pressure decreasing. The thin surrounding gas under low pressure weakens the energy dissipation of the plasma jet and also reduces the disturbance to the plasma jet [7]. Consequently, from 980 mbar to 3 mbar, the plasma jet shows an increased length as well as a weakened air disturbance at the fringe. This observation is similar to the LPPS, indicating the strong effect of the pressure on the plasma jet shape [8]. It is worth noting that when the environmental pressure drops to 3 mbar, the plasma jet dramatically expands. Moreover, as seen in Fig. 3.2, the powder stream expands more severely than the plasma stream, which causes a separation of the powders and the plasma jet.

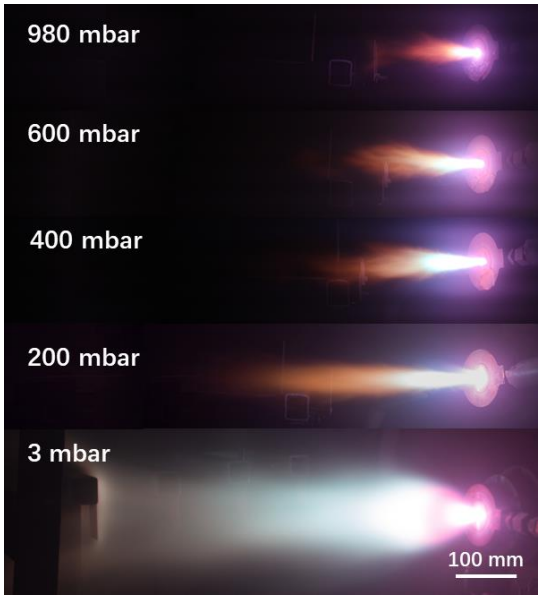

Fig. 3.1 Shapes of the plasma jets under different environmental pressures with the suspension injected

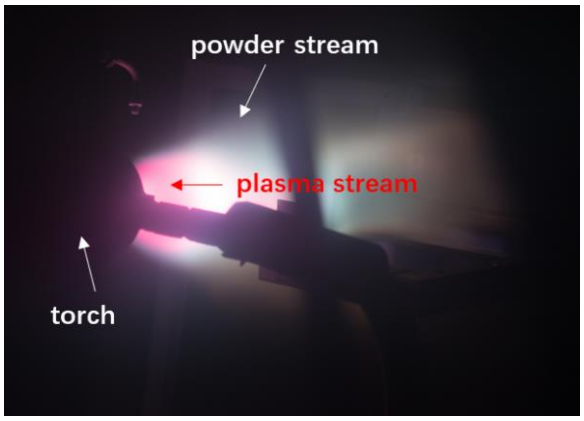

Fig. 3.2 Separation of the powders and the plasma jet under 3 mbar

3.4 Microstructures of the coatings

The coating prepared under 3 mbar exhibits poor adhesion force. Most of the coating fell off during the preparation process. Thus, the coating prepared under 3 mbar is separately analysed to distinguish it from the other coatings.

Fig. 3.3 shows the microstructure of the coating prepared under 3 mbar. As seen in the surface image, the coating mainly consists of nanoparticles, as well as a few spherical particles. In the cross-sectional image, a severe detachment occurs in the coating, and the coating exhibits a quite low thickness of ~ 10 μm. Nevertheless, there seems to be no visible pore in the intact region of the coating. By further observation, it can be seen that the pores in the coating are fully filled with nanoparticles (Fig. 3.3c). Under 3 mbar, a large number of powders are separated from the plasma jet (Fig. 3.2). This causes a large number of unmelted powders (nanoparticles) in the coating, therefore dramatically decreasing the adhesion of the coating. This result indicates that the pressure for LPSPS cannot be too low because of the differences in the expansion degree of the powder stream and the plasma stream under low pressure.

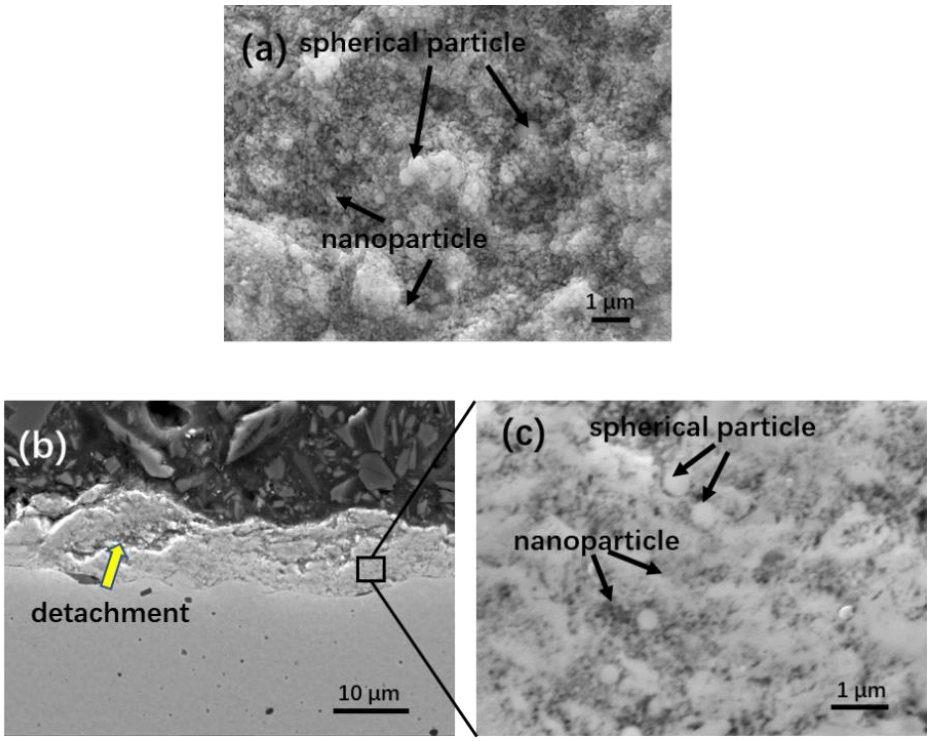

Fig. 3.3 Morphologies of SPS YSZ coating prepared under 3 mbar: (a) surface image, (b)(c) cross-sectional image

Fig. 3.4 shows the surface morphologies of the coatings under different pressures (except for 3 mbar). For the coating prepared under 980 mbar, the surface exhibits a cauliflower-shaped morphology, which has been reported in many SPS coatings [9-12]. As the pressure decreases, the cauliflower feature disappears. In turn, the coating under low pressures (from 600 mbar to 200 mbar) shows a flat surface, which is obviously different from that under 980 mbar. In the magnified morphologies, it can be observed that as the pressure decreases, the size of the particle in the coating significantly decreases. Under lower pressure, more and more nanoparticles (NPs) are formed in the coating, whereas the melted splats (MSs) and spherical particles (SPs) are gradually decreased.

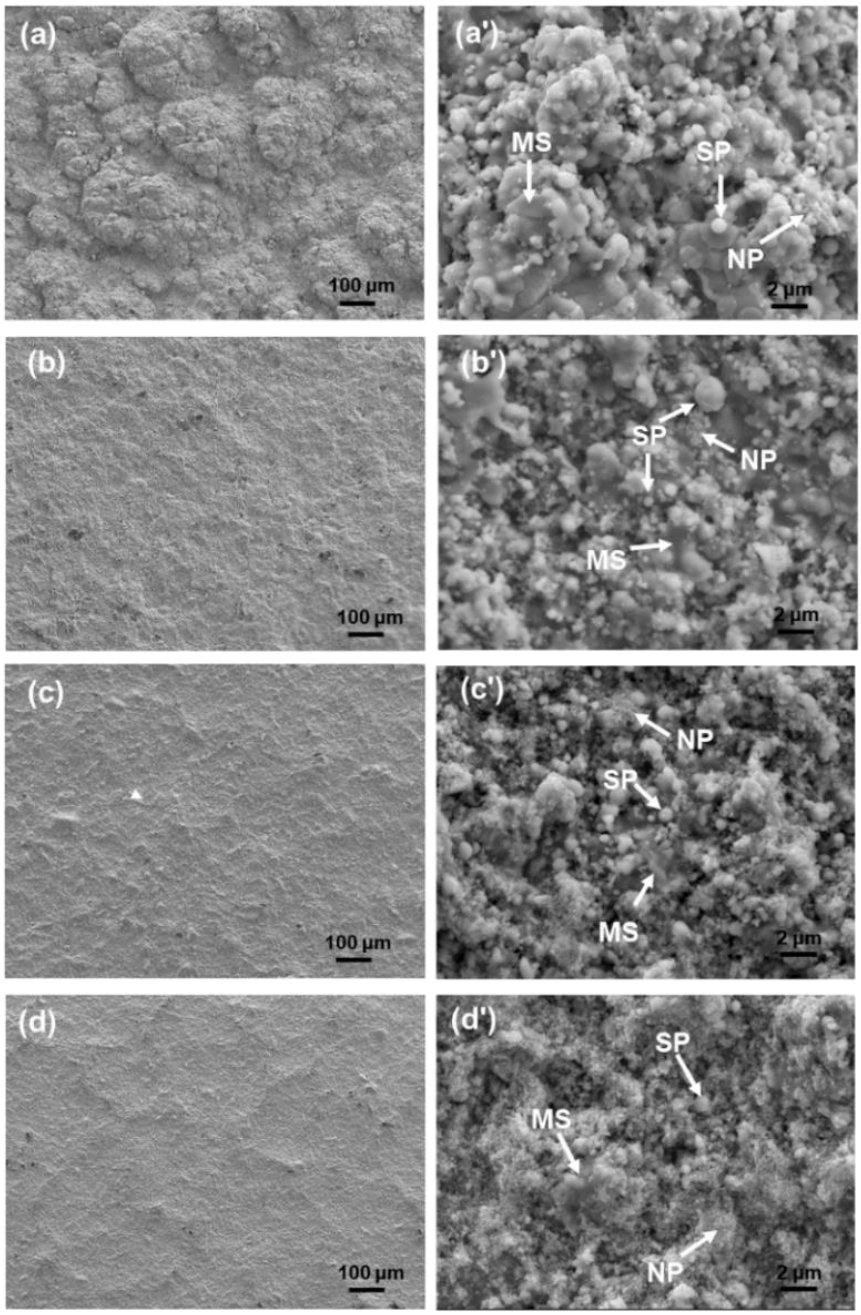

Fig. 3.4 Surface morphologies of SPS YSZ coatings under different environmental pressures: (a)(a') 980mbar, (b)(b') 600 mbar, (c)(c') 400 mbar, (d)(d') 200 mbar

Typically, the size of the particle in the coating is mainly dependent on the size of the atomised suspension droplet. The smaller the atomised droplet is, the smaller the particle of the coating is. The diameter of the droplet can be calculated using the following relation [13, 14]:

$$D_{min} = \frac{8\sigma_l}{C_D \rho U^2} \qquad (6)$$

σ_l, C_D, ρ, U is the surface tension, the drag coefficient, the plasma density and the plasma velocity relative to the droplet velocity, respectively. As the pressure decreases, the drag force of the plasma jet on the suspension is significantly increased due to the increased velocity of the plasma jet, which eventually causes a smaller droplet. It has been reported that the minimum droplet diameter is calculated to be about 1.8 μm under 100 pa by means of substituting suspension with ethanol [14]. This value is much smaller than 3 μm for the case under atmospheric pressure [15]. For that reason, from 980 mbar to 200 mbar, the size of the particle in the coating significantly decreases.

Once the solvent in the droplet vaporises, nanopowders tend to agglomerate together due to their high surface energy. Thereafter, the agglomerates are heated in the plasma jet and then impact the substrate to form the coating. For the molten agglomerates, they turn into SPs when impacting the substrate at low velocity or MSs when impacting at high velocity, as shown in Fig. 3.5. As for the nanoparticles in the coating, they are generally considered to be unmelted nanopowders.

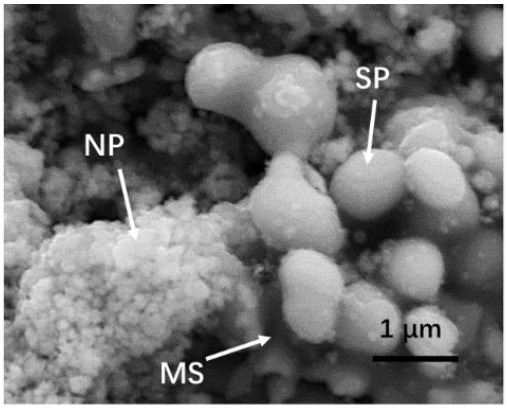

Fig. 3.5 Magnified surface morphology of SPS YSZ coating under 400 mbar

Nevertheless, in this study, most of these nanoparticles should be distinguished with the unmelted powder, since unmelted nanoparticles as the main composition of the coating are impossible because they are easily blown away by the high-velocity plasma jet under low pressure, or at the least, the resulting coating will have poor quality, like

the coating prepared under 3 mbar (Fig. 3.3). Although there are related reports regarding ceramic coating preparation based on unmelted sub-micron and nano-sized powders via vacuum cold spraying [16-18], the particle velocity in this study is obviously unable to reach the critical value of coating formation due to relatively high pressure and low working gas flow compared to vacuum cold spraying. The formation mechanism of the nanoparticles will be thoroughly discussed in the next chapter.

Fig. 3.6 shows the cross-section morphologies of the coatings under different pressures. All of the coatings show a high thickness, ranging from 400 μm to 600 μm. It is worth noting that decreased pressure should technically lead to a decrease in deposition efficiency of the coating. A typical example can be verified between APS coating and LPPS coating, where the deposition efficiency of APS coating is more than one order of magnitude higher than that of LPPS coating. However, in this study, the deposition efficiency does not substantially decline under low pressure, except for the case of 3 mbar. This indicates that, within a certain range (>200 mbar), decreasing the pressure cannot sacrifice the deposition efficiency of the coating.

In addition, the low pressure exhibits low gas resistance, the deposited particles, therefore, can reach the substrate with relatively high momentum in a long spraying distance [19, 20]. For that reason, although the spraying distance (100 mm) of the coating under 200 mbar is twice as long as (50 mm) the coating under 980 mbar, the thickness of the former is still similar to that of the latter. It should be noted that conventional SPS techniques generally possess a very short spraying distance (30 mm–50 mm) due to the low momentum of fine feedstock powders. It largely limits its application to the preparation of the coating on complex structural components such as turbine blades. The low-pressure environments in this study provide a feasible approach to solve this technical challenge.

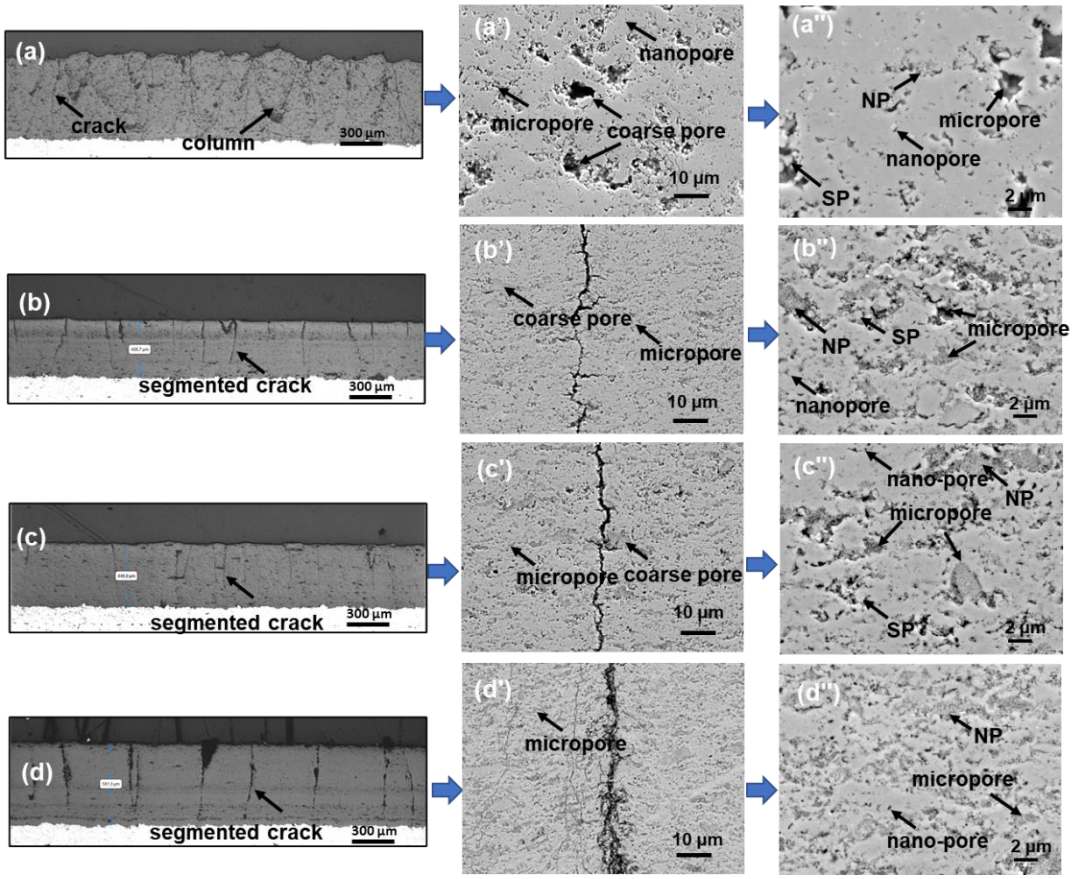

Fig. 3.6 Cross-section morphologies of SPS YSZ coatings under different environmental pressures: (a)(a')(a'') 980 mbar, (b)(b')(b'') 600 mbar, (c)(c')(c'') 400 mbar, (d)(d')(d'') 200 mbar

Although as the pressure varies, the deposition rate of the coatings remains similar, the cross-sectional morphology of the coating shows a significant difference. For the coating under 980 mbar, a column-like structure mixed with segmented cracks can be clearly observed in Fig. 3.6a. In that case, the interior of the column shows a porous microstructure (Fig. 3.6a'). The pores in the coating can be roughly classified into three categories: coarse pores (5–10 μm), micropores (1–5 μm) and nanopores (<1 μm). As the pressure decreases, the coating tends to transform from a column-like structure to a vertical crack-segmented structure. Moreover, the width of the vertical crack is increased as the pressure decreases, as shown in Fig. 3.7. In addition, as the pressure decrease, the number of the coarse pores in the coating is decreased, while the number

of micropores is increased.

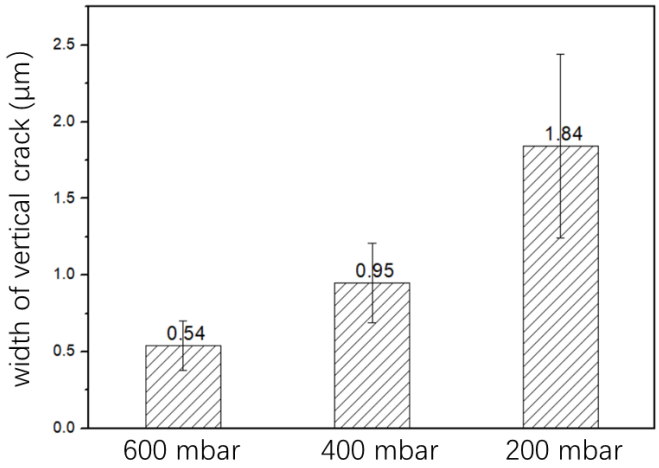

Fig. 3.7 Width of the vertical crack in SPS YSZ coatings as a function of the pressure

Interestingly, the regions between segmented cracks in the coatings under low pressure appear to possess an incredibly high density at low magnification (Fig. 3.6b–3.6d), which distinctly differs from the porous structure of the coating under 980 mbar. However, at higher magnification (Fig. 3.6b'–3.6d'), a number of micropores filled with nanoparticles can still be observed, making them invisible at low magnification. In fact, these nanoparticles exactly correspond to the NPs observed on the coating surface (Fig. 3.4). As the pressure decreases, more and more micropores are filled by the NPs. Particularly, in the coating prepared under 200 mbar, no obvious empty pores can be observed anymore.

3.5 Porosities of the coatings

Since the interior of the micropores is filled with the NPs, strictly speaking, they still belong to a unique porous microstructure to some extent. Fig. 3.8 displays the porosities of the coatings under different pressures. In that case, the filled pores were regarded as real pores to calculate the porosities. It can be seen that the porosity of the coating shows a nearly linear increase as the pressure decreases. In detail, the coating

under 200 mbar possesses a high porosity of 29.69%, which is more than twice that (12.74%) of the coating under 980 mbar.

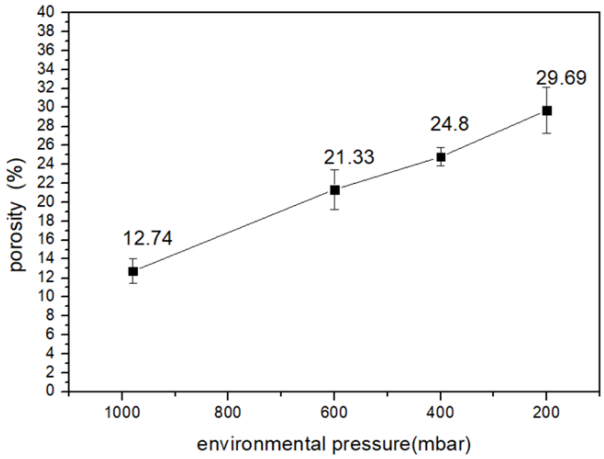

Fig. 3.8 Porosity of SPS YSZ coatings under different environmental pressures

It is commonly believed that the coating prepared under low pressure has a lower porosity than that prepared under atmospheric pressure; however, the result in this study is contrary to the above conclusion. As for suspension spraying, the deposited particle with a well-heated state and high momentum is beneficial to form a dense coating since the deposited particle, in that case, can be easily transformed into the MS on the substrate. From this point of view, it is reasonable that the coating under 980 mbar possesses the lowest porosity since it contains the largest number of MSs (Fig. 3.4a'). However, the large spherical particle in the coating under 980 mbar also enhances the shadow effect during the deposition process of the coating, resulting in more coarse pores in the coating. The momentum ($\boldsymbol{p}$) of the deposited particles is determined by particle velocity ($\boldsymbol{v}$) and particle mass (size) ($\boldsymbol{m}$) ($\boldsymbol{mv} = \boldsymbol{p}$). As mentioned before, low pressure increases the velocity of the particles, while it also reduces the size (mass) of the deposited particles. Hence, the density of the coating is actually dependent on which factor above is the dominant one. In this study, the decreased density of the coating should be attributed to the excessively low mass of the deposited particle.

According to the above results, the SPS coating prepared under low pressure

exhibits a vertical crack-segmented structure as well as a high porosity. Moreover, the pores are filled with nanoparticles. The porosity is an important property to evaluate TBCs. It reflects the thermal insulation of the coating. Commonly speaking, a coating with a high porosity possesses a low thermal conductivity. In addition, some researchers reported the favourable effects of the nanoparticles in the pores on the performance of TBCs. B. Bernard et al. [9] pointed out that the nanoparticles in the pores can enhance phonon scattering, which is expected to further reduce the thermal conductivity of the coating. R.S. Lima et al. [21] reported that the nanoparticles in the pore counteracted the increases in thermal diffusivity or elastic modulus caused by the sintering effects in high-temperature environments.

3.6 Surface roughness of the coatings

Fig. 3.9 displays the surface roughness (Ra) of the coatings prepared under different pressures. The surface roughness of the coating dramatically decreases from 12.12 μm to 2.43 μm as the pressure declines from 980 mbar to 200 mbar. TBCs not only work at elevated temperature environments but are also subjected to the attack of environmental particulates, including fly ash, sand, volcanic ash, etc. The main components of these particulates are CaO-MgO-Al_2O_3-SiO_2 (CMAS). At operating temperatures (>1200℃), the molten CMAS easily invades TBCs through the pores and cracks in the top coating, causing extra stress and reducing strain tolerance of the ceramic coating. When the mechanical properties decline, the spallation of the coating is accelerated [22]. Hence, the low surface roughness of TBCs will help to reduce the accumulation of corrosive media on the coating. In addition, it can also improve the aerodynamics of the blades.

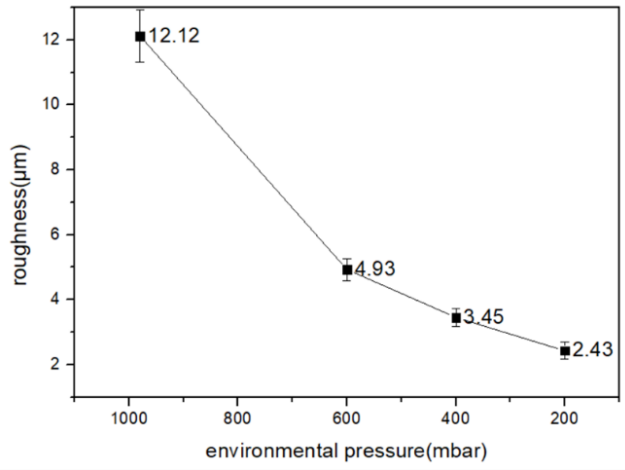

Fig. 3.9 Surface roughness of SPS YSZ coatings under different environmental pressures

3.7 Phase compositions of the powder and the coatings

Fig. 3.10 shows the XRD patterns of the powder and the coatings under different pressures. It can be seen that they contain the same main phase t'- ZrO_2, whereas the peak intensity of the coatings is much stronger than that of the original powder. This indicates that most powders are sufficiently heated in the plasma jet, thus increasing the crystallinity of the deposited particles. Nevertheless, the diffraction pattern of the coating prepared under 3 mbar exhibits a relatively lower intensity than the others prepared under low pressure. This is mainly due to unmelted powders separated from the plasma jet.

In addition, a certain amount of ZrO was detected in the coatings from 600 mbar to 200 mbar. Furthermore, the diffraction peak of ZrO was apparently intensified as the pressure increased. Since the coatings under low pressures were prepared in an argon atmosphere (oxygen-free atmosphere), ZrO_2 in the powder is quite easy to lose O and transform into ZrO at the ultra-high temperature of the plasma jet [23]. Additionally, the heat transfer between the plasma jet and the powder is more intense under higher pressure due to the higher plasma energy density. As a result, the transformation of ZrO_2

to ZrO is easily achieved under higher pressure. Therefore, the diffraction peak of ZrO in the coating under 600 mbar is the strongest one. As the coating under 980 mbar was prepared in an air atmosphere (oxygen-containing atmosphere), no ZrO was detected in the coating under 980 mbar. In fact, such a phenomenon of oxygen deficiency is sometimes also observed in the YSZ coating prepared by LPPS, which can be solved after proper heat treatment in an oxidative atmosphere.

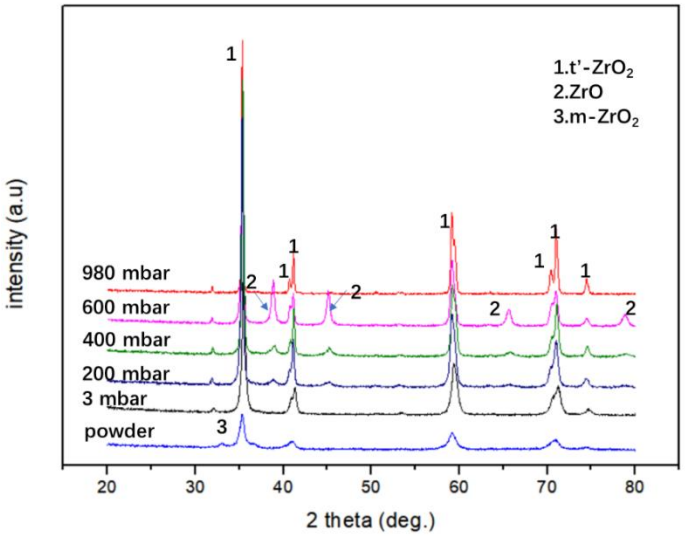

Fig. 3.10 XRD patterns of SPS YSZ coatings under different environmental pressures

3.8 Optimisation of pressure for LPSPS

In order to clearly distinguish the characteristic of LPSPS coating and SPS coating, the pressure of LPSPS needs to be as low as possible. However, excessively low pressure will cause the separation of the powder and the plasma jet, causing a large amount of unheated powder in the coating. After comprehensive consideration, the optimal pressure for LPSPS in this thesis is selected at 200 mbar.

3.9 Orientation of the cracks in the LPSPS coating and SPS coating

Fig. 3.11 shows the cross-sectional microstructures of the LPSPS coating (under

200 mbar) and the SPS coating (under 980 pressure) with the increased radial distance from the plasma centre to the fringe. For that, a special experiment was conducted, as shown in the schematic diagram in Fig. 3.11. The plasma torch was first adjusted to make its axial centreline perpendicular to the surface of the substrate; thereafter, it was moved back and forth in the same horizontal plane. Finally, the coated samples were sectioned along the plane, vertical to the moving direction of the plasma torch.

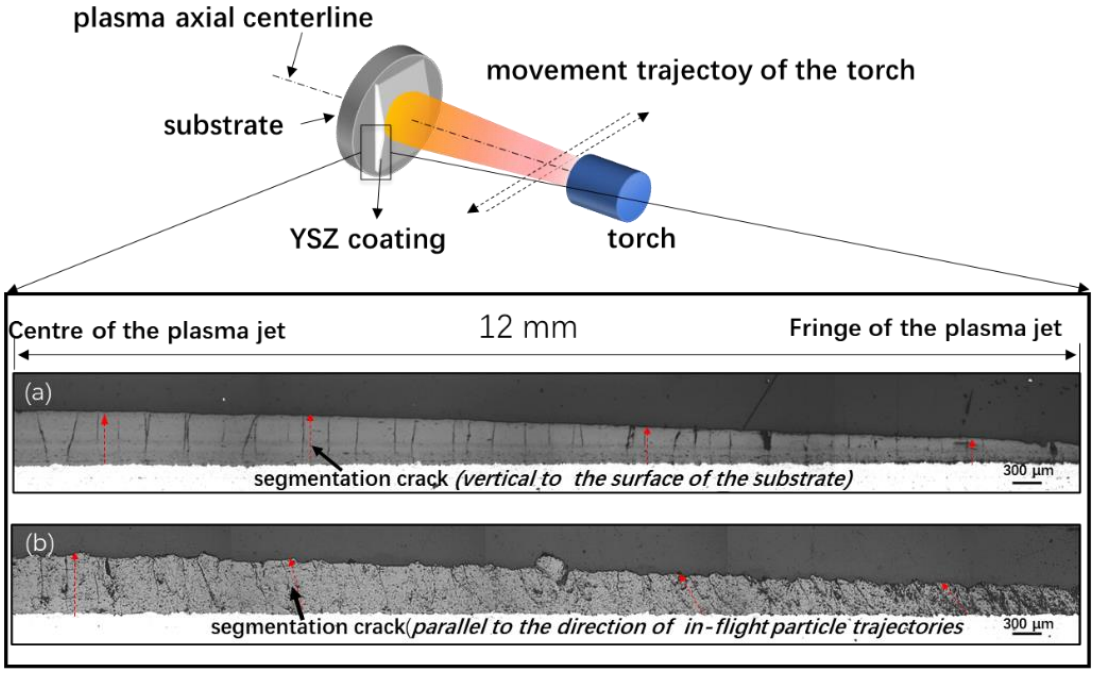

Fig. 3.11 Cross-sectional morphologies of the YSZ coatings along the radial direction of the plasma jet: (a) prepared by LPSPS, (b) prepared by SPS

As shown in Fig. 3.11, both coatings possess a reduced thickness as the radial distance of the plasma jet increases. The coating thickness at the fringe of the plasma jet is less than half the one at the centre of the plasma jet. It is interesting to note that the segmented cracks in the LPSPS coating are all vertical to the substrate surface, whereas those in the SPS coating mostly propagate along the in-flight trajectories of the deposited particles. Extensive references reported the existence of segmented cracks in the YSZ coatings prepared using APS and SPS. It is commonly believed that the formation of the segmented crack is related to the release of tensile stress of the coating

surface during the coating deposition process [24]. The factors affecting the formation of the segmented crack include deposition temperature, coating thickness, coating microstructure, droplet properties and so on. Guo et al. [25] reported that the density of the segmented crack increased as the substrate temperature or coating thickness increased. Ganvir et al. [26] pointed out that the coating deposited with higher droplet momentum tended to turn into a lamellar or vertical cracked structure. Vaßen et al. [27] considered that the segmented crack was more easily formed in the SPS coating than in the APS coating since the APS coating contained a higher amount of micro-crack, which can relax tensile stress during splat cooling. As a matter of fact, the vertical cracks are beneficial to TBCs because they can greatly tolerate the thermal strain to prevent the spallation of the coating.

For the LPSPS coating, the structure of the coating shows a non-preferred orientation. Therefore, the segmented cracks tend to propagate in a direction vertical to the tensile stress (coating surface). However, for the SPS coating in this study, the structure of the coating possesses the preferred orientation – the columnar structure. Thus, the cracks preferentially propagate along the gap between the columns.

3.10 Deposition mechanism of the LPSPS coating

The huge difference in the microstructure between the SPS coating and the LPSPS coating is attributed to the difference in their deposition mechanism. As the plasma jet reaches the substrate, the plasma jet shifts its movement direction from the direction perpendicular to the surface to the direction parallel to the surface. In order to characterise the behaviour of particles suspended in the plasma jet, a dimensionless number of Stokes number (S_t) is introduced as shown in Eqs. (1):

$$S_t = \frac{\rho_d d^2 v_0}{18 \mu_g l} \quad (1)$$

ρ_d is the particle density, d is the particle diameter, v_0 is the fluid velocity of the flow (plasma jet), l is the characteristic dimension of the obstacle (substrate) and μ_g

is the gas dynamic viscosity (plasma viscosity). The lower S_t is, the more likely the particles are to follow the plasma jet.

Fig. 3.12 shows the schematic of the SPS coating deposition and LPSPS coating deposition. Under atmospheric pressure, d and v_0 are relatively low, whereas μ_g is relatively high. Hence, with a relatively low S_t, the particles easily follow the plasma jet streamline, parallel to the substrate surface to deposit on the sides of surface asperities, resulting in a prominent growth of the coating on the asperities. After a few passes of the plasma jet, the columnar structure is built up [19]. However, under low pressure, the plasma jet exhibits much higher velocity v_0 and lower viscosity μ_g. In that case, S_t is much higher than that of atmospheric pressure. In other words, under low pressure, the particles easily detach from the plasma jet streamline, then vertically impact the substrate. In that case, after a few passes, the build-up of the coating is relatively uniform. As a result, no columnar structure is formed in the coating under low pressure, which also greatly decreases the roughness of the resulting coating.

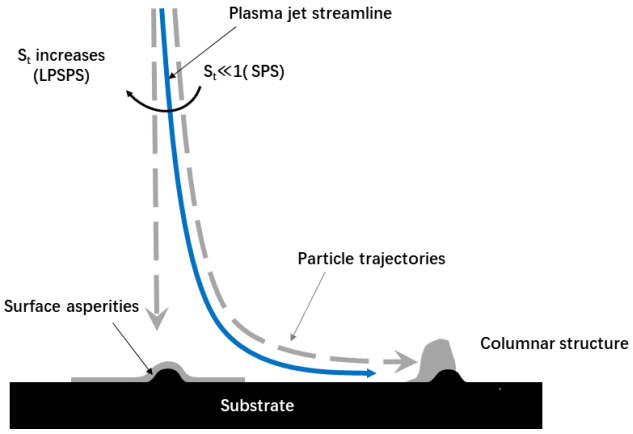

Fig. 3.12 Schematic of the SPS coating deposition and LPSPS coating deposition

3.11 Conclusion

In this chapter, the effect of environmental pressure on the microstructure of the coating prepared by suspension plasma spraying are investigated. The main conclusions are summarised as follows:

1. The required pressure for LPSPS cannot be too low; otherwise, the powders will be separated from the plasma jet, dramatically decreasing the adhesion of the coating. The optimised pressure for LPSPS is 200 mbar.
2. The size of the particle in the coating is significantly decreased as the pressure decreases. More nanoparticles are formed in the coating under lower pressure.
3. Within a certain range (> 200 mbar), decreasing the pressure can increase the effective spraying distance without sacrificing the deposition efficiency of the coating.
4. As the pressure decreases, the coating is transformed from a column-like structure to a vertical crack-segmented structure; a dramatic decrease is also seen in the surface roughness of the coating.
5. Compared to the coating prepared under atmospheric pressure, the coating prepared under low pressure contain fewer coarse pores (5 μm–10 μm) but exhibit a higher porosity due to the existence of the nanoparticles.
6. The segmented cracks in the LPSPS coating is consistently vertical to the surface of the substrate. However, the segmented cracks of the SPS coating are parallel to the direction of the in-flight particle trajectories.

References

[1] X. Fan, G. Darut, M.P. Planche, C. Song, H. Liao, G. Montavon, Preparation and characterization of aluminum-based coatings deposited by very low-pressure plasma spray, Surface and Coatings Technology 380 (2019).

[2] D.T.L. N. N Zhang, Y. L. Li, Y. Zhang, M. P. Planche, H. L. Liao, C. Coddet, F. Y. Dong, In-flight particle characterization and coating formation under low pressure plasma spray condition, Journal of Iron and Steel Research International 24 (2017) 306-312.

[3] J. Mao, M. Liu, Z. Deng, K. Wen, C. Deng, K. Yang, Z. Chen, Coating deposition regularity depended on orientation difference in PS-PVD plasma jet, Chinese Journal of Aeronautics (2020).

[4] M.G. J. L. Dorier, Ch. Hollenstein, Plasma Jet Properties in a New Spraying Process at Low Pressure for Large Area Thin Film Deposition, International Thermal Spray Conference (2001) 28-30.

[5] X.F. Zhang, K.S. Zhou, M. Liu, C.M. Deng, C.G. Deng, J. Mao, Z.Q. Deng, Mechanisms governing the thermal shock and tensile fracture of PS-PVD 7YSZ TBC, Ceramics International 44(4) (2018) 3973-3980.

[6] Z. Salhi, D. Klein, P. Gougeon, C. Coddet, Development of coating by thermal plasma spraying under very low-pressure condition <1mbar, Vacuum 77(2) (2005) 145-150.

[7] N. Zhang, F. Sun, L. Zhu, M.P. Planche, H. Liao, C. Dong, C. Coddet, Electron Temperature and Density of the Plasma Measured by Optical Emission Spectroscopy in VLPPS Conditions, Journal of Thermal Spray Technology 20(6) (2011) 1321-1327.

[8] K. von Niessen, M. Gindrat, Plasma Spray-PVD: A New Thermal Spray Process to Deposit Out of the Vapor Phase, Journal of Thermal Spray Technology 20(4) (2011) 736-743.

[9] B. Bernard, A. Quet, L. Bianchi, A. Joulia, A. Malié, V. Schick, B. Rémy, Thermal insulation properties of YSZ coatings: Suspension Plasma Spraying (SPS) versus

Electron Beam Physical Vapor Deposition (EB-PVD) and Atmospheric Plasma Spraying (APS), Surface and Coatings Technology 318 (2017) 122-128.

[10] W. Fan, Y. Bai, Review of suspension and solution precursor plasma sprayed thermal barrier coatings, Ceramics International 42(13) (2016) 14299-14312.

[11] A. Ganvir, S. Joshi, N. Markocsan, R. Vassen, Tailoring columnar microstructure of axial suspension plasma sprayed TBCs for superior thermal shock performance, Materials & Design 144 (2018) 192-208.

[12] M. Gupta, N. Markocsan, X.H. Li, L. Östergren, Influence of Bondcoat Spray Process on Lifetime of Suspension Plasma-Sprayed Thermal Barrier Coatings, Journal of Thermal Spray Technology 27(1-2) (2017) 84-97.

[13] P. Fauchais, V. Rat, C. Delbos, J.F. Coudert, T. Chartier, L. Bianchi, Understanding of suspension DC plasma spraying of finely structured coatings for SOFC, IEEE Transactions on Plasma Science 33(2) (2005) 920-930.

[14] P. He, H. Sun, Y. Gui, F. Lapostolle, H. Liao, C. Coddet, Microstructure and properties of nanostructured YSZ coating prepared by suspension plasma spraying at low pressure, Surface and Coatings Technology 261 (2015) 318-326.

[15] P. Fauchais, R. Etchart-Salas, V. Rat, J.F. Coudert, N. Caron, K. Wittmann-Ténèze, Parameters Controlling Liquid Plasma Spraying: Solutions, Sols, or Suspensions, Journal of Thermal Spray Technology 17(1) (2008) 31-59.

[16] L.S. Wang, C.X. Li, K. Ma, S.L. Zhang, G.J. Yang, C.J. Li, La0.8Sr0.2Ga0.8Mg0.2O3 electrolytes prepared by vacuum cold spray under heated gas for improved performance of SOFCs, Ceramics International 44(12) (2018) 13773-13781.

[17] S.Q. Fan, C.J. Li, C.X. Li, G.J. Liu, G.J. Yang, L.Z. Zhang, Preliminary Study of Performance of Dye-Sensitized Solar Cell of Nano-TiO2 Coating Deposited by Vacuum Cold Spraying, Materials Transactions 47(7) (2006) 1703-1709.

[18] S.Q. Fan, G.J. Yang, C.J. Li, G.J. Liu, C.X. Li, L.Z. Zhang, Characterization of Microstructure of Nano-TiO2 Coating Deposited by Vacuum Cold Spraying, Journal of Thermal Spray Technology 15(4) (2006) 513-517.

[19] K. VanEvery, M.J.M. Krane, R.W. Trice, H. Wang, W. Porter, M. Besser, D. Sordelet, J. Ilavsky, J. Almer, Column Formation in Suspension Plasma-Sprayed Coatings and Resultant Thermal Properties, Journal of Thermal Spray Technology 20(4) (2011) 817-828.

[20] A. Joulia, G. Bolelli, E. Gualtieri, L. Lusvarghi, S. Valeri, M. Vardelle, S. Rossignol, A. Vardelle, Comparing the deposition mechanisms in suspension plasma spray (SPS) and solution precursor plasma spray (SPPS) deposition of yttria-stabilised zirconia (YSZ), Journal of the European Ceramic Society 34(15) (2014) 3925-3940.

[21] R.S. Lima, B.R. Marple, Nanostructured YSZ thermal barrier coatings engineered to counteract sintering effects, Materials Science and Engineering: A 485(1-2) (2008) 182-193.

[22] L. Guo, Z. Yan, Y. Yu, J. Yang, M. Li, CMAS resistance characteristics of LaPO4/YSZ thermal barrier coatings at 1250°C–1350°C, Corrosion Science 154 (2019) 111-122.

[23] R.W. Rice, Comment on "Black Color in Partially Stabilized Zirconia", Journal of American Ceramic Society 74 (7) (1991) 1745-46.

[24] S.V. Shinde, E.J. Gildersleeve V, C.A. Johnson, S. Sampath, Segmentation crack formation dynamics during air plasma spraying of zirconia, Acta Materialia 183 (2020) 196-206.

[25] H.B. Guo, R. Vaßen, D. Stöver, Atmospheric plasma sprayed thick thermal barrier coatings with high segmentation crack density, Surface and Coatings Technology 186(3) (2004) 353-363.

[26] A. Ganvir, R.F. Calinas, N. Markocsan, N. Curry, S. Joshi, Experimental visualization of microstructure evolution during suspension plasma spraying of thermal barrier coatings, Journal of the European Ceramic Society 39(2-3) (2019) 470-481.

[27] R. Vaßen, H. Kaßner, G. Mauer, D. Stöver, Suspension Plasma Spraying: Process Characteristics and Applications, Journal of Thermal Spray Technology 19(1-2) (2009) 219-225.

Chapter 4 Tailoring of the microstructure of the coating prepared by low-pressure suspension plasma spraying

Chapter 4: Tailoring of the microstructure of the coating prepared by low-pressure suspension plasma spraying

In this chapter, LPSPS is conducted under 200 mbar. The microstructure of LPSPS YSZ coatings is tailored by varying the main spraying conditions. These spraying conditions include environmental atmosphere (argon versus air), oxygen content in the environment, spray distance, suspension solid content, solvent type.

4.1 Introduction

SPS, as a versatile process, provides flexible tailoring for the coating microstructure to meet the requirements of different applications, like photocatalytic coating, TBCs and wear-resistant coating. However, the current LPSPS coating seems to only show an improved density and uniformity compared to SPS coating. Hence, tailoring of the coating microstructure is necessary to fully understand the structural characteristics of the LPSPS coating.

For spraying technologies, the most common method to tailor the coating structure is varying the spraying conditions. In terms of LPSPS, the spraying process is conducted in a closed spraying environment. Hence, it has some unique spraying conditions that are invariable in SPS, including environmental pressure, environmental atmosphere, and oxygen content in the environment. These spraying conditions should be first examined. Since the environmental pressure has been studied in chapter 3, this chapter will first focus on the other two conditions to tailor the coating microstructure. In addition, both LPSPS and SPS have some common spraying conditions, such as spraying distance, solid content, solvent type and so on, which have been widely studied in SPS [1-4]. These spraying conditions should also have a certain influence on LPPS coating in the same or different way, and they will be studied in this chapter as well.

4.2 Effect of the environmental atmosphere on the microstructure of the coating

4.2.1 Preparation conditions of the coatings

Table 4.1 displays the detailed experimental parameters of the coating prepared in two atmospheres (argon versus air). Both atmospheres were achieved by means of the following operations: for the argon atmosphere, the pressure in the tank was first pumped down to 1 mbar to remove as much oxygen as possible. Argon was subsequently filled into the tank until the pressure reached 200 mbar. For the air atmosphere, the pressure in the tank was directly pumped to 200 mbar, remaining 200 mbar air in the tank. The pressure in the tank was automatically adjusted by the gas valve during the spraying process.

Table 4.1 Experimental parameters of LPSPS YSZ coatings prepared in two atmospheres

Spraying parameters	argon atmosphere	air atmosphere
Environmental pressure (mbar)	200	200
Current (A)	680 × 2	680 × 2
Voltage (V)	54	54
Ar (L/min)	80	80
H_2(L/min)	22	22
Solvent type	ethanol	ethanol
Solid content (wt%)	15	15
Suspension flow (mL/min)	35	35
Spraying distance (mm)	100	100
Spraying time (min)	14	9.5

4.2.2 Microstructures of the coatings

Fig. 4.1 displays the surface features of the coatings prepared in two atmospheres. The coating prepared in the argon appears in black colour, whereas the coating prepared in the air appears in white colour. The surface roughness (Ra) of the coating prepared in the argon is only 2.38 ± 0.32 μm. However, when the preparation environment turns into the air, the roughness of the coating is dramatically increased to 8.38 ± 0.53 μm.

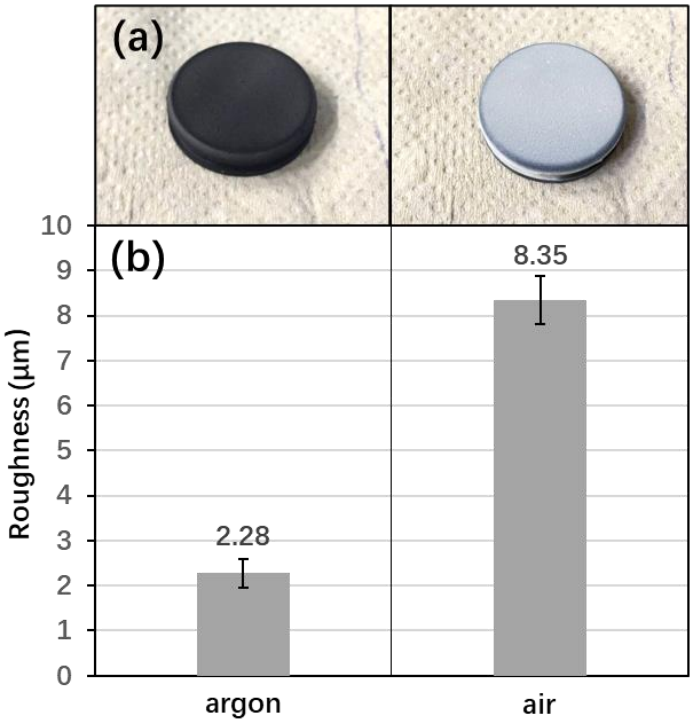

Fig. 4.1 Surface features of LPSPS YSZ coatings prepared in two atmospheres: (a) coating appearance, (b) surface roughness of the coating

Fig. 4.2 shows the microstructures of the coating prepared in the argon. It can be observed that the coating exhibits a similar surface or cross-section morphology with the previous LPSPS coating in chapter 3 (Fig. 3.4d and Fig. 3.4d'), although the solid content is lower in this case (15 wt% versus 25 wt%). The coating still exhibits a rather flat surface morphology and contains a large number of nanoparticles, a few spherical particles and melted splats. These nanoparticles have a similar size to the feed powder and are well adhered to the substrate, as shown in Fig. 4.3. It needs to be pointed out

that the coatings fell off as a whole after being in place for several weeks, as shown in Fig. 4.2b and Fig. 4.4. This phenomenon reflects the poor adhesion of the LPSPS coating prepared in the argon.

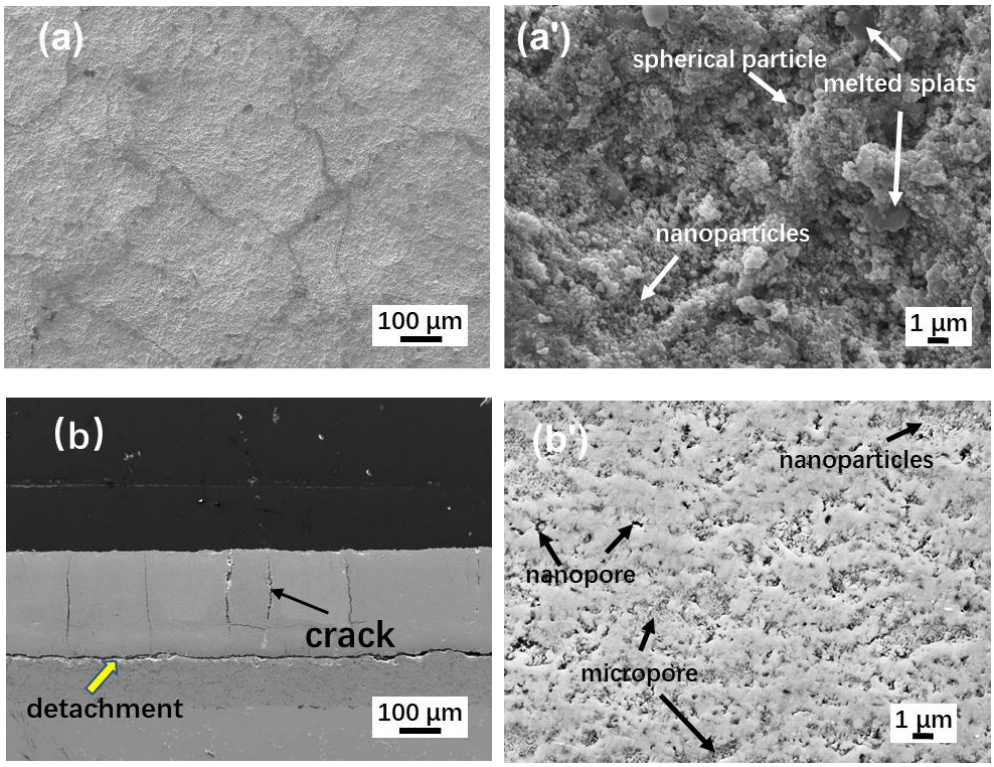

Fig. 4.2 SEM images of LPSPS YSZ coating prepared in the argon: (a)(a') surface morphologies, (b)(b') cross-sectional morphologies

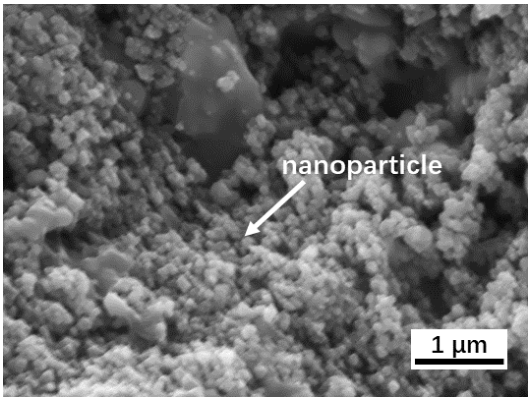

Fig. 4.3 Surface morphology of LPSPS YSZ coating prepared in the argon with a high magnification

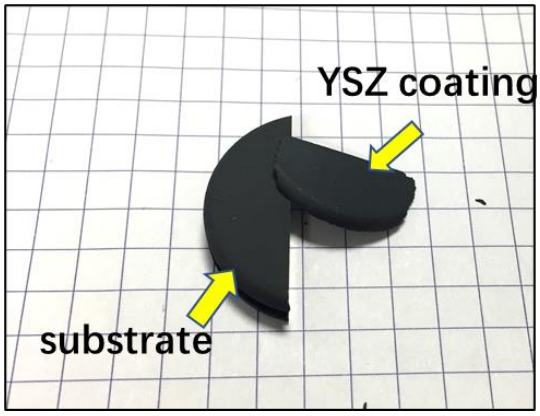

Fig. 4.4 Spallation of the LPSPS YSZ coating prepared in the argon after being in place for several weeks

Fig. 4.5 shows the microstructure of the coating prepared in the air. Different from that prepared in the argon, in this case, the coating exhibits a rough surface morphology, where many convexes can be observed on the surface of the coating (Fig. 4.5a). Moreover, the nanoparticles in the coatings are significantly removed (Fig. 4.5a'). In turn, a large number of spherical particles and melted splats are formed. In the cross-sectional image of the coating (Fig. 4.5b), there are almost no noticeable vertical cracks in the coating, and no crack or gap is formed at the interface between the coating and the substrate as well. In the magnified cross-sectional image (Fig. 4.5b'), the coating still contains a large number of micropores and nanopores. However, in this case, many micropores are empty without a nanoparticle filling. This observation is in good agreement with the surface morphology of the coating (Fig. 4.5a'), where fewer nanoparticles exist in the coating. In addition, the coating, in this case, has a lower porosity (14.46 ± 1.74%) than that (20.75 ± 2.23%) of the coating prepared in the argon, as shown in Fig. 4.6. This should be mainly attributed to the more melted splat on the coating prepared in the air.

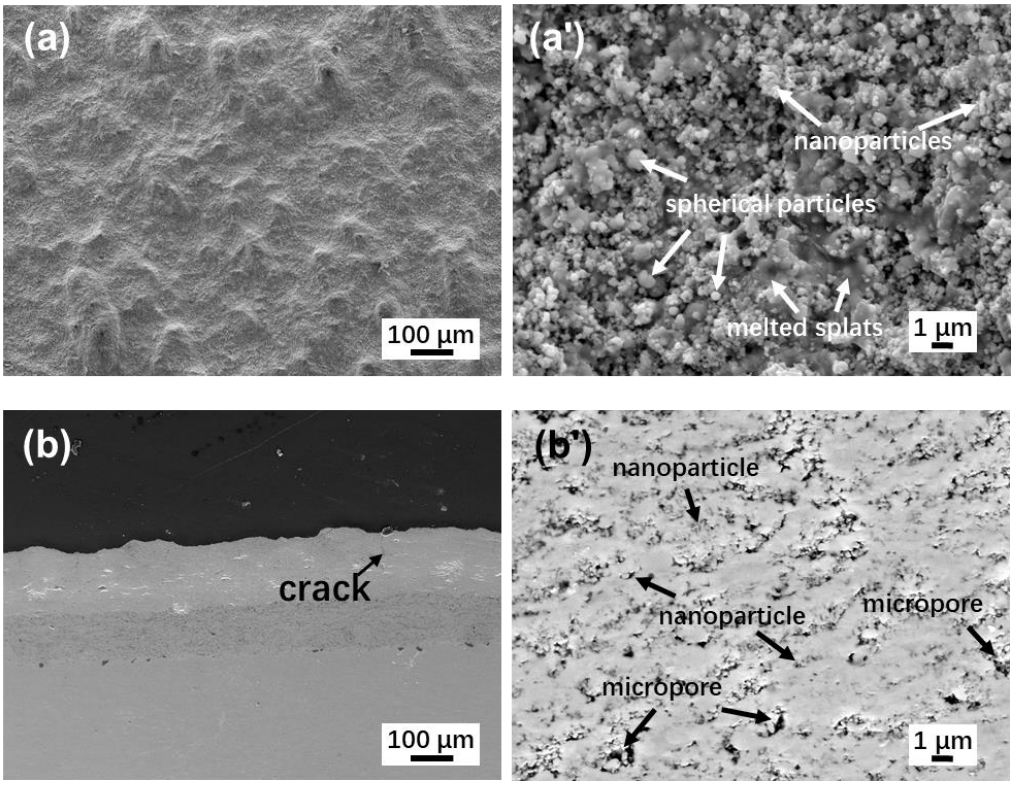

Fig. 4.5 SEM images of LPSPS YSZ coating prepared in the air: (a)(a') surface morphologies, (b)(b') cross-sectional morphologies

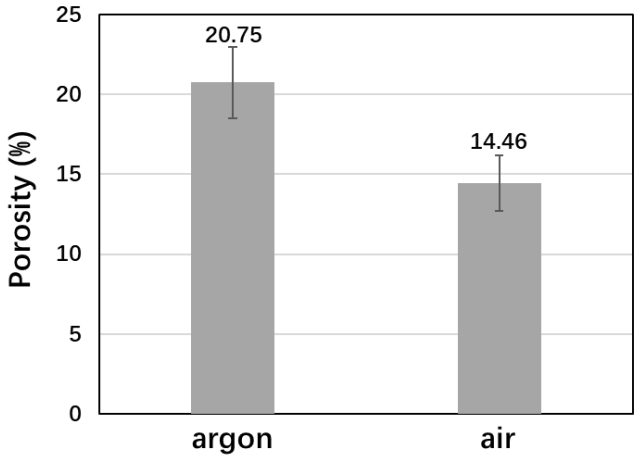

Fig. 4.6 Porosity of LPSPS YSZ coating prepared in two atmospheres

Normally, the vertical crack is caused by quenching stresses during the deposition of the coating. For the coating prepared in the argon, the nanoparticles are tightly packed, and most of the pores in the coating are filled with these nanoparticles. In that

case, it is hard for quenching stress to be released in the form of splat sliding or lissomness of the coating. As a result, a number of vertical cracks are formed in the coating. In contrast, for the coating prepared in the air, there are a number of empty micropores existing in the coating. These micropores provide a favourable medium for the release of quenching stress. Consequently, no obvious vertical cracks are formed in that case. In addition, the lower coating thickness may also suppress the formation of the vertical crack to some degree [5].

4.2.3 Phase composition of the coatings

Fig. 4.7 shows the phase composition of the feed powder and the coatings. Both coatings possess the same phase composition as the feed powder. They all mainly consist of t'-ZrO_2, and there is no significant difference in the diffraction patterns in both coatings. According to the intensity of the diffraction peaks, it can be seen that both coatings show a much high crystallinity than the powder, indicating that the powders are adequately heated by the plasma jet during the spraying process. It should be noted that different from the coating in chapter 3, no ZrO is detected in the coating prepared in the argon. It should be attributed to the much lower thickness in this case, which may affect the accuracy of XRD detection.

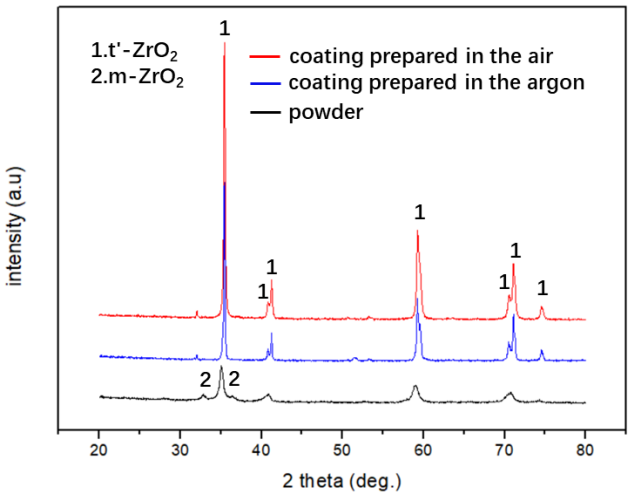

Fig. 4.7 XRD patterns of the feed powder and LPSPS YSZ coatings prepared in two atmospheres

4.2.4 Mechanical properties of the coatings

The mechanical properties of the coatings prepared in two atmospheres are shown in Fig. 4.8. Both coatings displayed a smooth load-displacement curve of indentation. The hardness and elastic modulus of the coatings prepared in the argon and in the air are 10.44 ±1.36 GPa / 146.34 ± 10.23 GPa, 9.35 ± 1.12 GPa / 142.56 ± 13.34 GPa, respectively. This indicates a small difference in the mechanical properties of the coatings prepared in the two atmospheres. Nevertheless, the hardness and elastic modulus of the former appears to be a little higher than that of the latter. The hardness and the elastic modulus of the coating strongly depend on the coating porosity. Generally speaking, the lower the porosity, the higher the hardness or elastic modulus. However, this conclusion seems to be inconsistent with the results of these two coatings. In this study, the porosity of the coating prepare in the air is actually lower than that of the coating prepared in the argon, but the former has lower hardness and elastic modulus than the latter. As mentioned above, the micropores in the coating prepared in the argon are fully filled by the nanoparticles, while those in the coating prepared in the air are mostly empty. It is believed that in comparison with the empty pores, the filled pores can somehow increase the hardness and the elastic modulus of the coating.

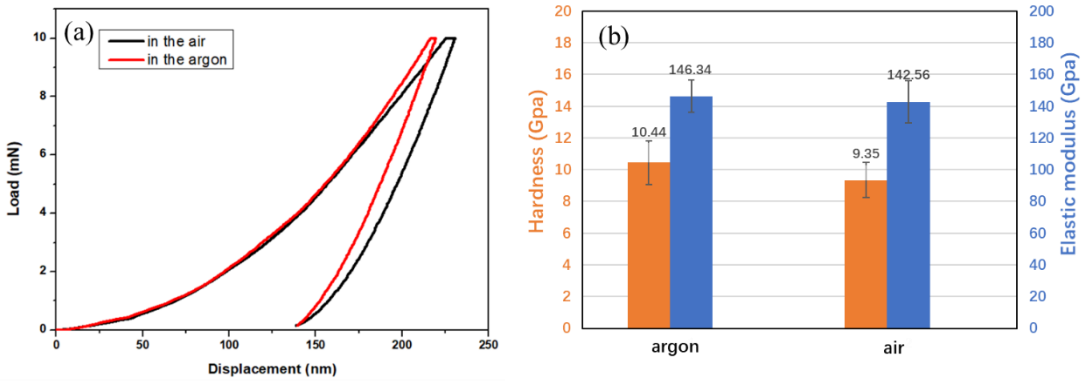

Fig. 4.8 Mechanical properties of LPSPS YSZ coatings prepared in two atmospheres: (a) load-displacement curves of nanoindentation, (b) hardness and elastic modulus

4.2.5 Characteristics of the plasma jets

The plasma jets in the two atmospheres are diagnosed by Optical Emission by

Spectroscopy (OES), as shown in Fig. 4.9. To simplify the analysis process, 35 ml/min of ethanol in place of the same flow of suspension were injected into the plasma jet.

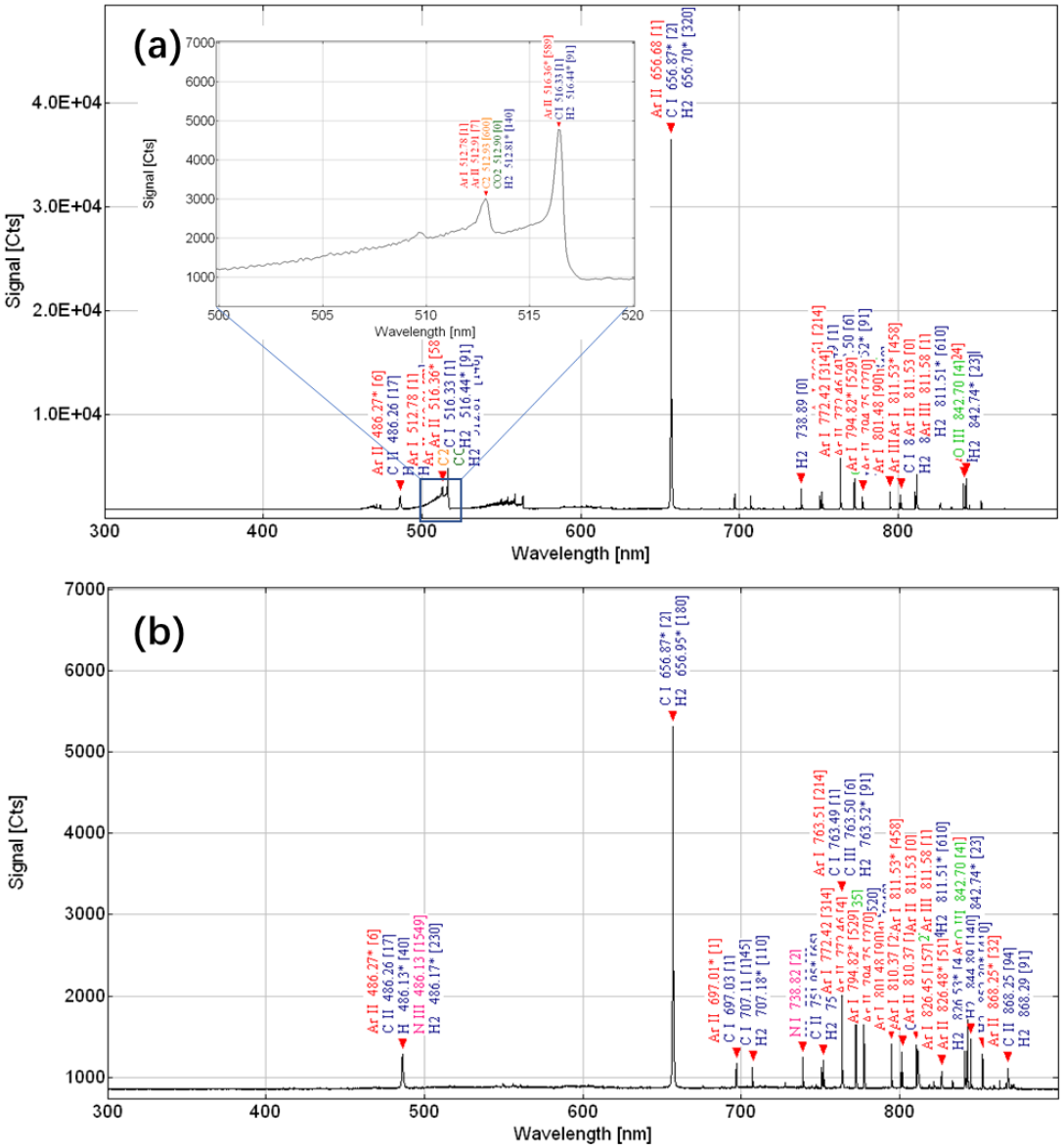

Fig. 4.9 OES patterns of the plasma jets with 35 mL/min of ethanol in two atmospheres: (a) in the argon, (b) in the air

It can be seen that in the argon atmosphere, a strong spectral signal of gaseous carbon molecules C_2 is detected in the plasma jet. However, in the air atmosphere, no obvious signal of C_2 is detected. This result indicates that the chemical composition in the plasma jet changes as the environmental atmosphere varies. When ethanol is injected into the plasma jet, some complex chemical reactions may take place as shown

below:

$$C_2H_5OH(l) \rightarrow CO(g) + C(g) + 3H_2\ (g) \qquad \Delta H^{\theta}_{298k} = 124.6\,kJ/mol\ (1)$$

$$C_2H_5OH(l) \rightarrow CO(g) + CH_4(g) + H_2\ (g) \qquad \Delta H^{\theta}_{298k} = 49.8\,kJ/mol\ (2)$$

$$C_2H_5OH(l) + 1/2O_2(g) \rightarrow 2CO(g) + 3H_2\ (g) \qquad \Delta H^{\theta}_{298k} = 14.1\,kJ/mol\ (3)$$

$$C_2H_5OH(l) + 3/2O_2(g) \rightarrow 2CO_2(g) + 3H_2\ (g) \qquad \Delta H^{\theta}_{298k} = -555.0\,kJ/mol\ (4)$$

$$C_2H_5OH(l) + 3\ O_2(g) \rightarrow 2CO_2(g) + 3H_2O(g) \qquad \Delta H^{\theta}_{298k} = -1366.8kJ/mol(5)$$

As seen in Eq. (1), ethanol will undergo a pyrolysis reaction in an oxygen-free environment. At the same time, a number of carbons (carbon black) may be generated as a by-product of the reaction. This can explain why a significant spectral signal of gaseous carbon molecules $\boldsymbol{C_2}$ is detected from the plasma jet in the argon (oxygen-free) atmosphere. Due to the existence of carbon, the resulting coating appears in black colour (another possible reason is the oxygen deficiency in ZrO_2, which has been commonly reported in the YSZ coatings prepared by LPPS [6, 7]). As the oxygen content in the environment rises, the produced carbon is gradually decreased. When the oxygen content is sufficient, a complete combustion reaction can take place, as shown in Eq. (5)

4.2.6 Hypothesis of the ethanol-based suspension evolution in two atmospheres

As mentioned before, there is a big difference in the morphology of the coatings prepared in different atmospheres. A huge number of nanoparticles are formed in the coating prepared in the argon, while only a few nanoparticles are formed in the coating prepared in the air. Even so, both coatings show similar mechanical properties and XRD patterns. These results indicate that most of the nanoparticles should be sufficiently

heated. Most of them should be distinguished from the unmelted particle. In order to explain the structural difference between the two coatings, a hypothesis of the ethanol-based suspension evolution in the two atmospheres are proposed, as shown in Fig. 4.10.

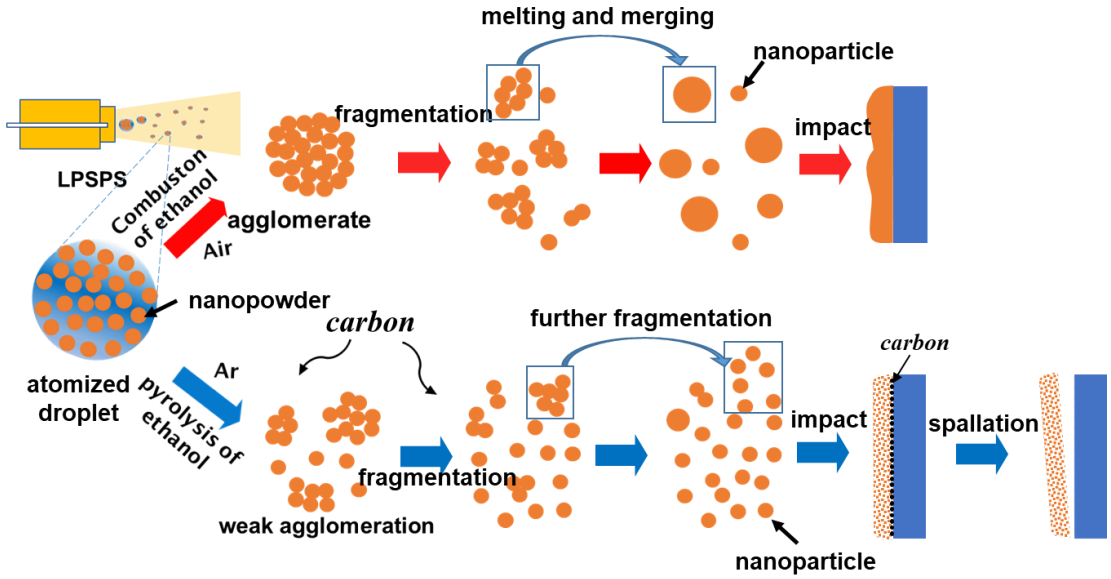

Fig. 4.10 Evolution of ethanol-based suspension in LPSPS in two atmospheres

When the suspension is injected into the plasma jet, it will successively undergo four major evolution stages: suspension atomisation, particle agglomeration, particle fragmentation or sintering and impact of final deposit. In the air atmosphere, once the atomised droplet vaporises, the exposed nanopowders tend to form agglomerates due to the high surface energy of the nanopowders [8]. The factors affecting nanopowder agglomeration mainly include [9]: 1. Van der Waals forces. 2. Moisture (hydrogen bonds). 3. Capillary forces. 4. Adsorbed foreign species. 5. Particle pre-sintering (during particle syntheses). Due to the high-velocity plasma jet under low pressure, these agglomerates can be further fragmented into smaller particles. However, in most cases, the merging of the agglomerates can suppress their further fragmentation and form molten particles at last. The molten particles have high momentum; thus, the resulting coating has a relatively high density and adhesion.

However, in the argon atmosphere, on the one hand, the functional groups (such

as O-H) on the surface of the powder are largely eliminated, which can weaken the agglomeration of the powders to some degree. In fact, such a characteristic of the argon atmosphere has been widely used to prepare the nanopowder; on the other hand, due to the pyrolysis of ethanol, carbon is produced in the plasma jet. Carbon can avoid direct contact between the particles, which can further inhibit the agglomeration of the powders [10, 11]. As a result, the final deposits in the argon atmosphere are mostly nanoparticles that have the same size as the powder. These nanoparticles have low momentum, so the resulting coating has a relatively low density and adhesion. Besides, the carbon may adhere to the substrate surface, which causes the spallation of the coating at last.

It should be pointed out that the real evolution process of suspension is much more complicated than what is shown in the schematic diagram. For instance, the agglomeration and fragmentation of the particles can take place simultaneously or alternately; additionally, since the particles in the plasma centre and plasma fringe are heated to different degrees, both evolution modes displayed in the schematic diagram can exist simultaneously as well.

4.3 Effect of the oxygen content on the microstructure of the coating

4.3.1 Injection of oxygen into the plasma jet

According to Eq. (1)-(5) in section 4.2, it is known that as the oxygen content increases, the combustion of ethanol goes more adequately, accompanied by the transformation from an endothermic reaction to an exothermic reaction. According to this conclusion, more heat will be released into the plasma jet as the oxygen content in the environment rises. After converting the reaction heat of reaction (1) and reaction (5) to the power of the torch, it is found that in comparison to reaction (1), reaction (5) is equivalent to increasing the power of the torch by ~10 kW. According to this calculation,

it should be possible to tailor the coating structure by varying the oxygen content in the environment during the spraying process. In order to vary the oxygen content in the LPSPS, a homemade gas injector is assembled in front of the torch to inject oxygen in the plasma jet, as seen in Fig. 4.11. The oxygen flow is controlled at 15 L/min in order to minimise the turbulence of the oxygen to the plasma jet.

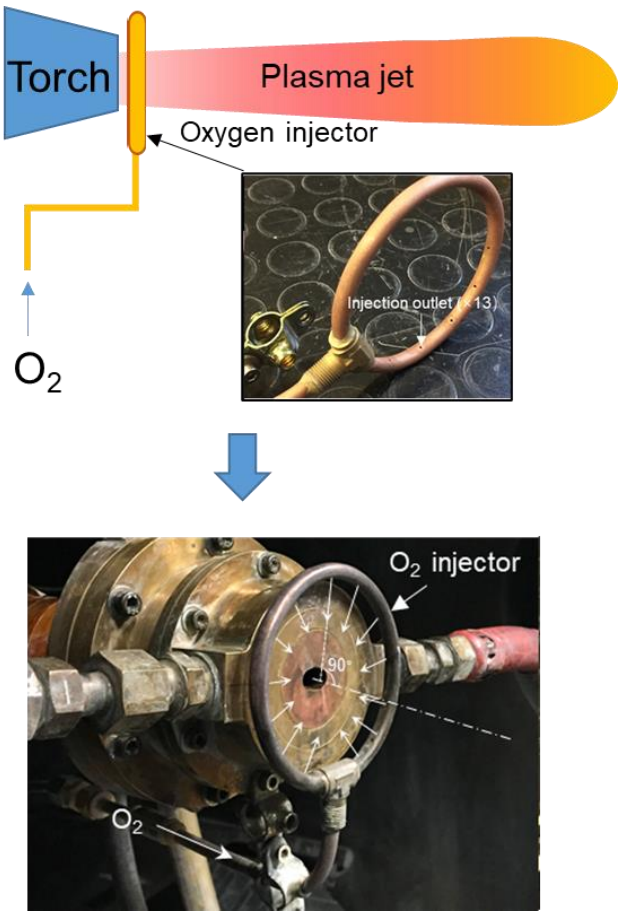

Fig. 4.11 The form of oxygen injection into the plasm jet

According to Eq. (5), for 15L/min of O_2, the ethanol flow for complete combustion is calculated at 13.03 mL/min (in the stoichiometric condition), which will release the most heat into the plasma jet. However, limited by experimental conditions, an excessively low flow will cause an unstable injection of ethanol. At the same time, the low-flow suspension also easily blocks the suspension injector nozzle. Considering that there is still a certain amount of oxygen remaining in the tank (200 mbar air), the

suspension flow is controlled at 20 mL/min. In that case, the ethanol is roughly considered to be completely combusted.

4.3.2 Preparation conditions of the coatings

In order to study the effect of the oxygen content on the coating microstructure, two experiments are designed. One is an experiment without oxygen injected, and the other is an experiment with oxygen injected. The detailed experimental parameters are shown in Table 4.2.

Table 4.2 Experimental parameters of the LPSPS YSZ coating prepared with and without oxygen injected

Spraying parameters	O-LPSP YSZ coating	LPSPS YSZ coating
Environmental atmosphere	air	air
Environmental pressure (mbar)	200	200
Current (A)	680 × 2	680 × 2
Voltage (V)	54	54
Ar (L/min)	80	80
H_2 (L/min)	22	22
Solvent type	ethanol	ethanol
Solid content (wt%)	15	15
Suspension flow (mL/min)	20	35
Additional O_2 (L/min)	15	-
Spraying distance (mm)	100	100
Spraying time (min)	9.5	9.5

4.3.3 Microstructures of the coatings

Fig. 4.12 shows the microstructure of O-LPSPS YSZ coating (with oxygen injected) and LPSPS YSZ coating (without oxygen injected). It can be observed that the

surface of O-LPSPS-coating exhibits a sintering-like morphology, where the particles are tightly packed. There are almost no pores observed either from the surface or from the cross-sectional image (Fig. 4.12a and Fig. 4.12a'). Even in the cross-sectional image with high magnification (Fig. 4.12a''), the coating still exhibits a high density, where only nanopores are observed. In contrast, for LPSPS YSZ coating, a certain number of nanoparticles are still observed on the coating surface, and the coating density is much lower than that of O-LPSPS YSZ coating. It is interesting that the nanoparticles are almost removed in O-LPSPS coating. According to Fig. 4.10, the plasma jet with higher enthalpy allows the agglomerate to be melted more easily, which suppress their further fragmentation. Fig. 4.13 shows the porosity of both coatings. O-LPSPS YSZ coating shows a rather low porosity of 3.04 ± 0.36%, while LPSPS YSZ coating shows a relatively high porosity of 14.46 ± 1.74%. Such a structure of O-LPSPS YSZ coating is expected in wear-resistant coatings, SOFC electrolytes, etc.

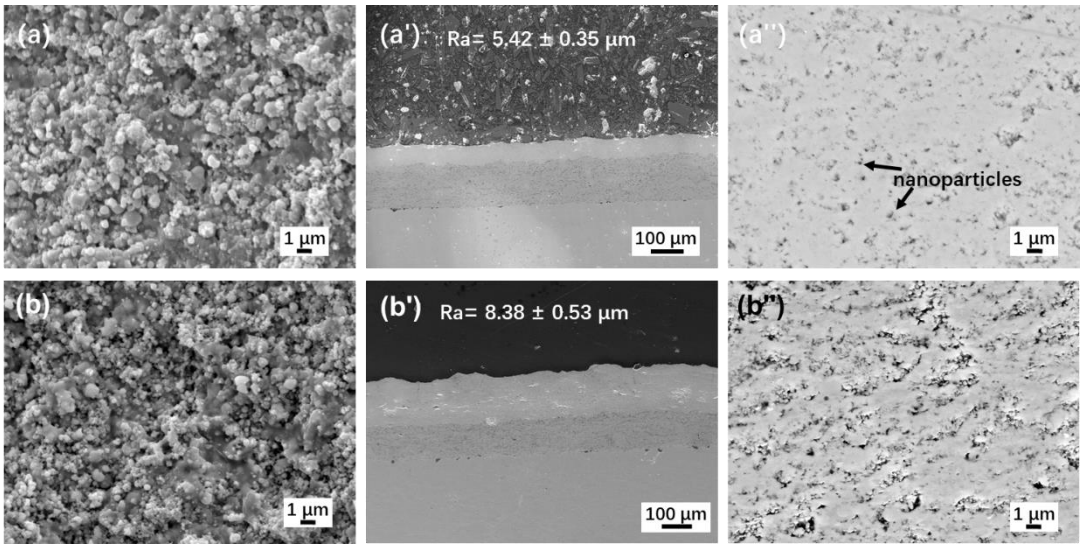

Fig. 4.12 SEM images of O-LPSPS YSZ coating and LPSPS YSZ coating: (a)(a')(a'') O-LPSPS YSZ coating, (b)(b')(b'') LPSPS YSZ coating

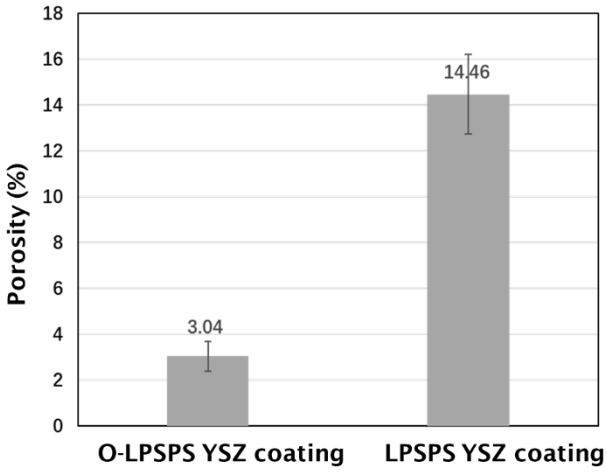

Fig. 4.13 Porosity of O-LPSPS YSZ coating and LPSPS YSZ coating

4.3.4 Phase composition of the coatings

Fig. 4.14 shows the phase compositions of O-LPSPS YSZ coating and LPSPS YSZ coating. It can be seen that there is no significant difference in the XRD patterns of both coatings. However, the intensity of diffraction peaks of O-LPSPS YSZ coating appears to be slightly stronger than that of LPSPS YSZ coating. It reflects that the crystallinity of the coating is increased when prepared with oxygen injected.

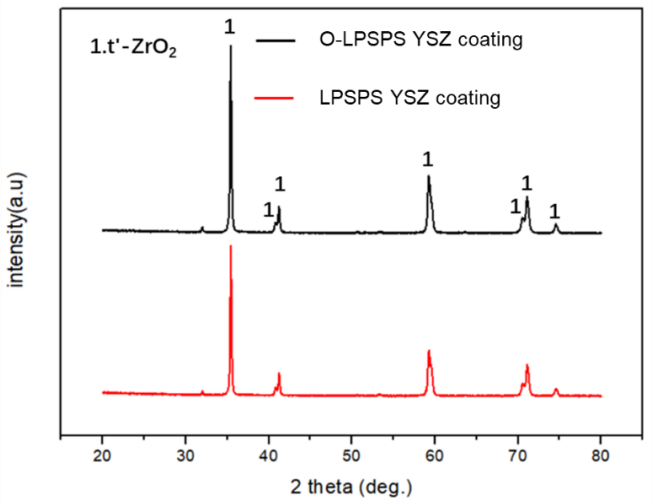

Fig. 4.14 XRD patterns of O-LPSPS YSZ coating and LPSPS YSZ coating

4.3.5 Mechanical properties of the coatings

Fig. 4.15 shows the mechanical properties of O-LPSPS YSZ coating and LPSPS YSZ coating. The load-displacement curve of O-LPSPS YSZ coating is steeper than that of LPSPS YSZ coating. The hardness and the elastic modulus of the former are 10.22 ± 1.03 GPa and 160.38 ± 8.93 GPa, respectively. Both values are higher than those (9.35 ± 1.12 GPa and 142.56 ± 13.34 GPa) of the latter. Both results reflect the improved mechanical properties of the coating prepared with oxygen injected.

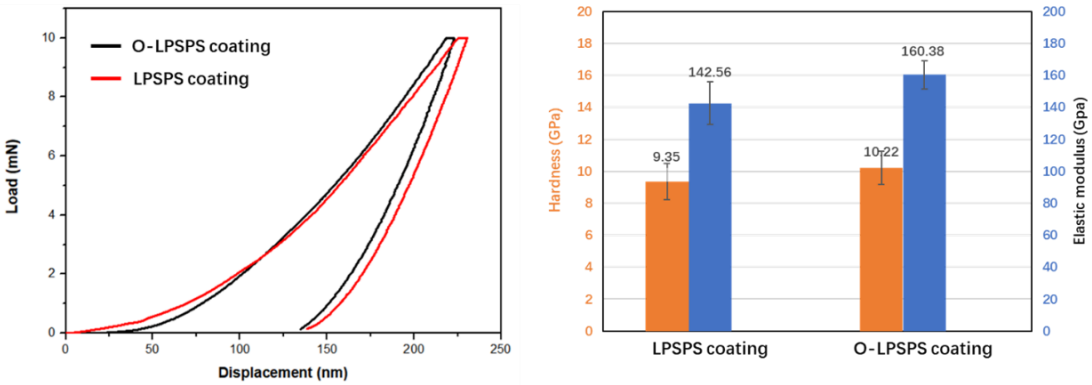

Fig. 4.15 Mechanical properties of O-LPSPS YSZ coating and LPSPS YSZ coating: (a) load-displacement of nanoindentation, (b) hardness and elastic modulus

4.3.6 Characteristics of the plasma jets

Fig. 4.16 shows the comparison of the OES patterns of the plasma jets with and without oxygen injected. It can be seen that the OES signals of the plasma jet are intensified when the oxygen is injected, especially in the case that ethanol is completely combusted., This result indicates that the injection of oxygen increases the enthalpy of the plasma jet. The result is also in good agreement with the combustion reaction of ethanol, as shown in Eq. (1)- (5). It is commonly accepted that a higher enthalpy plasma jet helps to improve the density of the coating. That is why the coating density is significantly improved when oxygen is injected.

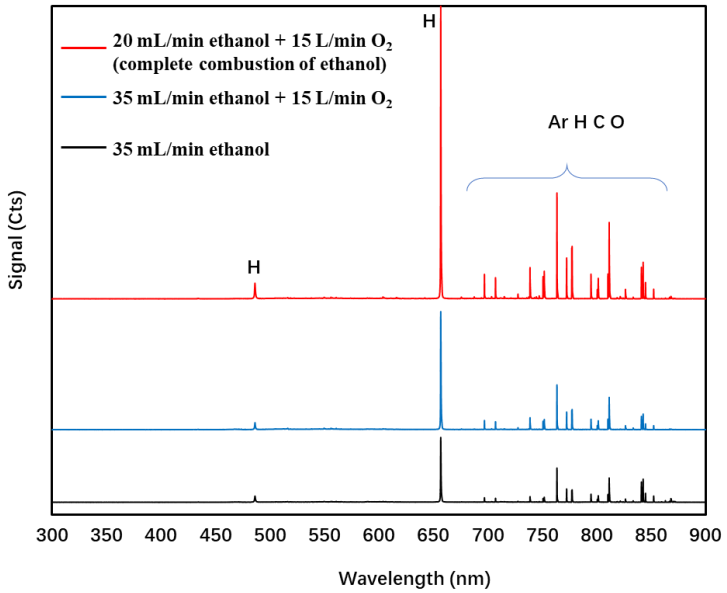

Fig. 4.16 OES patterns of the plasma jets with and without oxygen injected

4.4 Effect of the spraying distance on the microstructure of the coating

4.4.1 Preparation conditions of the coatings

The detailed spraying parameters are shown in Table 4.3. In this section, three spraying distances of 100 mm, 120 mm and 140 mm are set to investigate the effect of the spraying distance on the coating microstructure. Among the three spraying distances, 100 mm is the shortest spraying distance that the substrate can withstand.

Table 4.3 Experimental parameters of LPSPS YSZ coatings prepared at different spraying distances

Spraying parameters	air atmosphere
Environmental pressure (mbar)	200
Current (A)	680 × 2
Voltage (V)	54
Ar (L/min)	80
H_2(L/min)	22
Solvent type	ethanol
Solid content (wt%)	15
Suspension flow (mL/min)	35
Spraying distance (mm)	100/120/140
Spraying time (min)	9.5

4.4.2 Microstructure of the coatings

Fig. 4.17 shows the microstructure of the coatings prepared at different spraying distances. As the spraying distance increases, an internal detachment gradually occurs in the coating, accompanied by a decrease in coating thickness (Fig. 4.17a–Fig. 4.17c). It indicates that the interparticle adhesion is weakened as the spraying distance increases. In the magnified cross-sectional image (Fig. 4.17a'–Fig. 4.17c'), it can be observed that the density of the coating is greatly decreased with the spray distance increasing. The coating porosity is increased from 14.46 ± 1.74% to 37.22 ± 4.84% as the spraying distance increase from 100 mm to 140 mm, as shown in Fig. 4.18.

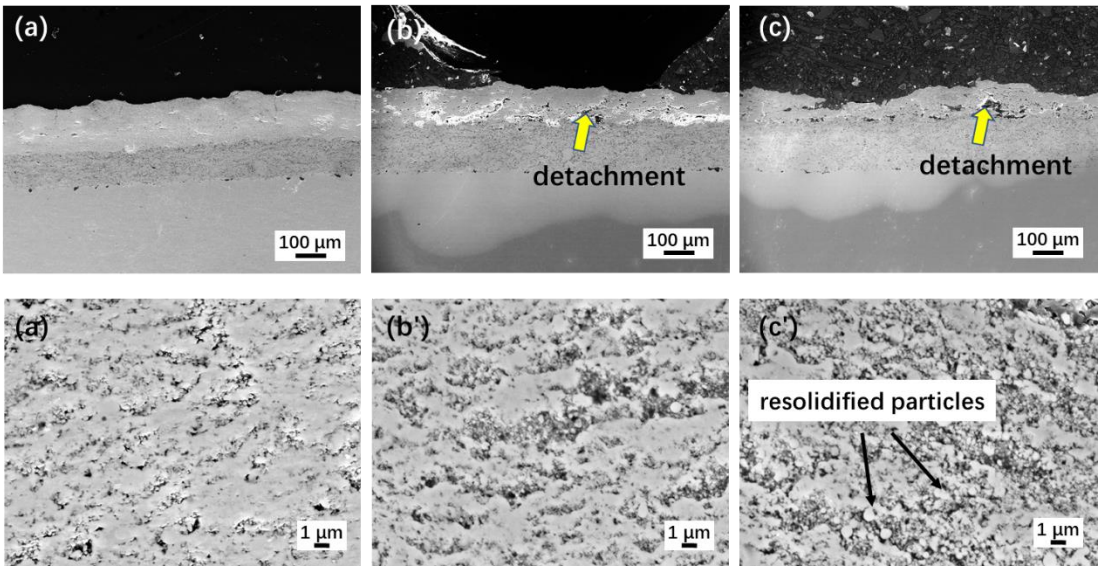

Fig. 4.17 SEM images of LPSPS YSZ coating prepared at different spraying distances: (a)(a') 100 mm, (b)(b') 120mm, (c)(c') 140mm

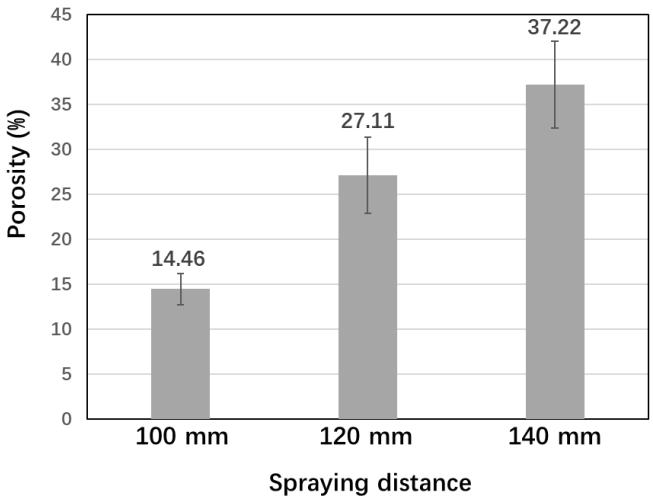

Fig. 4.18 Porosity of LPSPS YSZ coating prepared at different spraying distances

In terms of suspension plasma spraying, both particle temperature and particle velocity are greatly decreased with the distance increasing in the plasma jet, which results in the decrease of the coating density. In particular, an excessively long spraying distance will cause the resolidification of the melted in-flight particles [12]. These resolidified particles are not easily deformed when impacting the substrate (Fig. 4.17c'), which greatly lowers the interparticle adhesion, causing the internal detachment of the coating.

4.5 Effect of the suspension solid content on the microstructure of the coating

4.5.1 Preparation conditions of the coatings

In this section, the suspensions with three solid contents (5 wt%, 15 wt%, 25 wt%) are prepared to investigate the effect of solid content on the coating microstructure. The detailed spraying parameters are shown in Table 4.4.

Table 4.4 Experimental parameters of LPSPS YSZ coatings prepared with different suspension solid contents

Spraying parameters	air atmosphere
Environmental pressure (mbar)	200
Current (A)	680 × 2
Voltage (V)	54
Ar (L/min)	80
H_2(L/min)	22
Solvent type	ethanol
Solid content (wt%)	5/15/25
Suspension flow (mL/min)	35
Spraying distance (mm)	100
Spraying time (min)	9.5

4.5.2 Microstructure of the coatings

Fig. 4.19 shows the microstructure of the coatings prepared with different solid contents. With a low solid content (5 wt%), a large number of nanoparticles are formed on the surface of the coating (Fig. 4.19a). The coating thickness is rather inhomogeneous, and the partial region of the substrate is even not completely covered by the coating (Fig. 4.19a'). Additionally, some large holes are also formed in the coating. The coating

exhibits a quite porous microstructure with a high porosity of 25.58 ± 2.85% (Fig. 4.20).

With a medium solid content (15 wt%), the number of nanoparticles in the coating is decreased, while the number of spherical particles and splats significantly increases (Fig. 4.19b). The coating shows a relatively dense and homogeneous structure (Fig. 4.19 b' and 4.19b''), and the coating porosity is decreased to 14.46 ± 1.74%.

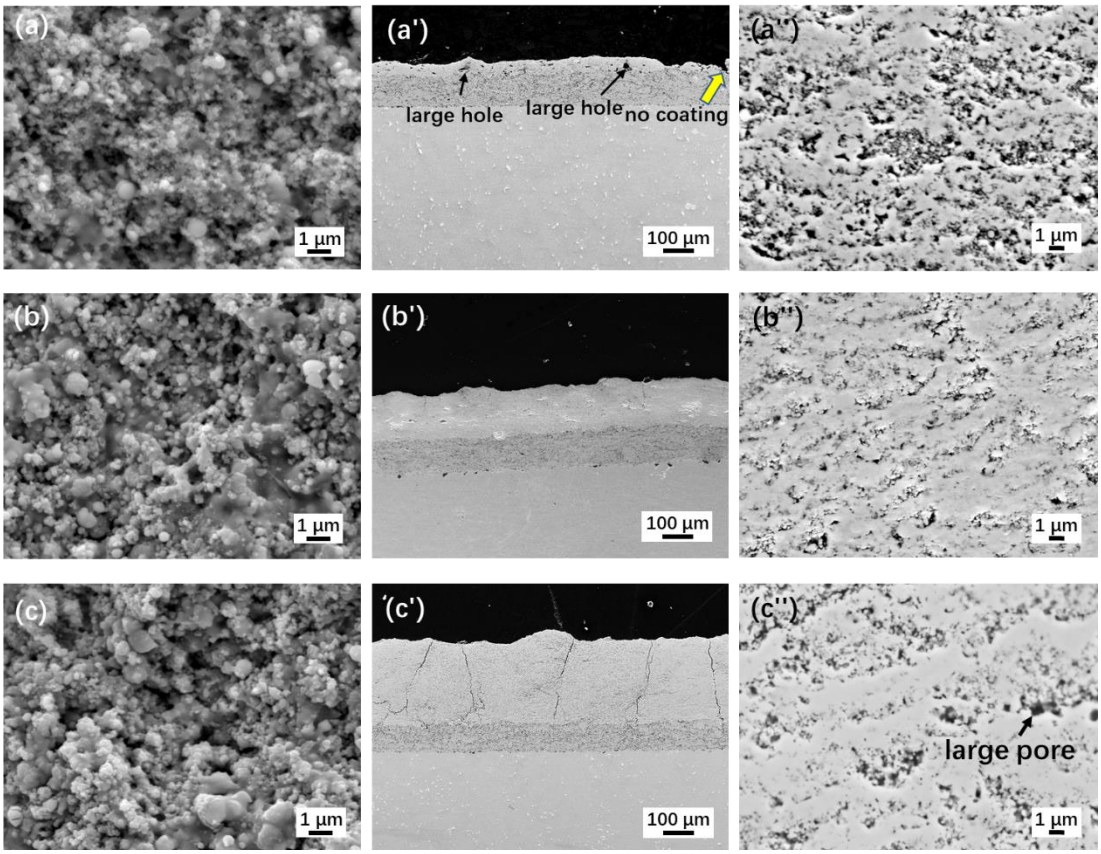

Fig. 4.19 SEM images of LPSPS YSZ coating prepared with different suspension solid content;(a-a'') 5 wt%, (b-b'') 15 wt%, (c-c'') 25 wt%

With a high solid content (25 wt%), the coating exhibits a similar surface morphology to the coating with 15 wt% of solid content. However, the size of the particle in the coating appears to be larger than that of the latter. In addition, the coating, in this case, shows a vertical crack-segmented structure, which is similar to the coating prepared in the argon, but the roughness of the coating, in this case, is much higher (Fig. 4.2b versus Fig. 4.19c'). The porosity of the coating is slightly increased to 17.36 ± 1.88%, and the pores are a little larger than that of 15 wt% of solid content. Such a

microstructure of the coating may have a potential application value for TBCs.

It should be noted that there is no linear correlation between the porosity and solid content. As shown in Fig. 4.20, the porosity of the coating is first largely decreased and then slightly increased. In general, a high solid content helps to improve the density of the coating. This conclusion has been demonstrated by many reports on the SPS coating [1, 13]. Due to a high suspension viscosity [14, 15], the suspension with the higher solid content tends to form larger droplets during the atomisation process. These larger droplets will subsequently turn into larger agglomerates with larger dynamic inertia and thermal inertia, therefore easily forming a denser coating. This rule is verified between the case of 5 wt% of solid content and the case of 15 wt% of solid content. However, excessively large agglomerates may enhance the shadow effect of the coating deposition, which causes more large pores in the coating (Fig. 4.19c"). For that reason, the porosity of coating with 25 wt% of solid content is a little higher than that of the coating with 15 wt% of solid content, and the pore size of the former is larger than that of the latter as well.

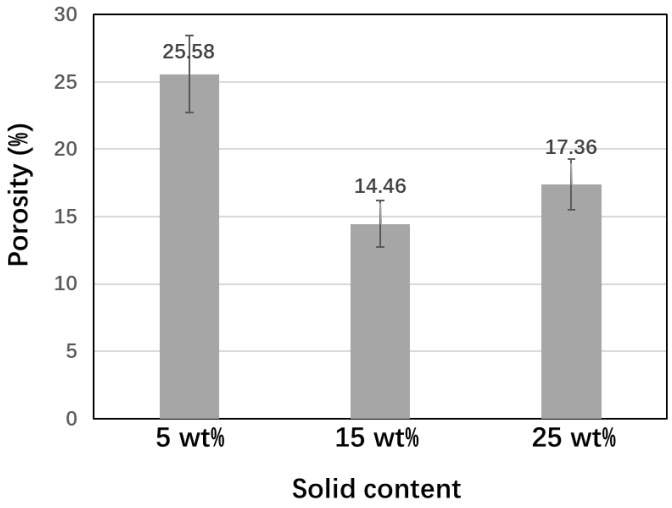

Fig. 4.20 Porosity of LPSPS YSZ coating prepared with different suspension solid contents

4.6 Effect of the solvent type on the microstructure of the coating

4.6.1 Preparation conditions of the coatings

In this section, two common suspension solvents: ethanol and water, are used to investigate the effect of suspension solvent on the coating microstructure. The detailed spraying parameters are shown in Table 4.5.

Table 4.5 Experimental parameters of LPSPS YSZ coatings prepared with different suspension solvents

Spraying parameters	air atmosphere
Environmental pressure (mbar)	200
Current (A)	680 × 2
Voltage (V)	54
Ar (L/min)	80
H_2(L/min)	22
Solvent type	ethanol/water
Solid content (wt%)	15
Suspension flow (mL/min)	35
Spraying distance (mm)	100
Spraying time (min)	9.5

4.6.2 Microstructure of the coatings

Fig. 4.21 shows the microstructure of the coatings. As seen from the surface image of the coatings (Fig. 4.21a and Fig. 4.21b), there is no significant difference in the surface morphology of both coatings. However, the particles of the water-based coating appear to be more tightly packed than those of the ethanol-based coating. Besides, no obvious vertical cracks are observed in the water-based coating, while some tiny cracks

can be observed in the ethanol-based coating (Fig. 4.21a' and Fig. 4.21b'). This indicates that the water-based coating has a stronger interparticle adhesion compared to the ethanol-based coating. The atomised droplets of water-based suspension are larger than those of ethanol-based suspension due to the weak atomisation ability of water. The larger droplets possess larger momentum, resulting in closer packing of interparticle force in the coating. Nevertheless, the porosity of the water-based coating is still similar to that of the ethanol-based coating, as shown in Fig. 4.22.

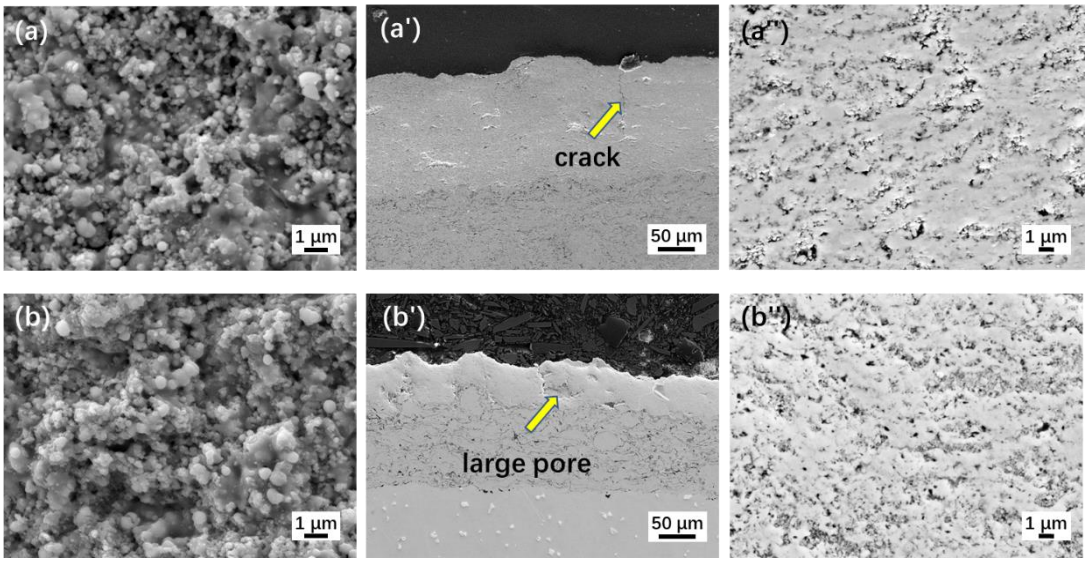

Fig. 4.21 SEM images of LPSPS YSZ coatings prepared with different solvents: (a-a") ethanol solvent, (b-b") water solvent

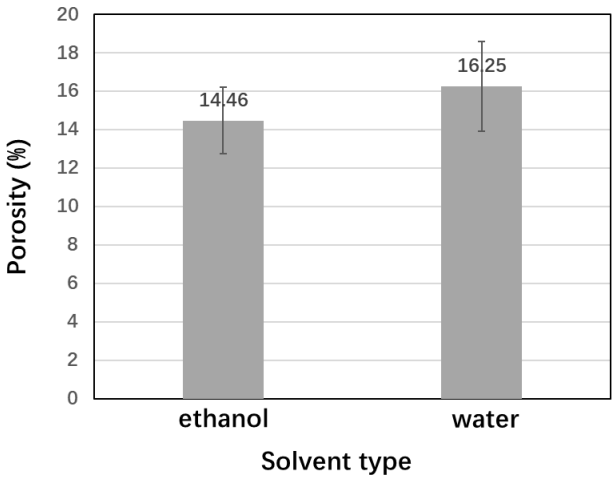

Fig. 4.22 Porosity of LPSPS YSZ coating prepared with different suspension solvents

4.6.3 Phase composition of the coatings

Fig. 4.23 shows the XRD patterns of the coatings. It can be seen that the diffraction peaks of the water-based coating are slightly weakened compared to those of the ethanol-based coating. This reflects that the enthalpy of the water-injected plasma jet is lower than that of the ethanol-injected plasma jet. This is because the vaporisation of water takes away much of the heat from the plasma jet, while the combustion of ethanol releases heat into the plasma jet. For that reason, the density of the water-based coating is not improved compared to that of the ethanol-based coating, even though the water-based coating exhibits a stronger interparticle adhesion.

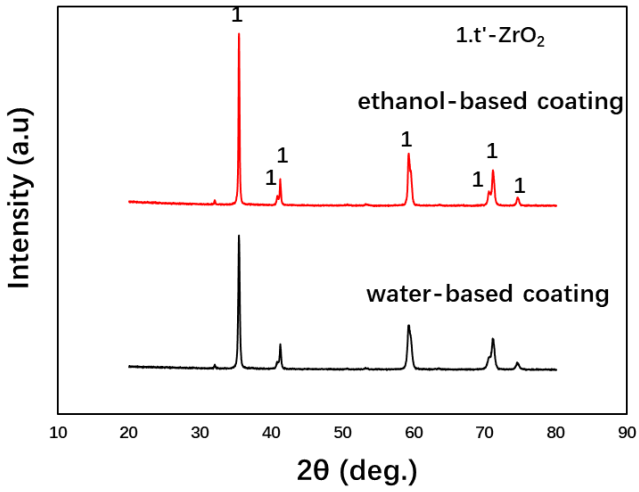

Fig. 4.23 XRD patterns of LPSPS YSZ coatings prepared with different suspension solvents

4.6.4 Clogging of the torch nozzle by water-based suspension during the spraying process

It should be noted that the torch nozzle was severely clogged by the suspension during the spraying process, as shown in Fig. 4.24, consequently producing a number of spatters on the surface of the coating. Also, for this reason, the deposition rate of the water-based coating is quite low, as shown in Fig. 4.21b'. These spatters destroy the homogeneousness of the coating, causing large pores in the place where the spatters exist (yellow arrow in Fig. 4.21b').

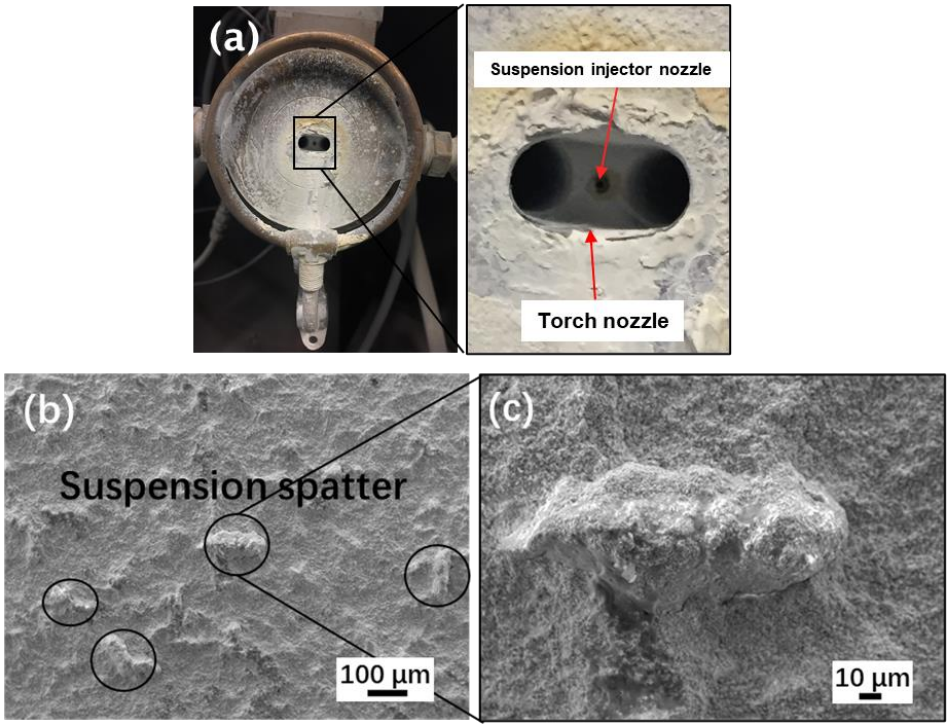

Fig. 4.24 Clogging of the torch nozzle by water-based suspension during the spraying process: (a) torch nozzle clogged by suspension, (b) surface morphology of the coating, (c) larger spatters on the coating surface

Fig. 4.25 shows the schematic of the suspension evolution inside the torch nozzle. Since the vaporisation of water is much harder than that of ethanol, the water remains in droplet form over a longer distance in the plasma jet. Coupled with the expanded spraying angle under low pressure, the unvaporised suspension stream, therefore, sticks to the inner wall of the torch nozzle and clog it at last.

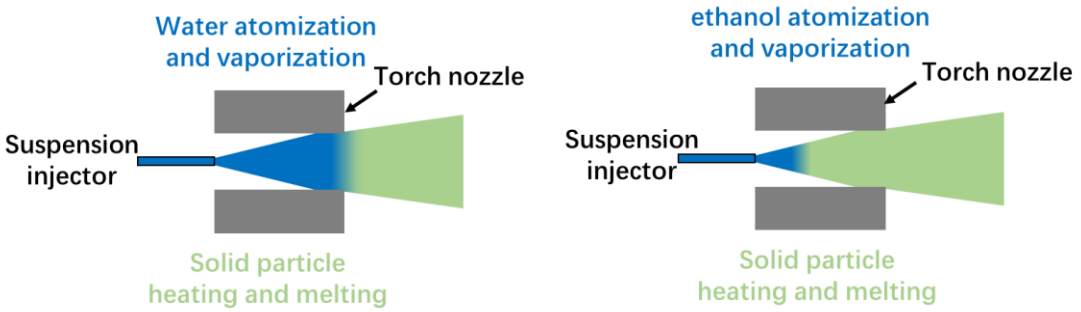

Fig. 4.25 Schematic of the suspension evolution inside the torch nozzles

4.7 Summary of structural characteristics of the LPSPS coatings

According to the results in this chapter, it is apparent that the microstructure of the LPSPS coating can be greatly tailored by varying the spraying conditions. Among these spraying conditions, the environmental atmosphere plays the most curtail role. In the argon, due to the carbon produced by the pyrolysis of ethanol, a huge number of nanoparticles are formed in the coating. In that case, the coating exhibits a low surface roughness, relatively low density and very poor adhesion. In contrast, in the air, the nanoparticles in the coating are largely removed. In that case, the coating exhibits an increased surface roughness, higher density and improved adhesion. It is not suitable for the LPSPS coating to prepare in the argon. The LPSPS coating is preferably prepared in the air

In addition to the environmental atmosphere, oxygen content in the environment is another important factor greatly influencing the structure of the coating. By injecting oxygen into the plasma jet, the enthalpy of the plasma jet can be significantly increased. As a result, a high-density coating can be prepared by LPSPS. Such a structure is expected to be applied in wear-resistant coatings and SOFC electrolytes.

In addition to high-density coating, a porous vertical crack structure can also be achieved by using LPSPS (Fig. 4.19c'), which shows the potential of LPSPS in the preparation of TBCs. Thanks to the higher particle velocity and smaller particle size in LPSPS, the coarse pores are significantly removed, and more micropores are formed in the LPSPS coating, which is expected to greatly lower the thermal conductivity of the coating. Besides, the vertical crack structure can provide the coating with high thermal strain tolerance. Moreover, the surface roughness of the LPSPS coating is much smaller than the SPS coating, which is expected to provide a better corrosion/erosion resistance for TBCs because such structures can reduce the accumulation of corrosive media like CMAS, at the same time slow their penetration into the coating.

4.8 Conclusion

In this chapter, the microstructure of the LPSPS coating is tailored by varying the spraying conditions. The main conclusions drawn from this chapter are summarised below:

1. The coating prepared in the argon exhibits a low surface roughness (Ra=2.28 μm), whereas the coating prepared in the air exhibits a much higher surface roughness (Ra=8.35 μm). The latter shows a denser microstructure than the former.
2. In the argon atmosphere, carbons are produced in the plasma jet due to ethanol pyrolysis, which causes a large number of nanoparticles in the coating, at the same time, greatly lowers the adhesion of the coating. The argon atmosphere is not suitable for the preparation of LPSPS coating. However, in the air atmosphere, no carbon is produced in the plasma jet due to ethanol combustion. Nanoparticles are largely removed. As a result, the density and adhesion of the coating are significantly improved.
3. The combustion of ethanol can greatly influence the enthalpy of the plasma jet in LPSPS. A high-density coating can be prepared with a high-enthalpy plasma jet, which can be achieved by injecting oxygen into the plasma jet during the spraying process.
4. The density of the coating is significantly decreased as the spray distance increases, while it is increased first and then decreased as the suspension solid content increases. By adjusting the spraying processes, a vertical crack-segmented structure can be tailored.
5. The coating prepared with water solvent has stronger interparticle adhesion than that prepared with ethanol solvent. However, the density of the coating is not significantly improved in that case. In addition, when water is used as the solvent, the torch nozzle is severely clogged by the suspension during the spraying process, producing a large number of suspension spatters on the coating surface.

References

[1] M. Shahien, M. Suzuki, Y. Tsutai, Controlling the coating microstructure on axial suspension plasma spray process, Surface and Coatings Technology 356 (2018) 96-107.

[2] M. Gupta, N. Markocsan, X.H. Li, B. Kjellman, Development of bondcoats for high lifetime suspension plasma sprayed thermal barrier coatings, Surface and Coatings Technology 371 (2019) 366-377.

[3] A. Ganvir, S. Joshi, N. Markocsan, R. Vassen, Tailoring columnar microstructure of axial suspension plasma sprayed TBCs for superior thermal shock performance, Materials & Design 144 (2018) 192-208.

[4] M. Gizynski, X. Chen, N. Dusautoy, H. Araki, S. Kuroda, M. Watanabe, Z. Pakiela, Comparative study of the failure mechanism of atmospheric and suspension plasma sprayed thermal barrier coatings, Surface and Coatings Technology 370 (2019) 163-176.

[5] H.B. Guo, R. Vaßen, D. Stöver, Atmospheric plasma sprayed thick thermal barrier coatings with high segmentation crack density, Surface and Coatings Technology 186(3) (2004) 353-363.

[6] A. Hospach, G. Mauer, R. Vaßen, D. Stöver, Characteristics of Ceramic Coatings Made by Thin Film Low Pressure Plasma Spraying (LPPS-TF), Journal of Thermal Spray Technology 21(3-4) (2012) 435-440.

[7] G.M. lngo, Origin of Darkening in 8 wt% Yttria-Zirconia Plasma-Sprayed Thermal Barrier Coatings, J Am Cerarn Soc 74 [2] 381-86(1991)

[8] D. Sen, S. Mazumder, J.S. Melo, A. Khan, S. Bhattyacharya, S.F. D'Souza, Evaporation Driven Self-Assembly of a Colloidal Dispersion during Spray Drying: Volume Fraction Dependent Morphological Transition, Langmuir 25(12) (2009) 6690-6695.

[9] M. Trunec, K. Maca, Advanced Ceramic Processes, Advanced Ceramics for Dentistry, Elsevier, 2014, pp. 123-150.

[10] R. Shi, M. Ren, H. Li, J. Zhao, S. Liu, Z. Li, J. Ren, Graphene supported Cu

nanoparticles as catalysts for the synthesis of dimethyl carbonate: Effect of carbon black intercalation, Molecular Catalysis 445 (2018) 257-268.

[11] J. Yan, T. Wei, B. Shao, F. Ma, Z. Fan, M. Zhang, C. Zheng, Y. Shang, W. Qian, F. Wei, Electrochemical properties of graphene nanosheet/carbon black composites as electrodes for supercapacitors, Carbon 48(6) (2010) 1731-1737.

[12] V. Carnicer, M.J. Orts, R. Moreno, E. Sánchez, Influence of solids concentration on the microstructure of suspension plasma sprayed Y-TZP/Al2O3/SiC composite coatings, Surface and Coatings Technology 371 (2019) 143-150.

[13] N. Curry, K. VanEvery, T. Snyder, J. Susnjar, S. Bjorklund, Performance Testing of Suspension Plasma Sprayed Thermal Barrier Coatings Produced with Varied Suspension Parameters, Coatings 5(3) (2015) 338-356.

[14] D. Sen, S. Mazumder, J.S. Melo, A. Khan, S. Bhattyacharya, S.F. D'Souza, Evaporation driven self-assembly of a colloidal dispersion during spray drying: volume fraction dependent morphological transition, Langmuir 25(12) (2009) 6690-5.

[15] D. Waldbillig, O. Kesler, The effect of solids and dispersant loadings on the suspension viscosities and deposition rates of suspension plasma sprayed YSZ coatings, Surface and Coatings Technology 203(15) (2009) 2098-2101.

Chapter 5 Application of low-pressure suspension plasma spraying in solid oxide fuel cell

Chapter 5: Application of low-pressure suspension plasma spraying in solid oxide fuel cell

In this chapter, YSZ electrolyte and lanthanum silicate electrolyte are deposited by the developed LPSPS processes in the previous chapters. The microstructure, crystallinity and gas permeability of both electrolytes are investigated.

5.1 Introduction

According to the preliminary research results of this thesis, LPSPS has a foreseeable potential in the preparation of TBCs and high-density coating (wear-resistant coatings, SOFC electrolytes, etc.). Unfortunately, due to the severe erosion of the anode, the bi-cathode plasma torch used in this thesis no longer has the ability to prepare a very thick coating (It requires a longer spraying time); thus, the application of LPSPS in TBCs will not be studied in this thesis. Instead, this chapter will focus on the application of the LPSPS in the electrolyte of solid oxide fuel cells (SOFC).

In this chapter, 8mol% YSZ (YSZ) electrolyte and $La_9SrSi_6O_{26.5}$ (LSSO) electrolyte will be prepared by LPSPS. These two electrolytes are used in high-temperature SOFC and intermediate-temperature SOFC, respectively. The preparation processes of the electrolytes are based on those developed in the previous chapters. The microstructure, crystallinity and gas permeability of both electrolytes are investigated to preliminarily examine the application of LPSPS in SOFC.

5.2 Preparation conditions of the electrolytes

The experimental parameters are displayed in table 5.1. For comparison, a YSZ electrolyte coating is also prepared by SPS. In this study, in order to reduce the erosion of the torch, the torch current is decreased from 680 A to 580 A. At the same time, the effect of plasma gas composition on the coating microstructure is investigated as well.

Table 5.1 Preparation parameters of the electrolytes

Spraying parameters	SPS-YSZ	LPSPS-YSZ	LPSPS-He-YSZ	LPSPS-He-LSSO
Environmental pressure	980 mbar	200 mbar	200 mbar	200 mbar
Environmental atmosphere	air	air	air	air
Current (A)	580×2	580×2	580×2	580×2
Voltage(V)	55	55	55	55
Powder	8 mol% YSZ	8 mol% YSZ	8 mol% YSZ	$La_9SrSi_6O_{26.5}$
Plasma gas (L/min)	Ar/H_2: 80/22	Ar/H_2: 80/22	Ar/H_2/He: 60/12/100	Ar/H_2/He: 60/12/100
Solvent type	ethanol	ethanol	ethanol	ethanol
Solid content (wt %)	15	15	15	15
Suspension flow (mL/min)	20	20	20	20
Additional O_2 (L/min)	15	15	15	15
Spraying distance(mm)	50	100	100	100

5.3 Microstructures of the electrolytes

Fig. 5.1 shows the microstructures of the SPS-YSZ electrolyte. The surface of the coating shows a number of cauliflower morphologies in which large gaps and pores exist (Fig. 5.1a' and Fig. 5.1a'). In the cross-sectional image (Fig. 5.1b), the thickness of the electrolyte shows poor uniformity. Moreover, severe spallation occurs in the anode layer. It should be noted that the pores are mostly dispersed in the column of the electrolyte (region 1 in Fig. 5.1c). As mentioned before, due to a low Stokes number of the deposited particles under atmospheric pressure, the coating tends to form a columnar structure. Specifically, the column is mainly deposited by the small particles with low momentum, while the flat region is mainly deposited by large particles with high momentum. For that reason, the pores are unevenly dispersed in the coating. Due to the columnar structure, many gaps and pores are formed in the coating, which is detrimental

to the gas-tightness of the electrolyte. In conclusion, such a porous structure of the SPS-YSZ electrolyte is not appropriate as the electrolyte of SOFC. Nevertheless, it is likely to be appropriate for the electrode layers of SOFC because the porous structure provides a higher surface for the catalytic reaction in the electrodes.

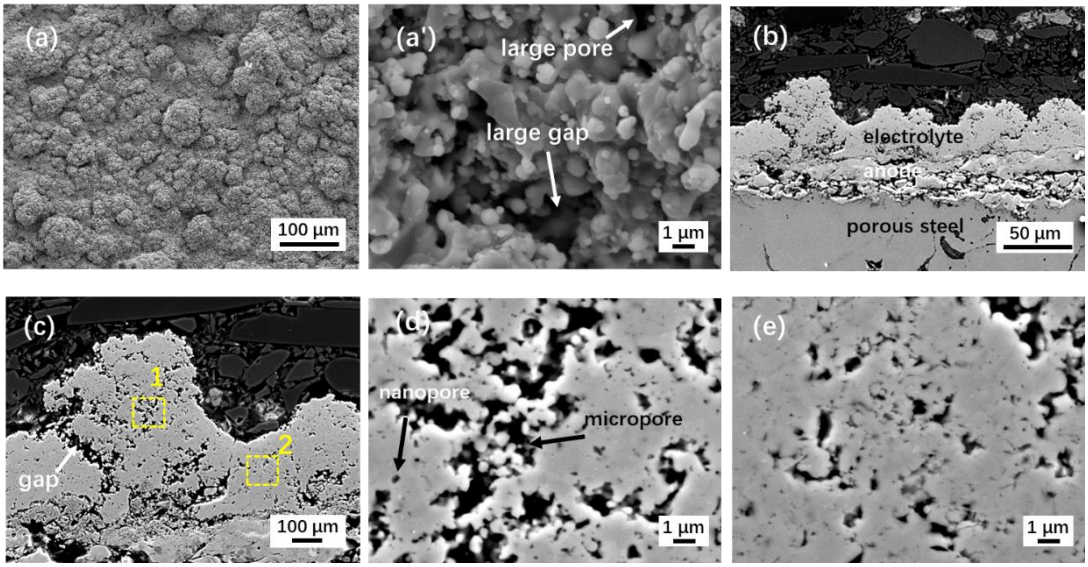

Fig. 5.1 SEM images of the SPS-YSZ electrolyte: (a)(a') surface morphology, (b)(c) cross-sectional morphology, (d) magnified image of region 1 in Fig. 5.1c, (e) magnified image of region 2 in Fig. 5.1c

Fig. 5.2 shows the microstructures of the LPSPS-YSZ electrolyte. The electrolyte exhibits a much flatter and more compact surface morphology compared to the SPS-YSZ electrolyte. Since the torch current in this study is decreased to 580 A, small particles, especially nanoparticles, are formed in the coating again. As a result, the electrolyte density is decreased compared to the high-density coating in chapter 4. Nevertheless, in this case, no spallation and crack can be observed at the interface of the electrolyte or anode, exhibiting a good coverage between both. This should be attributed to the lower cooling rate of the sample under low pressure, which prevents the excessive stress concentration between the electrolyte and anode. As seen in Fig. 5.2b, the electrolyte still shows a high density at low magnification, in which no visible pores can be observed. However, in the high-magnification image (Fig. 5.2b'), a large number of

micropores filled with the nanoparticle can be observed in the coating. Nevertheless, the density of the LPSPS-YSZ electrolyte is still much higher than the SPS-YSZ electrolyte.

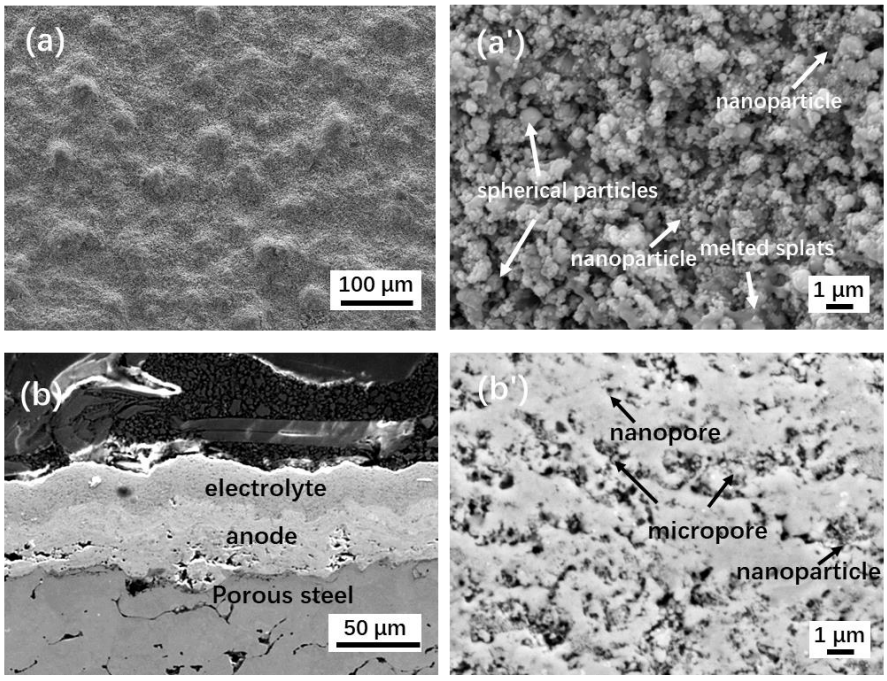

Fig. 5.2 SEM images of the LPSPS-YSZ electrolyte: (a)(a') surface morphology, (b)(b') cross-sectional morphology

Fig. 5.3 shows the microstructures of the LPSPS-He-YSZ electrolyte. In this case, helium was added to the plasma jet for electrolyte preparation. It can be observed that the electrolyte shows a similar surface morphology to the LPSPS-YSZ electrolyte (Fig. 5.3a). However, more melted splats are formed in the coating, and the nanoparticles are remarkedly reduced (Fig. 5.3a'). As a result, the LPSPS-He-YSZ electrolyte shows a higher density than the LPSPS-YSZ electrolyte. In terms of plasma sprayings, hydrogen and helium are two of the main plasma gases used to enhance the enthalpy of the plasma jet. Generally speaking, the plasma jet with helium is more concentrated and also has a higher enthalpy in comparison to hydrogen [1, 2], due to the higher viscosity and thermal conductivity of helium. Therefore, when helium is used as the plasma gas, the resulting coating typically exhibits a high density. However, considering the high cost of

helium, most plasma sprayings use hydrogen as the plasma gas. Helium is mainly used in LPPS in order to compensate for the limited torch power [3, 4]. From this point of view, helium can also be used in LPSPS to improve the density of the coating; however, a potential disadvantage of helium to the behaviour of the suspension should be considered. Since helium has a high viscosity, it may produce a stronger drag force on the suspension droplets. As a result, the suspension is more easily fragmented into small droplets, which is detrimental to the density of the resulting coating, as mentioned before. This may also explain the existence of the nanoparticles on the LPSPS-He-YSZ electrolyte (Fig.5.3a').

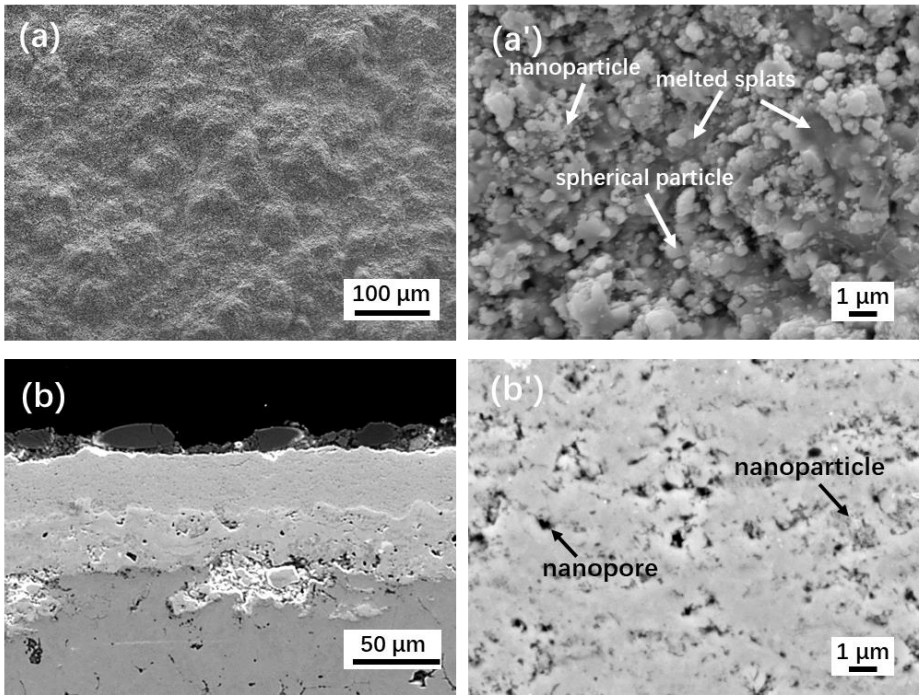

Fig. 5.3 SEM images of the LPSPS-He-YSZ electrolyte: (a)(a') surface morphology, (b)(b') cross-sectional morphology

Fig. 5.4 shows the microstructure of the LPSPS-He-LSSO electrolyte. It can be observed that the electrolyte exhibits a rather dense microstructure. No noticeable pores can be observed in the surface or cross-sectional image with low magnification (Fig. 5.4a and Fig. 5.4b). In the surface image of the magnified images (Fig. 5.4a'), the surface of the electrolyte shows a sintering-like morphology, and only a few nanopores

can be seen. As seen from the cross-sectional image at high magnification (Fig. 5.4b'), only a few nanopores can be observed in the coating. Moreover, these nanopores appear to be unconnected with each other. The closed pores can prevent the penetration of gas, thus greatly improving the gas tightness of the electrolyte. The LPSPS-He-LSSO electrolyte exhibits a much denser microstructure than the LPSPS-He-YSZ electrolyte under the same spraying conditions. This can be explained in two aspects. First, the lanthanum silicate powder has a lower melting point than zirconia powder. Second, the size of the former is larger than the latter (~500 nm versus ~150 nm), as shown in Fig. 2.3. It will effectively eliminate the nanoparticles in the coating, thus decreasing the porosity of the coating.

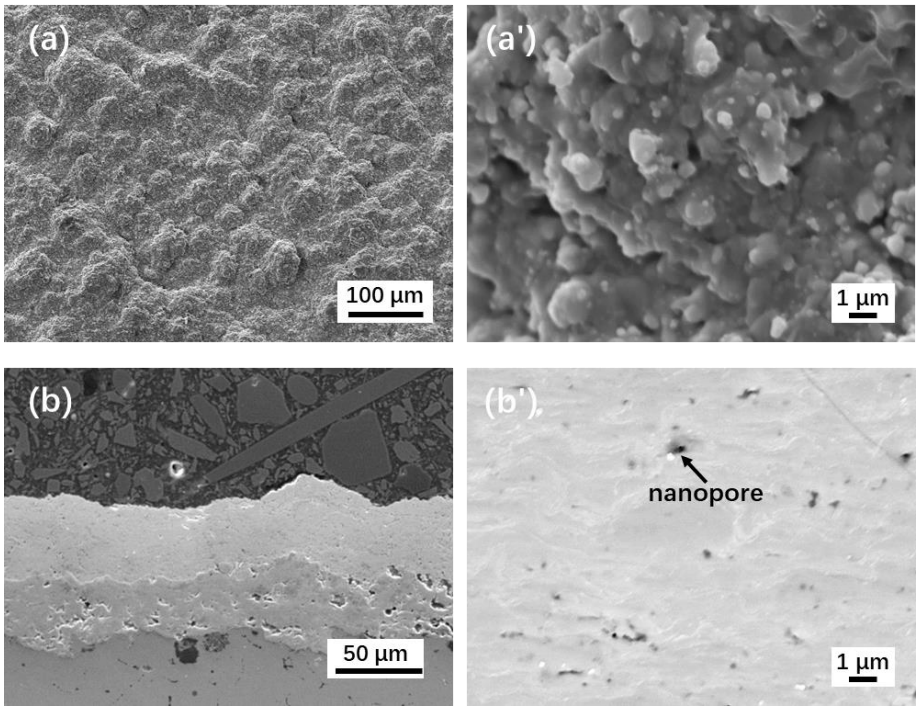

Fig. 5.4 SEM images of the LPSPS-He-LSSO electrolyte: (a)(a') surface morphology, (b)(b') cross-sectional morphology

5.4 Crystallinity of the electrolytes

Fig. 5.5 displays the XRD patterns of the two electrolytes prepared by LPSPS, as well as the corresponding powders. According to the intensity of the diffraction peaks,

the LPSPS-He-YSZ electrolyte exhibits a similar crystallinity to the feed powder, whereas the LPSPS-He-LSSO electrolyte exhibits a lower crystallinity than that of the feed powder. It reflects the lower thermal stability of lanthanum silicate compared to YSZ. Nevertheless, no apparent amorphous hump peak was observed in the XRD pattern of the LSSO electrolyte. Considering that the LSSO powder is prepared by high-temperature solid-phase sintering, the crystallinity of the feed powder is inherently very high. Hence, the LSSO electrolyte still exhibits a relatively high crystallinity. Generally speaking, the lanthanum silicate coating easily forms an amorphous phase when prepared by thermal sprayings [5-7]. The amorphous phase will seriously decrease the ionic conductivity of the electrolyte [8]; therefore, most thermal sprayed lanthanum silicate coatings require a post-heat treatment to eliminate the amorphous phase. The amorphous phase mainly results from the rapid quenching of the melted particle on the substrate. In the case of LPSPS, due to the low heat transfer in the low-pressure environment, the substrate remains at a high temperature during the spraying process. In addition, after spraying is completed, the cooling of the coating in the low-pressure environment is much slower than in the atmospheric environment. Both of the above factors can restrain the formation of the amorphous phase. This result reflects the unique advantage of LPSPS in the preparation of lanthanum silicate electrolytes.

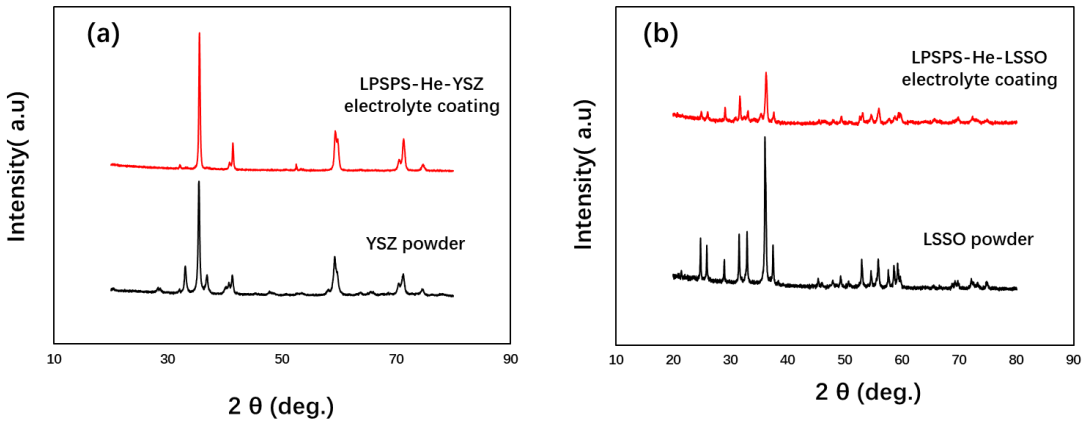

Fig. 5.5 XRD patterns of the feed powders and the electrolytes: (a) LPSPS-He-YSZ electrolyte and YSZ powder; (b) LPSPS-He-LSSO electrolyte and LSSO powder

5.5 Roughness of the electrolytes

The surface roughness of the electrolytes is shown in Fig. 5.6. The SPS-YSZ electrolyte exhibits a much higher roughness than that prepared by LPSPS. The use of He appears to slightly decrease the surface roughness, which could be attributed to the higher velocity of the particle with the addition of He. In addition, the LSSO electrolyte shows a higher roughness compared to the YSZ electrolytes. This may be due to the lower specific mass of LSSO powder. In that case, the deposited particle has a lower S_t. In that case, it is easier for the coating to form the cauliflower morphologies (Fig. 5.4a). However, since these deposited particles have a relatively low melting point, the electrolyte still exhibits a rather low porosity even though it possesses a cauliflower surface morphology like the SPS-YSZ electrolyte (Fig. 5.1a).

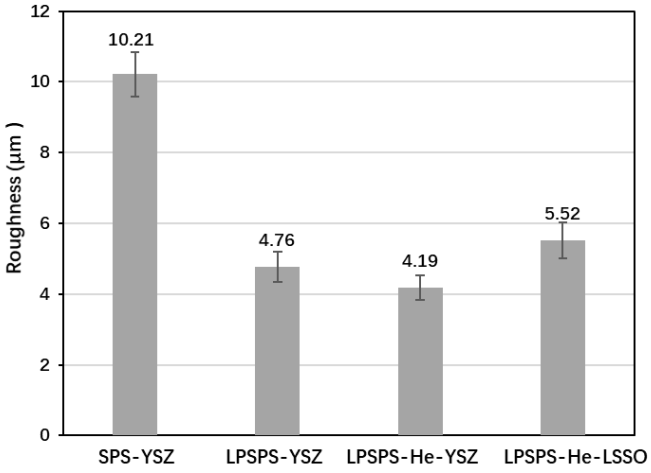

Fig. 5.6 Surface roughness of the electrolytes

5.6 Deposition rate of the electrolytes

Fig. 5.7 displays the deposition rate of the electrolytes. Herein, the deposition rate is defined as the deposit thickness per spraying pass. One spraying pass refers to one deposited layer of the coating. The coating is stacked by multiple deposited layers. In that case, the calculated deposition rate is not influenced by the number or size of the sample, so it can more accurately reflect the 'work efficiency' of the LPSPS technique.

As seen in Fig. 5.7, the LPSPS electrolytes show a low deposition rate. The coating is deposited at a thickness of only 1–2 μm per spraying pass. Although this value is much lower than that (20–30 μm) of conventional plasma spraying, it is still much higher than that of PVD and CVD. The low deposition rate of the LPSPS coating is beneficial for the accurate control of the coating thickness, which is advantageous for the preparation of thin SOFC electrolytes. In addition, by comparing the deposition rate of electrolytes, the deposition rate of the coating is slightly increased after the addition of helium. Moreover, the deposition rate of the LSSO electrolyte is higher than that of the YSZ electrolyte. The above phenomena are closely related to the melted particles in the coating. Generally speaking, the melted particles are easier to deposit on the substrate. The LPSPS-He-LSSO electrolyte contains more melted particles, as shown in Fig. 5.4a', thereby increasing the deposition rate of the coating.

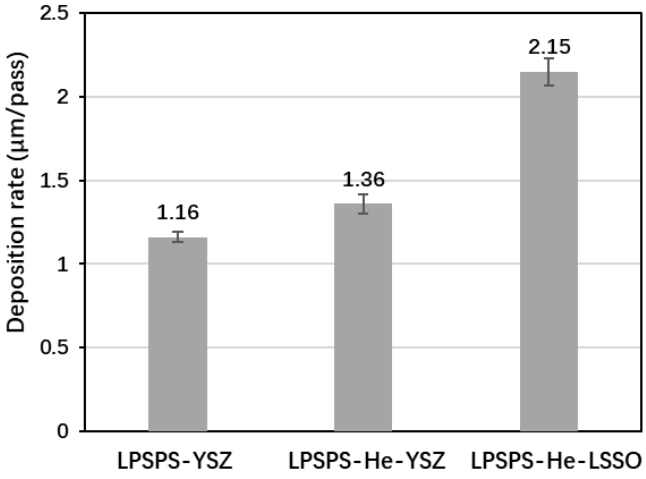

Fig. 5.7 Deposition rate of the electrolytes

5.7 Gas permeability of the electrolytes

Fig. 5.8 shows the gas permeability of the electrolytes. It can be seen that the gas permeability ($7.09 \pm 0.80 \times 10^{-17}$ m^2) of the LPSPS-He-YSZ electrolyte is more than two times higher than that ($3.02 \pm 0.23 \times 10^{-17}$ m^2) of the LPSPS-He-LSSO electrolyte. This result is in good agreement with the density of both electrolytes. It has been widely

verified that a denser coating causes a low gas permeability [9-11].

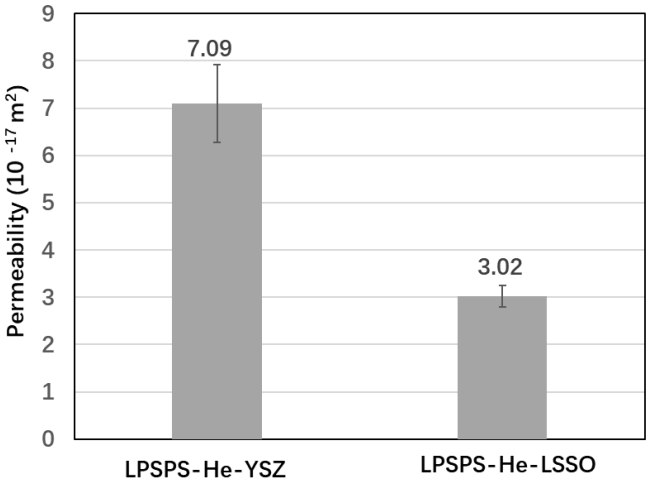

Fig. 5.8 Gas permeability of the electrolytes

Table 5.2 shows a summary of the gas permeability of plasma-sprayed electrolytes in the literature. Overall, the gas permeability of the LPSPS electrolytes in this thesis is higher than that of the LPPS electrolyte but lower than that of the APS electrolytes. However, it should be noted that the thickness of the LPSPS electrolyte in this thesis is only 30-50 μm， while the thickness of the APS electrolytes or the LPPS electrolyte is more than 100 μm or even up to 900 μm. Generally speaking, a high thickness helps to decrease the gas permeability of the electrolyte. However, it will also increase the ionic resistance of the electrolyte. Given the low thickness and the low gas permeability of the LPSPS electrolytes, the LPSPS shows a great advantage in the SOFC electrolyte compared to other plasma spraying processes.

According to Darcy's law, gas permeability uniquely depends on the internal geometry of the material. In the micropore and nanopore, the free movement range of gas molecules is largely limited. The collision between the molecules and the pore wall is enhanced, while the collisions between gas molecules are weakened [12, 13]. Therefore, the real gas viscosity in the pores is decreased, which somehow decreases the permeability. In other words, the fine internal structure of the LPSPS coating is beneficial for the reduction of gas permeability, which reflects the potential value of LPSPS in the

preparation of SOFC.

Table 5.2 Summary of the gas permeability of plasma-sprayed electrolytes in the literature

Electrolyte	Size of feed powder (μm)	Tested electrolyte thickness（μm）	Permeability (m^2)	Test gas	Preparation method	Ref.
YSZ	0.15	30~50	7.09×10^{-17}	H_2	LPSPS	This thesis
YSZ	25.60	900	1.30×10^{-16}	H_2	APS	[14]
YSZ	5.00-25.00	600~800	1.32×10^{-17}	Air	LPPS	[15]
$La_9SrSi_6O_{26.5}$	0.50	30~50	3.02×10^{-17}	H_2	LPSPS	This thesis
$La_{10}Mg_{0.2}Si_{5.8}O_{26.8}$	20.08	100~200	1. ~2.65×10^{-16} 2. ~1.50×10^{-16} (900 ℃ × 4h post-treatment)	H_2	APS	[16]
$La_{10}Mg_{0.2}Si_{5.8}O_{26.8}$	20.08	100~200	3.58×10^{-19}	H_2	LPPS	[17]

5.8 Conclusion

Based on the processes developed in the previous chapters, in this chapter, YSZ electrolyte and the lanthanum silicate electrolyte are prepared by LPSPS. The main conclusions are listed below:

1. The electrolyte prepared by SPS exhibits a porous structure. Such a structure is detrimental to the air tightness of the electrolyte.
2. The electrolyte prepared by LPSPS exhibit a uniform structure, and their density is significantly improved in comparison to that prepared by SPS.
3. The addition of helium can significantly increase the density of the electrolyte.
4. The crystallinity of the lanthanum silicate electrolyte is reduced compared to that of feedstock powder, but no obvious amorphous phase is formed in that case.
5. The density of the lanthanum silicate electrolyte is higher than that of the YSZ electrolyte, and the gas permeability of the former is also lower than that of the latter.

6. Both LPSPS electrolytes have a low gas permeability even in a low thickness (30~50 μm), which indicates the advantage of LPSPS in the preparation of SOFC electrolytes.

References

[1] A. Anwaar, L. Wei, H. Guo, Plasma characteristics and coating microstructures of yttria stabilized zirconia during plasma spray physical vapor deposition, 2017 14th International Bhurban Conference on Applied Sciences and Technology (IBCAST), IEEE, 2017.

[2] G. Mauer, A. Hospach, R. Vaßen, Process development and coating characteristics of plasma spray-PVD, Surface and Coatings Technology 220 (2013) 219-224.

[3] W. He, G. Mauer, A. Schwedt, O. Guillon, R. Vaßen, Advanced crystallographic study of the columnar growth of YZS coatings produced by PS-PVD, Journal of the European Ceramic Society 38(5) (2018) 2449-2453.

[4] D.T.L. N. N Zhang, Y. L. Li, Y. Zhang, M. P. Planche, H. L. Liao, C. Coddet, F. Y. Dong, In-flight particle characterization and coating formation under low pressure plasma spray condition, Journal of Iron and Steel Research International 24 (2017) 306-312.

[5] S. Dru, E. Meillot, K. Wittmann-Teneze, R. Benoit, M.L. Saboungi, Plasma spraying of lanthanum silicate electrolytes for intermediate temperature solid oxide fuel cells (ITSOFCs), Surface and Coatings Technology 205(4) (2010) 1060-1064.

[6] W. Gao, H.-L. Liao, C. Coddet, Effect of Gun Current on Electrical Properties of Atmospheric Plasma-Sprayed Lanthanum Silicate Coatings, Journal of Thermal Spray Technology 22(7) (2013) 1103-1108.

[7] Y.-X. Liu, S.-F. Wang, Y.-F. Hsu, C.-H. Wang, Solid oxide fuel cells with apatite-type lanthanum silicate-based electrolyte films deposited by radio frequency magnetron sputtering, Journal of Power Sources 381 (2018) 101-106.

[8] W.Z. Wang, F. Sun, X.P. Guo, H.L. Liao, O. Elkedim, J.C. Liang, Effect of substrate surface temperature on the microstructure and ionic conductivity of lanthanum silicate coatings deposited by plasma spraying, Surface and Coatings Technology 205(12) (2011) 3665-3670.

[9] M. Marr, O. Kesler, Permeability and Microstructure of Suspension Plasma-Sprayed

YSZ Electrolytes for SOFCs on Various Substrates, Journal of Thermal Spray Technology 21(6) (2012) 1334-1346.

[10] M. Marr, J. Kuhn, C. Metcalfe, J. Harris, O. Kesler, Electrochemical performance of solid oxide fuel cells having electrolytes made by suspension and solution precursor plasma spraying, Journal of Power Sources 245 (2014) 398-405.

[11] H. Tsukuda, A. Notomi, and N. Hisatome, Application of Plasma Spraying to Tubular-Type Solid Oxide Fuel Cells Production, Journal of Thermal Spray Technology, 9(3) (2000) 364-368.

[12] X. Duan, Z. Hu, N. Shao, W. Li, Y. Li, J. Chang, R. Shen, Establishment of a new slip permeability model of gas flow in shale nanopores based on experimental and molecular dynamics simulations studies, Journal of Petroleum Science and Engineering 193 (2020).

[13] C. Zhang, W.-Y. Li, M.-P. Planche, C.-X. Li, H. Liao, C.-J. Li, C. Coddet, Study on gas permeation behaviour through atmospheric plasma-sprayed yttria stabilized zirconia coating, Surface and Coatings Technology 202(20) (2008) 5055-5061.

[14] C. Zhang, C.-J. Li, H. Liao, M.-P. Planche, C.-X. Li, C. Coddet, Effect of in-flight particle velocity on the performance of plasma-sprayed YSZ electrolyte coating for solid oxide fuel cells, Surface and Coatings Technology 202(12) (2008) 2654-2660.

[15] C. Zhang, H.L. Liao, W.Y. Li, G. Zhang, C. Coddet, C.J. Li, C.X. Li, X.J. Ning, Characterization of YSZ Solid Oxide Fuel Cells Electrolyte Deposited by Atmospheric Plasma Spraying and Low Pressure Plasma Spraying, Journal of Thermal Spray Technology 15(4) (2006) 598-603.

[16] F.SUN, Caractérisation de revêtements de silicate de lanthane de structure apatite dopé au magnésium réalisés par projection plasma en vue d'application comme électrolyte de pile à combustible de type IT-SOFC Université de Technologie de Belfort-Montbéliard, 2011.

[17] F. Sun, N. Zhang, J. Li, H. Liao, Preparation of dense silicate electrolyte coating with low pressure plasma spraying and very low pressure plasma spraying for

intermediate-temperature solid oxide fuel cells, Journal of Power Sources 223 (2013) 36-41.

Conclusions and perspectives

Conclusions and perspectives

Conclusions

To the best of the authors' knowledge, this thesis is the first systematic report on LPSPS, involving an integrated investigation from the development of this technology to its application. Its main contributions include: 1. the deposition mechanism of LPSPS is proposed for the first time; 2. some common defects of the previous LPSPS coatings, such as poor adhesion, low mechanical strength, are significantly improved in this thesis; 3. many structural characteristics, such as a vertical crack structure and a high-density structure, are successively tailored; 4. the application of LPSPS in the SOFC electrolyte is preliminarily examined. The main conclusions of this thesis are shown as follow:

In the first part, the effect of environmental pressure on the microstructure of the YSZ coating prepared by suspension plasma spraying is investigated. The results show that as the pressure decreases from 980 mbar to 3 mbar, the surface roughness and the size of the particle in the coating gradually decrease, and the coating is transformed from a columnar structure to a vertical crack structure. The coarse pores in the coating gradually disappear under low pressure. In turn, more micropores are formed. These micropores are filled with nanoparticles, which somehow reduces the density of the coating. The suitable pressure for LPSPS cannot be too low; otherwise, the powders will be separated from the plasma jet, causing a large number of unmelted particles in the coating. The optimal pressure for LPSPS is 200mbar in this thesis.

In the second part, the LPSPS coating microstructures are tailored by varying the spraying conditions. These spraying conditions include environmental atmosphere (argon versus air), oxygen content in the environment, spray distance, suspension solid content, solvent type. The results show that the environment atmosphere plays the most critical role in the microstructure of the coating. In the argon atmosphere, a large amount of carbon is produced in the plasma jet due to ethanol pyrolysis. Both carbon

and argon atmosphere inhibit the agglomeration of the nanoparticles. As a result, a large number of nanoparticles with the same size as the feed powder are formed in the coating. These nanoparticles decrease the density and adhesion of the coating. Meanwhile, the carbon at the interface between the substrate and coating somehow causes the spallation of the coating at last. However, in the air atmosphere, carbon is largely removed due to ethanol combustion. Hence, only a few nanoparticles are formed in the coating; moreover, the density and adhesion of the coating are greatly improved. The oxygen content in the environment can greatly influence the microstructure of the coating since it can influence the enthalpy of the plasma jet through the combustion reaction of ethanol. A high-density YSZ coating can be prepared by injecting oxygen into the plasma jet during the preparation process. The density of the coating is significantly decreased as the spray distance increases, while it is increased first and then decreased as the solid concentration increases. The interparticle adhesion in the coating prepared with water solvent appears to be stronger than that prepared with ethanol solvent. However, the density of the coating is not significantly improved in that case. Besides, when water is used as the solvent, the torch nozzle is severely clogged by the suspension during the spraying process, producing a large number of suspension spatters on the coating surface. In this chapter, after the adjusting of various parameters, a high-density structure and a vertical crack-segmented structure are successfully tailored.

In the last part of the thesis, based on the processes developed in the previous chapters, YSZ electrolyte and the lanthanum silicate electrolyte are prepared by LPSPS in order to examine LPSPS in the application of SOFC. The first results showed that both electrolytes prepared by LPSPS exhibit a uniform structure as well as much higher density than the YSZ electrolyte prepared by SPS. The density of the lanthanum silicate electrolyte is higher than that of the YSZ electrolyte, and the gas permeability of the former is also lower than that of the latter. The crystallinity of the lanthanum silicate electrolyte is reduced compared to that of feedstock powder, but no obvious amorphous phase is formed in that case. Overall, both LPSPS electrolytes have a low gas

permeability even in a low thickness (30~50 μm), which indicates the advantage of LPSPS in the preparation of SOFC electrolytes.

Perspectives

For the further development of LPSPS, there is still a lot of work that needs to be improved and studied.

1. The LPSPS system should be further modified. For instance, the geometry of the torch nozzle should be modified to make the plasma jet more concentrated under low pressure as well as to prevent the water-based suspension from sticking inside the nozzle. Besides, a torch with a higher power is required for the research of LPSPS in the future.
2. The feeding system also should be modified. The peristaltic pump used in this thesis caused unstable injection of the suspension in the case of low flow. A pneumatic pump should be a better choice for a stable injection of the suspension.
3. According to the study of the thesis, nanoparticles decrease the density and adhesion of the coating due to their low momentum. The powder used in LPSPS can be larger (1–2 μm), which should be essayed in further works.
4. In chapter 4, a vertical crack-structured coating was tailored (Fig. 4.19c'). It contains a large number of micropores rather than coarse pores, which can help to decrease the thermal conductivity of the coating. In addition, the vertical crack structure typically has better corrosion and erosion resistance (depending on the width of the vertical crack) than that of the columnar structure, which can be used as a top layer in the multilayer TBC to improve the durability of the TBCs. These characteristics imply the potential value of LPSPS in TBCs, which is necessary to be further verified and investigated.
5. According to the results in this thesis, it is possible to prepare various coating microstructures by using LPSPS. This technology provides an ideal platform for

the development of coatings for different applications. At the same time, it also has potential in the one-step preparation of the gradient coatings. For example, it can achieve the porosity gradient simply by controlling the injection of oxygen in the plasma jet during the preparation process.

Abstract

Suspension plasma spraying (SPS) has attracted more and more attention in terms of the preparation of nanostructured / sub-microstructured ceramic coatings. However, conventional SPS techniques are conducted under atmospheric pressure, which inevitably causes some disadvantages. Recently, a novel suspension spraying technology – low-pressure suspension plasma spraying (LPSPS) – was proposed, in which the suspension spraying process is conducted under low environmental pressure. Benefit from the significant impact of low pressure on the coating deposition, LPSPS is expected to improve the disadvantage of SPS as well as to obtain distinct coating structures not achievable in conventional SPS coatings. Currently, the reported LPSPS coatings commonly have a much denser structure compared to the SPS coatings. However, their adhesion and mechanical strength are quite low. More importantly, the structural characteristics of the LPSPS coating are still not fully understood. Its practical applications, especially the application in the electrolyte of SOFC, have not been fully studied and verified as well.

In this thesis, the authors further developed and studied LPSPS on the basis of limited references. We first investigated the effect of environmental pressure on the microstructure of the yttria-stabilised zirconia (YSZ) coating prepared by suspension plasma spraying. The results revealed that as the pressure decreased, the coating was transformed from a column-like structure to a vertical crack structure; a dramatic decrease in surface roughness was also observed. The size of the particle in the coating was significantly decreased as the pressure decreased. More nanoparticles were formed in the coating prepared under lower pressure. The required pressure for LPSPS cannot be too low; otherwise, the powders would be separated from the plasma jet, dramatically decreasing the quality of the coating. The optimal pressure for LPSPS in this thesis was 200 mbar.

Next, the microstructures of the LPSPS YSZ coating were comprehensively

tailored by varying the spraying conditions. These spraying conditions included environmental atmosphere (argon versus air), oxygen content in the environment, spray distance, suspension solid content and solvent type. Out of them, the environment atmosphere played the most critical role in the microstructure of the coating. The argon atmosphere was not suitable for LPSPS. The evolution modes of suspension in different atmospheres (air versus argon) were proposed. Finally, a high-density YSZ coating and a vertical crack structured YSZ coating were successfully tailored by adjusting the preparation parameters.

In the last part of the thesis, we attempted to deposit YSZ electrolyte and lanthanum silicate electrolyte by using the developed LPSPS processes in order to examine the application of this technology in the solid oxides fuel cell (SOFC). The first results showed that the density of the lanthanum silicate electrolyte was higher than that of the YSZ electrolyte and that the gas permeability of the former was lower than that of the latter. Both electrolytes exhibited a low gas permeability in the order of magnitude of 10^{-17} $m^{2,}$ even in a rather low thickness (30~50 μm). Moreover, they all exhibited a high crystallinity, and no amorphous phase was formed in the lanthanum silicate electrolyte. These results indicate that LPSPS has a huge potential in the preparation of the electrolyte of SOFC.

Keywords: nanostructured ceramic coating, low-pressure suspension plasma spraying, structural characteristics, spraying conditions, solid oxide fuel cell.

Résumé

La projection plasma de suspension (SPS) attire de plus en plus d'attention en termes de préparation de revêtements céramiques nanostructurés / sous-microstructurés. Cependant, les techniques SPS conventionnelles sont menées sous pression atmosphérique, ce qui inévitablement cause des désavantages. Récemment, une nouvelle technologie de projection plasma de suspension du nom de projection plasma de suspension sous basse pression (LPSPS) a été proposée, dans laquelle la projection de suspension est réalisée sous basse pression environnementale. Bénéficiant de l'impact significatif de basse pression sur le dépôt de revêtement, LPSPS devrait améliorer les désavantages de SPS et obtenir des structures de revêtement distinctes non réalisables dans les revêtements SPS conventionnels. Actuellement, les revêtements LPSPS rapporté ont généralement une structure beaucoup plus dense que les revêtements SPS. Cependant, leur adhérence et résistance mécanique sont très faibles. Plus important encore, les caractéristiques structurelles du revêtement LPSPS ne sont toujours pas entièrement comprises. Ses applications pratiques, en particulier l'application dans l'électrolyte de la pile à combustible à oxyde solide (SOFC) n'ont pas été entièrement étudiés et vérifiés.

Dans cette thèse, les auteurs ont continué de développé et étudié LPSPS sur la base de références limitées. Nous avons d'abord étudié l'effet de la pression environnementale sur la microstructure du revêtement de zircone stabilisée à l'yttria (YSZ) préparé par projection plasma de suspension. Les résultats ont révélé qu'au fur et à mesure que la pression diminuait, le revêtement était transformé d'une structure en forme de colonne à une structure segmentée par fissure verticale, ainsi qu'une diminution dramatique de la rugosité de surface. La taille des particules dans le revêtement était considérablement diminuée à mesure que la pression diminuait. Plus de nanoparticules se sont formées dans le revêtement préparé sous une pression plus basse. La pression requise pour le LPSPS ne peut pas être trop basse; sinon, les poudres seraient séparées du jet de plasma, ce qui réduirait considérablement la qualité du revêtement. La pression optimale pour le LPSPS dans cette thèse était de 200 mbar.

Ensuite, les conditions de projection ont été variées pour changer les microstructures du revêtement de LPSPS YSZ. Ces conditions comprenaient l'atmosphère environnementale (argon versus air), le teneur en oxygène dans l'environnement, le teneur en solides de la suspension, la distance de projection et la type de solvant. Parmi elles, l'atmosphère environnante a joué le rôle le plus critique dans les microstructures du revêtement. L'atmosphère d'argon n'était pas adaptée au LPSPS. Les modes d'évolution de la suspension dans différentes atmosphères (air versus argon) ont été proposé. Finalement, un revêtement YSZ avec haute densité et un revêtement YSZ structuré par fissures verticales ont été développés avec succès en ajustant les paramètres de préparation.

Dans la dernière partie de la thèse, nous avons tenté de déposer l'électrolyte de YSZ et l'électrolyte de silicate de lanthane par les LPSPS processus développés, afin d'examiner l'application de cette technologie dans la pile à combustible à oxydes solides (SOFC). Les premiers résultats ont montré que la densité de l'électrolyte silicate de lanthane était plus haute à celle de l'électrolyte de YSZ, et la perméabilité aux gaz du premier était également plus faible à celle du second. Les deux électrolytes présentaient une perméabilité faible de l'ordre de grandeur de $10^{-17} m^2$ même dans une épaisseur assez faible (30~50 μm). De plus, les deux électrolytes présentaient une cristallinité élevée et aucune phase amorphe ne s'était formée dans l'électrolyte silicate de lanthane. Ces résultats indiquent que le LPSPS a un énorme potentiel dans la préparation de l'électrolyte de SOFC

Mots clés: revêtement céramique nanostructuré, projection plasma de suspension sous basse pression, caractéristiques structurelles, conditions de projection, pile à combustible à oxyde solide

Publications

[1] **S. Xie**, C. Song, Z. Yu, S. Liu, F. Lapostolle, D. Klein, C. Deng, M. Liu, H. Liao, Effect of environmental pressure on the microstructure of YSZ thermal barrier coating via suspension plasma spraying, **Journal of the European Ceramic Society**, 41 (2021) 535-543

[2] **S. Xie**, M. Dai, S. Lin, Q. Shi, C. Song, H. Hou, W. Qiu, Y. Wang, Effect of bias voltage on the oxidation resistance of NiCoCrAlYTa coatings prepared by arc ion plating, **Corrosion Science**, 147 (2019) 330-341.

[3] **S. Xie,** C. Song, S. Liu, F. Lapostolle, D. Klein, C. Deng, M. Liu, H. Liao, Dense nanostructured YSZ coating prepared by low-pressure suspension plasma spraying: Atmosphere control and deposition mechanism, **Surface & Coatings Technology** 416 (2021) 127175

[4] **S. Xie**, S. Lin, Q. Shi, W. Wang, C. Song, W, Xu. M.Dai, A study on the mechanical and thermal shock properties of MCrAlY coating prepared by arc ion plating, **Surface and Coatings Technology**, 413(2021) 127092

[5] **S. Xie**, C. Song, Z. Yu, S. Liu, F. Lapostolle, D. Klein, C. Deng, M. Liu, H. Liao, Dense and thin nanostructured electrolyte coatings prepared by low-pressure suspension plasma spraying. **Journal of Power Source**, *in preparation*.

[6] C. Song, **S. Xie***, X.-J. Fan, P.-J. He, M. Liu, K.-S. Zhou, C.-M. Deng, H.-L. Liao, Very low-pressure plasma-sprayed dense yttria-stabilized zirconia coatings using an axial bi-cathode plasma torch, **Surface and Coatings Technology**, 402 (2020) 126281.

[7] S. Liu, **S. Xie***; H. Wu; Z. Yu; W. Wang; M. MOLIERE; H. LIAO, Novel Liquid Fuel HVOF Torches Fueled with Ethanol: Optimization and Erosion Wear Response of Cr3C2-NiCr Coatings, **Journal of the European Ceramic Society**, *under review*

[8] S. Liu, H. Wu, **S. Xie**, M.-P. Planche, D. Rivolet, M. Moliere, H. Liao, Novel liquid fuel HVOF torches fueled with ethanol: relationships between in-flight particle characteristics and properties of WC-10Co-4Cr coatings, **Surface and Coatings Technology**,

408 (2021) 126805.

[9] C. Song, Y. Wang, X.-j. Fan, **S. Xie**, M. Liu, K.-s. Zhou, C.-m. Deng, C.-g. Deng, H.-l. Liao, Microstructure and mechanical property of dense yttria-stabilized zirconia coating fabricated by an axial bi-cathode plasma torch under very low pressure, **Ceramics International**, 46 (2020) 9507-9511.

[10] Z. Chen, X. Yan, Y. Chang, **S. Xie**, W. Ma, G. Zhao, H. Liao, H. Fang, M. Liu, D. Cai, Effect of polarization voltage on the surface componentization and biocompatibility of micro-arc oxidation modified selective laser melted Ti6Al4V, **Materials Research Express**, 6 (2019) 086425.

[11] H. Wu, S. Liu, X. Xie, Y. Xie, **S. Xie,** R. Huang, C. Verdy, M. Liu, H. Liao, Mechanical Reliability of Multi-Deposits Produced by Hybrid Cold Spray Additive Manufacturing, **Journal of Materials Processing Tech,** *under review*